

CMS Draft Analysis Note

The content of this note is intended for CMS internal use and distribution only

2017/04/30

Head Id: 401684

Archive Id: 401646:401684

Archive Date: 2017/04/30

Archive Tag: trunk

Search for the standard model Higgs boson decaying to a pair of tau leptons in 2016 data

Isobel Ojalvo¹⁰, Kelvin Mei¹⁰, Artur Akhmetshin¹¹, Raphael Friese¹¹, Andrew Gilbert¹¹, Stefan Wayand¹¹, Roger Wolf¹¹, Valeria Botta¹², Francesco Costanza¹², Elisabetta Gallo¹², Teresa Lenz¹², Alexei Raspereza¹², Yiwen Wen¹², Alexis Kalogeropoulos¹², Alberto Bragagnolo¹², Thomas Müller¹³, Alexander Nehrkorn¹³, Johannes Brandstetter¹⁴, Martin Flechl¹⁴, Markus Spanring¹⁴, Cecile Caillol¹, Laura Dodd¹, Sridhara Dasu¹, Tyler Ruggles¹, Alexander Savin¹, Wesley Smith¹, David Colling², Daniel Winterbottom², Rebecca Lane², Olivier Davignon³, Ketino Kaadze⁴, Yurii Maravin⁴, Abdollah Mohammadi⁴, Riccardo Manzoni⁵, Lucia Perrini⁶, Christian Veelken⁶, Jan Steggemann⁷, Yuta Takahashi⁸, and Olena Hlushchenko⁹

¹ University of Wisconsin Madison

² Imperial College London

³ Centre National de la Recherche Scientifique

⁴ Kansas State University

⁵ Universita & INFN, Milano-Bicocca

⁶ National Institute of Chemical Physics and Biophysics

⁷ CERN

⁸ Universitaet Zuerich

⁹ National Taras Shevchenko Univ.

¹⁰ Princeton University

¹¹ Karlsruhe Institute of Technology

¹² Deutsches Elektronen-Synchrotron

¹³ Rheinisch-Westfaelische Tech. Hoch.

¹⁴ Austrian Academy of Sciences

Abstract

A search for the standard model Higgs boson which decays to a pair of τ leptons is presented using 35.9 fb^{-1} of 13 TeV data collected in 2016 by the CMS detector at CERN. Final states considered require that one τ lepton decays leptonically while the other decays hadronically, $\mu\tau_h$ or $e\tau_h$, both taus decay hadronically, $\tau_h\tau_h$, or one τ decays to an electron while the other decays to a muon, $e\mu$. An excess with a significance of 4.9 standard deviations is observed for $m_H = 125 \text{ GeV}$. The signal strength, μ , relative to the expectation for the standard model Higgs boson is measured to be 1.06 ± 0.25 .

This box is only visible in draft mode. Please make sure the values below make sense.

PDFAuthor: Valeria Botta, Johannes Brandstetter, Cecile Caillol, Laura Dodd, Martin Flechl, Ketino Kaadze, Abdollah Mohammadi, Isabel Ojalvo, Alexei Raspiereza, Tyler Ruggles, Alexander Savin, Markus Spanring, Yuta Takahashi, Yiwen Wen

PDFTitle: Search for the standard model Higgs boson decaying to a pair of tau leptons in 2016 data

PDFSubject: CMS

PDFKeywords: CMS, physics, software, computing

Please also verify that the abstract does not use any user defined symbols

1 Contents

2	1	Introduction	2
3	2	Samples	3
4	3	Object reconstruction	7
5	3.1	Hadronically decaying taus	7
6	3.2	Muons	7
7	3.3	Electrons	8
8	3.4	Lepton isolation	8
9	3.5	Jets	8
10	3.6	Missing transverse energy	9
11	4	Event weights and data/simulation corrections	9
12	4.1	PU reweighting	9
13	4.2	Tau identification efficiency scale factors	9
14	4.3	Anti-lepton discriminator tau-ID scale factors	10
15	4.4	Lepton ID/isolation scale factors	11
16	4.5	Trigger efficiencies	12
17	4.6	Reweighting of LO Madgraph Drell-Yan samples	13
18	4.7	Top p_T reweighting	14
19	4.8	Recoil corrections	14
20	4.9	Generator event weights and luminosity	16
21	5	Signal extraction	18
22	6	The $\mu\tau_h$ final state	22
23	6.1	Trigger requirements	22
24	6.2	Event selection	22
25	6.3	Background estimation	25
26	6.4	Signal extraction	29
27	6.5	Control plots	31
28	7	The $e\tau_h$ final state	36
29	7.1	Trigger requirements	36
30	7.2	Event selection	36
31	7.3	Background methods	37
32	7.4	Signal extraction	39
33	7.5	Control plots	42
34	8	The $\tau_h\tau_h$ final state	42
35	8.1	Trigger requirements	42
36	8.2	Event selection	44
37	8.3	Signal extraction	46
38	8.4	Background methods	47
39	8.5	Control plots	52
40	9	The $e\mu$ final state	57
41	9.1	Trigger requirements	57
42	9.2	Offline selection	57
43	9.3	MC corrections	60

44	9.4	Event categories and signal extraction	60
45	9.5	Background estimation	60
46	9.6	Control Plots	63
47	9.7	Mass plots	63
48	10	Fit model	63
49	11	Systematic uncertainties	70
50	11.1	Lepton isolation and identification	70
51	11.2	Luminosity	71
52	11.3	W+jets estimation	71
53	11.4	QCD estimation	72
54	11.5	$t\bar{t}$ estimation	73
55	11.6	Other MC normalization	75
56	11.7	Fake rates	75
57	11.8	Energy scales	75
58	11.9	Z+jets reweighting	78
59	11.10	Btagging uncertainty	79
60	11.11	Z+jets estimation uncertainty	79
61	11.12	$t\bar{t}$ reweighting according to generated top/antitop p_T	79
62	11.13	Theoretical uncertainties for signal	79
63	11.14	Systematic uncertainties summary	80
64	12	Results	82
65	13	Summary	84

1 Introduction

67 Understanding the mechanism of electroweak symmetry breaking through which the W and
 68 Z bosons become massive is a central goal of the Large Hadron Collider (LHC) physics pro-
 69 gram. In the standard model (SM) [1, 2], the Brout-Englert-Higgs mechanism [3–8] allows for
 70 electroweak symmetry breaking and calls for the existence of a new massive particle, the Higgs
 71 boson. During Run I at the LHC the discovery of the Higgs boson was announced by the AT-
 72 LAS and CMS collaborations [9–11] with the most significant excesses seen in ZZ, $\gamma\gamma$, and WW
 73 decay channels.

74 In the SM, it is postulated that the Higgs boson gives mass to fermions via the Yukawa cou-
 75 plings. Therefore, detection of the Higgs boson decay to fermions and measurement of its
 76 properties through the fermionic decays is an essential ingredient to identifying this newly dis-
 77 covered particle as the SM Higgs boson. Many searches for the SM Higgs boson decay to a τ
 78 lepton pair have been performed [12–15]. Using the full Run I dataset, evidence for the 125
 79 GeV Higgs boson coupling to τ leptons was found by both the ATLAS and CMS collaborations
 80 with a measured signal strength of 1.43 ± 0.43 and 0.78 ± 0.27 , respectively [16, 17].

81 This Analysis Note summarizes the search for the SM Higgs boson via its decay to τ leptons in
 82 proton-proton collisions at $\sqrt{s} = 13$ TeV at the LHC. A dataset collected in 2016 at the LHC and
 83 corresponding to a total integrated luminosity of 35.9 fb^{-1} was used. The note is organized into
 84 the following subsections: data samples and Monte Carlo simulations, object reconstruction,
 85 event weights for data/simulation corrections, signal extraction, four sections detailing the
 86 individual channels ($e\tau_h$, $\mu\tau_h$, $\tau_h\tau_h$, $e\mu$), systematic uncertainties, and finally the results.

⁸⁷ A separate analysis note detailing the treatment of theory systematic uncertainties in this anal-
⁸⁸ ysis can be found at *AN-16-387*.

⁸⁹ 2 Samples

⁹⁰ This analysis is based on proton-proton collision data at a center of mass energy of 13 TeV
⁹¹ collected in 2016 with the CMS detector at the CERN LHC. The data analyzed corresponds
⁹² to an integrated luminosity of 35.9 fb^{-1} . The collision datasets, run ranges, and integrated
⁹³ luminosity per dataset are given in Tab. 1. Only data that is collected and fully certified by the
⁹⁴ CMS collaboration is used for this analysis; the data which is fully certified is selected using
⁹⁵ the JSON file `Cert_271036-276811_13TeV_PromptReco_Collisions16_JSON.txt`.

⁹⁶ The Monte Carlo (MC) simulations that model significant SM backgrounds in the analysis are
⁹⁷ listed in Tab. 2. The $W + \text{jets}$, and $Z/\gamma^* \rightarrow \ell\ell$ samples are generated with MADGRAPH [18],
⁹⁸ while the single top and $t\bar{t}$ samples are generated with POWHEG [19]. The diboson samples
⁹⁹ are generated either with MADGRAPH or POWHEG. The PYTHIA8 [20] generator, with the tune
¹⁰⁰ CUETP8M1 [21], is used to model the parton shower and hadronization processes, as well
¹⁰¹ as tau decays in all samples. The cross sections for single top and di-boson production are
¹⁰² computed at NLO accuracy [22]. A k-factor of 1.16 is considered for the $Z + \text{jets}$ samples, and
¹⁰³ 1.21 for the $W + \text{jets}$ samples. The NNPDF3.0 parton distribution functions are used [23].

¹⁰⁴ MC samples used for signal modeling can be found in Tab. 3. The signal samples are pro-
¹⁰⁵ duced using POWHEG. The gluon-gluon fusion, vector boson fusion, and associated produc-
¹⁰⁶ tion modes are considered.

¹⁰⁷ All simulated samples are reweighted to match the pile-up distribution in data, corresponding
¹⁰⁸ to a minimum bias cross section of 69.2 mb.

Channel	Dataset	Run range	Integrated Luminosity
$e\mu$	/MuonEG/Run2016B-03Feb2017-ver2-v2/MINIAOD	272007–275376	5.788 /fb
$e\mu$	/MuonEG/Run2016C-03Feb2017-v1/MINIAOD	275657–276283	2.573 /fb
$e\mu$	/MuonEG/Run2016D-03Feb2017-v1/MINIAOD	276315–276811	4.248 /fb
$e\mu$	/MuonEG/Run2016E-03Feb2017-v1/MINIAOD	276831–277420	4.009 /fb
$e\mu$	/MuonEG/Run2016F-03Feb2017-v1/MINIAOD	277772–278808	3.102 /fb
$e\mu$	/MuonEG/Run2016G-03Feb2017-v1/MINIAOD	278820–280385	7.540 /fb
$e\mu$	/MuonEG/Run2016H-03Feb2017-ver2-v1/MINIAOD	280919–284044	8.606 /fb
$e\mu$	/MuonEG/Run2016H-03Feb2017-ver3-v1/MINIAOD	280919–284044	see above
$\mu\tau_h$	/SingleMuon/Run2016B-03Feb2017-ver2-v2/MINIAOD	272007–275376	5.788 /fb
$\mu\tau_h$	/SingleMuon/Run2016C-03Feb2017-v1/MINIAOD	275657–276283	2.573 /fb
$\mu\tau_h$	/SingleMuon/Run2016D-03Feb2017-v1/MINIAOD	276315–276811	4.248 /fb
$\mu\tau_h$	/SingleMuon/Run2016E-03Feb2017-v1/MINIAOD	276831–277420	4.009 /fb
$\mu\tau_h$	/SingleMuon/Run2016F-03Feb2017-v1/MINIAOD	277772–278808	3.102 /fb
$\mu\tau_h$	/SingleMuon/Run2016G-03Feb2017-v1/MINIAOD	278820–280385	7.540 /fb
$\mu\tau_h$	/SingleMuon/Run2016H-03Feb2017-ver2-v1/MINIAOD	280919–284044	8.606 /fb
$\mu\tau_h$	/SingleMuon/Run2016H-03Feb2017-ver3-v1/MINIAOD	280919–284044	see above
$e\tau_h$	/SingleElectron/Run2016B-03Feb2017-ver2-v2/MINIAOD	272007–275376	5.788 /fb
$e\tau_h$	/SingleElectron/Run2016C-03Feb2017-v1/MINIAOD	275657–276283	2.573 /fb
$e\tau_h$	/SingleElectron/Run2016D-03Feb2017-v1/MINIAOD	276315–276811	4.248 /fb
$e\tau_h$	/SingleElectron/Run2016E-03Feb2017-v1/MINIAOD	276831–277420	4.009 /fb
$e\tau_h$	/SingleElectron/Run2016F-03Feb2017-v1/MINIAOD	277772–278808	3.102 /fb
$e\tau_h$	/SingleElectron/Run2016G-03Feb2017-v1/MINIAOD	278820–280385	7.540 /fb
$e\tau_h$	/SingleElectron/Run2016H-03Feb2017-ver2-v1/MINIAOD	280919–284044	8.606 /fb
$e\tau_h$	/SingleElectron/Run2016H-03Feb2017-ver3-v1/MINIAOD	280919–284044	see above
$\tau_h\tau_h$	/Tau/Run2016B-03Feb2017-ver2-v2/MINIAOD	272007–275376	5.788 /fb
$\tau_h\tau_h$	/Tau/Run2016C-03Feb2017-v1/MINIAOD	275657–276283	2.573 /fb
$\tau_h\tau_h$	/Tau/Run2016D-03Feb2017-v1/MINIAOD	276315–276811	4.248 /fb
$\tau_h\tau_h$	/Tau/Run2016E-03Feb2017-v1/MINIAOD	276831–277420	4.009 /fb
$\tau_h\tau_h$	/Tau/Run2016F-03Feb2017-v1/MINIAOD	277772–278808	3.102 /fb
$\tau_h\tau_h$	/Tau/Run2016G-03Feb2017-v1/MINIAOD	278820–280385	7.540 /fb
$\tau_h\tau_h$	/Tau/Run2016H-03Feb2017-ver2-v1/MINIAOD	280919–284044	8.606 /fb
$\tau_h\tau_h$	/Tau/Run2016H-03Feb2017-ver3-v1/MINIAOD	280919–284044	see above

Table 1: List of datasets included in the analysis. Re-miniAOD is used for data.

Background MC simulations	Cross section
/DYJetsToLL_M-50_TuneCUETP8M1_13TeV-madgraphMLM-pythia8	4954.0 pb (LO)
/DY1JetsToLL_M-50_TuneCUETP8M1_13TeV-madgraphMLM-pythia8	1012.5 pb (LO)
/DY2JetsToLL_M-50_TuneCUETP8M1_13TeV-madgraphMLM-pythia8	332.8 pb (LO)
/DY3JetsToLL_M-50_TuneCUETP8M1_13TeV-madgraphMLM-pythia8	101.8 pb (LO)
/DY4JetsToLL_M-50_TuneCUETP8M1_13TeV-madgraphMLM-pythia8	54.8 pb (LO)
/DYJetsToLL_M-150_TuneCUETP8M1_13TeV-madgraphMLM-pythia8	6.657 pb (LO)
/DYJetsToLL_M-10to50_TuneCUETP8M1_13TeV-madgraphMLM-pythia8	18610 pb (LO)
/TT_TuneCUETP8M1_13TeV-powheg-pythia8	831.76 pb
/WJetsToLNu_TuneCUETP8M1_13TeV-madgraphMLM-pythia8	50380 pb (LO)
/W1JetsToLNu_TuneCUETP8M1_13TeV-madgraphMLM-pythia8	9644.5 pb (LO)
/W2JetsToLNu_TuneCUETP8M1_13TeV-madgraphMLM-pythia8	3144.5 pb (LO)
/W3JetsToLNu_TuneCUETP8M1_13TeV-madgraphMLM-pythia8	954.8 pb (LO)
/W4JetsToLNu_TuneCUETP8M1_13TeV-madgraphMLM-pythia8/	485.6 pb (LO)
/WZTo1L3Nu_13TeV_amcatnloFXFX_madspin_pythia8	3.05 pb
/WZTo1L1Nu2Q_13TeV_amcatnloFXFX_madspin_pythia8	10.71 pb
/WZTo2L2Q_13TeV_amcatnloFXFX_madspin_pythia8	5.595 pb
/ST_tW_antitop_5f_inclusiveDecays_13TeV-powheg-pythia8_TuneCUETP8M1	35.6 pb
/ST_tW_top_5f_inclusiveDecays_13TeV-powheg-pythia8_TuneCUETP8M1	35.6 pb
/ST_t-channel_antitop_4f_leptonDecays_13TeV-powheg-pythia8_TuneCUETP8M1	80.95 pb
/ST_t-channel_top_4f_leptonDecays_13TeV-powheg-pythia8_TuneCUETP8M1	136.02 pb
/WWTo1L1Nu2Q_13TeV_amcatnloFXFX_madspin_pythia8	1.212 pb
/ZZTo2L2Q_13TeV_amcatnloFXFX_madspin_pythia8	3.22 pb
/VVTo2L2Nu_13TeV_amcatnloFXFX_madspin_pythia8	11.95 pb
/WZJToLLLNU_TuneCUETP8M1_13TeV-amcnlo_pythia8	4.708 pb
/WZTo1L1Nu2Q_13TeV_amcatnloFXFX_madspin_pythia8	10.71 pb
/WZTo1L3Nu_13TeV_amcatnloFXFX_madspin_pythia8	3.05 pb
/WZTo2L2Q_13TeV_amcatnloFXFX_madspin_pythia8	5.595 pb
/ZZTo4L_13TeV-amcatnloFXFX_pythia8	1.212 pb
/EWKWMminus2Jets_WToLNu_M-50_13TeV-madgraph-pythia8	20.25 pb
/EWKWPplus2Jets_WToLNu_M-50_13TeV-madgraph-pythia8	25.62 pb
/EWKZ2Jets_ZToLL_M-50_13TeV-madgraph-pythia8	3.987 pb
/EWKZ2Jets_ZToNuNu_13TeV-madgraph-pythia8	10.01 pb
/GluGluHToWWTo2L2Nu_M125_13TeV_powheg_JHUGen_pythia8	1.001 pb
/VBFHToWWTo2L2Nu_M125_13TeV_powheg_JHUGen_pythia8	0.0858 pb
/WGToLNuG_TuneCUETP8M1_13TeV-amcatnloFXFX_pythia8	489.0 pb
/WGstarToLNuMuMu_012Jets_13TeV-madgraph	2.793 pb
/WGstarToLNuEE_012Jets_13TeV-madgraph	3.526 pb

Table 2: MC background samples included in the analysis. All samples are generated for p-p collisions at a center-of-mass energy of 13 TeV. Samples used in this analysis are reconstructed and stored in miniAOD format. A k-factor of 1.16 is considered for the Z+jets samples, and 1.21 for the W+jets samples. These MC samples all belong to the Summer16 production, with Moriond Premix conditions. When available, all sample extensions are used.

Signal MC sample	Production cross section	$H \rightarrow \tau\tau$ branching fraction
/GluGluHToTauTau_M110_13TeV_powheg_pythia8	57.90 pb	0.0791
/GluGluHToTauTau_M120_13TeV_powheg_pythia8	52.22 pb	0.0698
/GluGluHToTauTau_M125_13TeV_powheg_pythia8	48.58 pb	0.0627
/GluGluHToTauTau_M130_13TeV_powheg_pythia8	45.31 pb	0.0541
/GluGluHToTauTau_M140_13TeV_powheg_pythia8	36.00 pb	0.0360
/VBFHToTauTau_M110_13TeV_powheg_pythia8	4.434 pb	0.0791
/VBFHToTauTau_M120_13TeV_powheg_pythia8	3.935 pb	0.0698
/VBFHToTauTau_M125_13TeV_powheg_pythia8	3.782 pb	0.0627
/VBFHToTauTau_M130_13TeV_powheg_pythia8	3.637 pb	0.0541
/VBFHToTauTau_M140_13TeV_powheg_pythia8	3.492 pb	0.0360
/ZHToTauTau_M110_13TeV_powheg_pythia8	1.309 pb	0.0791
/ZHToTauTau_M120_13TeV_powheg_pythia8	0.994 pb	0.0698
/ZHToTauTau_M125_13TeV_powheg_pythia8	0.884 pb	0.0627
/ZHToTauTau_M130_13TeV_powheg_pythia8	0.790 pb	0.0541
/ZHToTauTau_M140_13TeV_powheg_pythia8	0.6514 pb	0.0360
/WplusHToTauTau_M110_13TeV_powheg_pythia8	1.335 pb	0.0791
/WplusHToTauTau_M120_13TeV_powheg_pythia8	0.9558 pb	0.0698
/WplusHToTauTau_M125_13TeV_powheg_pythia8	0.8400 pb	0.0627
/WplusHToTauTau_M130_13TeV_powheg_pythia8	0.7414 pb	0.0541
/WplusHToTauTau_M140_13TeV_powheg_pythia8	0.6308 pb	0.0360
/WminusHToTauTau_M110_13TeV_powheg_pythia8	0.8587 pb	0.0791
/WminusHToTauTau_M120_13TeV_powheg_pythia8	0.6092 pb	0.0698
/WminusHToTauTau_M125_13TeV_powheg_pythia8	0.5328 pb	0.0627
/WminusHToTauTau_M130_13TeV_powheg_pythia8	0.4676 pb	0.0541
/WminusHToTauTau_M140_13TeV_powheg_pythia8	0.3940 pb	0.0360

Table 3: List of Monte Carlo signal samples included in the analysis.

109 **3 Object reconstruction**

110 At CMS, particle reconstruction is performed using a particle-flow (PF) algorithm [24–27] that
 111 combines information from CMS subdetectors to reconstruct and identify particles from each
 112 proton-proton collision. The particles are classified as either charged hadrons, neutral hadrons,
 113 photons, muons, and electrons. The particle list from each event is then used to reconstruct the
 114 missing transverse energy, jets, the τ_h candidates and to quantify lepton isolation.

115 **3.1 Hadronically decaying taus**

116 Hadronic decays of τ leptons are reconstructed and identified with the Hadron Plus Strips
 117 (HPS) algorithm [28, 29]. The basic features of the algorithm are identical to those of Run-
 118 I. The HPS algorithm is seeded by the reconstructed jets. The algorithm makes use of the
 119 constituents of the jets to reconstruct the neutral pions that are present in most τ_h decays. The
 120 high probability for photons originating from $\pi^0 \rightarrow \gamma\gamma$ decays to convert to e^+e^- pairs is
 121 accounted for by collecting the photon and electron ($p_T > 0.5$ GeV) constituents of the jet into
 122 clusters (*strips*). In Run I, the size of the strips was set to a fixed value of 0.05×0.20 in the $\eta - \phi$
 123 direction. For Run II, the size of the strip is allowed to vary dynamically in order to account
 124 for nuclear interactions between the tracker material and low p_T secondary particles, and to
 125 account for the more narrow, boosted topologies of high p_T neutral hadrons.

126 The τ_h candidates are formed by combining the strips with the charged-particle constituents of
 127 the jet. Based on the observed number of strips and charged particles, it is assigned to be one
 128 of the following *decay modes*:

- 129 • a single charged particle without any strips: `oneProngZeroPizero`;
- 130 • combination of one charged particle and one strip: `oneProngOnePizero`;
- 131 • combination of a single charged particle with two strips: `oneProngTwoPizero`;
- 132 • combination of three charged particles: `threeProngZeroPizero`.

133 The isolation of τ_h candidates is based on an MVA discriminator that takes into account usual
 134 isolation variables based on energy deposits in a cone of $\Delta R < 0.5$ around the τ_h candidates, as
 135 well as variables related to the tau lifetime.

136 Electrons and muons are rejected with an MVA-based, and a cut-based discriminators, respec-
 137 tively. The working point of the discriminators against electrons and muons depends on the
 138 final state.

139 The τ_h energy scale is corrected depending on the decay mode. The corrections are the follow-
 140 ing:

- 141 • -1.8% for 1 prong taus;
- 142 • +1.0% for 1 prong $+\pi^0$ s taus;
- 143 • +0.4% for 3 prong taus.

144 The uncertainty on the correction amounts to 0.6%.

145 **3.2 Muons**

146 Muons are reconstructed from both the inner tracker and the muon subsystems [30]. The PF
 147 muons are selected from among the reconstructed muon track candidates by applying minimal
 148 requirements on the track components in the muon system and taking into account matching
 149 with small energy deposits in the calorimeters.

150 The medium ID is applied to muons in MC simulations. For data events in runs B to F, the
 151 "medium 2016" ID is used to recover from some tracking inefficiency in that period, and the
 152 medium ID is used in runs G and H. The medium and medium 2016 ID have about the same
 153 efficiency in MC simulations. In runs G and H the medium ID selects approximately 10% less
 154 fake muons in data at low p_T , in comparison with the medium 2016 ID. In practice the data/MC
 155 scale factors are measured as a weighted combination of the two IDs.

156 3.3 Electrons

157 Electrons are reconstructed from clusters of energy deposits in the ECAL and GSF tracks in the
 158 inner tracker [31]. Electron identification relies on the electromagnetic shower shape and other
 159 observables based on tracker and calorimeter information. The selection criteria depend on p_T
 160 and $|\eta|$, and on a categorization according to observables that are sensitive to the amount of
 161 bremsstrahlung emitted along the trajectory in the tracker.

162 The electrons are identified based on an MVA discriminator. The "general purpose" ID, re-
 163 trained on Spring16 MC samples, is used in the analysis.

164 3.4 Lepton isolation

165 The isolation of muons (electrons) is measured relative to their transverse momentum p_T^ℓ , by
 166 summing over the transverse momenta of PF particles in a cone with $\Delta R < 0.4$ (0.3) around the
 167 lepton:

$$R_{\text{Iso}}^\ell = \left(\sum p_T^{\text{charged}} + \max \left[0, \sum p_T^{\text{neutral}} + \sum p_T^\gamma - p_T^{\text{PU}}(\ell) \right] \right) / p_T^\ell. \quad (1)$$

168 The $\sum p_T^{\text{charged}}$ is the scalar sum of the transverse momenta of charged hadrons originating from
 169 the primary vertex. The $\sum p_T^{\text{neutral}}$ and $\sum p_T^\gamma$ are the scalar sums of the transverse momenta for
 170 neutral hadrons and photons, respectively. The neutral contribution to isolation from pileup,
 171 $p_T^{\text{PU}}(\ell)$, is estimated using a jet area method [32] for the electron. For the muon, the $p_T^{\text{PU}}(\ell)$ con-
 172 tribution is estimated using the sum of transverse momenta of charged hadrons not originating
 173 from the primary vertex scaled by a factor of 0.5.

174 3.5 Jets

175 Jets are reconstructed by clustering all PF candidates using the anti- k_T algorithm with distance
 176 parameter $\Delta R = 0.4$ [33]. Charged hadrons that are not originating from the primary ver-
 177 tex are subtracted from the PF candidates (hadron subtraction). Jet-energy corrections are not
 178 reapplied on MiniAOD MC samples with the production global tag:

- 179 • 80X_mcRun2_asymptotic_2016_TrancheIV_v8

180 Jet energy corrections are reapplied for data samples with the global tag:

- 181 • 80X_dataRun2_2016SeptRepro_v7

182 Applied correction labels in data events are L1FastJet, L2Relative, L3Absolute and L2L3Residual
 183 correction levels. Jets are only considered if they pass the loose working point of the PF jet ID
 184 discriminator provided by the JETMET POG [34] and if they have a corrected transverse mo-
 185 mentum above 30 GeV and $|\eta| < 4.7$. Additionally, they have to be separated from every τ
 186 candidate (τ_h , electrons, or muons) that passes object selection by $\Delta R > 0.5$.

187 **3.6 Missing transverse energy**

188 All particles reconstructed in the event are used to determine the missing transverse energy.
 189 The missing transverse energy is defined as the negative vectorial sum of the transverse mo-
 190 ments of all PF candidates. Type-1 corrections are applied to the transverse missing energy, as
 191 well as recoil corrections, which are described in the next section.

192 **4 Event weights and data/simulation corrections**

193 Various weights are applied on an event-by-event basis to simulations to improve the data-
 194 MC agreement. The derivation and application of these weights is described in the following
 195 paragraphs.

196 **4.1 PU reweighting**

197 Pile Up (PU) reweighting is applied to the MC simulations in order to have similar PU distri-
 198 butions in data and in simulations. A minimum bias cross section of 69.2 mb is used. The "True
 199 PU" reweighting method is used. The range of the number of primary vertices used is 0-80,
 200 with 800 bins. The MC distribution of the number of primary vertices is reweighted to match
 201 the number of pile-up interactions in data given the recommended minimum bias cross section
 202 of 69.2 mb. The data/MC distributions before and after reweighting are shown in Fig. 1.

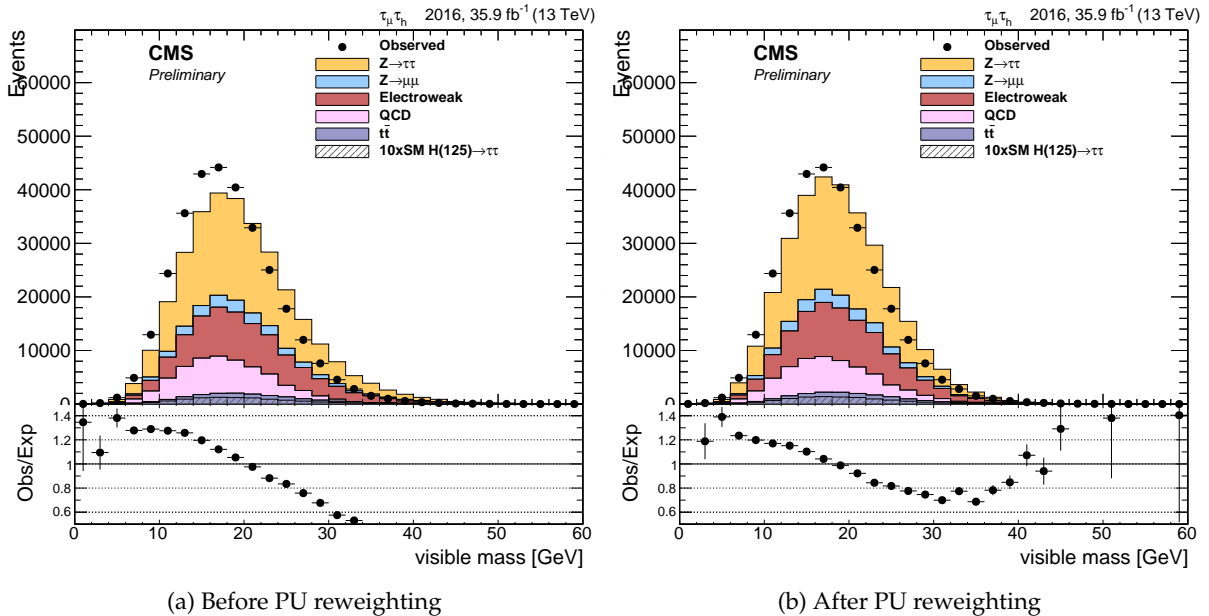


Figure 1: Primary vertex distribution before and after the pile-up reweighting described in the text, in the $\mu\tau_h$ final state.

203 **4.2 Tau identification efficiency scale factors**

204 In order to correct for differences seen between data and simulations in hadronic tau identifi-
 205 cation, scale factors have been calculated by the Tau POG for various working points. The
 206 measurements are based on a tag-and-probe method in $Z \rightarrow \tau_\mu \tau_h$ events. Events with a muon
 207 and an OS loosely defined tau candidate (passing decay mode finding, and with at least one
 208 track with p_T greater than 5 GeV) are divided into two categories whether the loosely defined

tau candidate passes or does not pass the working point of the discriminator under study. The $Z \rightarrow \tau_\mu \tau_h$ contribution to each region is adjusted with a maximum likelihood fit that considers the tau identification efficiency scale factor as the parameter of interest. A $Z \rightarrow \mu\mu$ control region is added to the fit to control the Drell-Yan cross section times luminosity. The parameter of interest is anti-correlated between the Pass and the Fail regions, with a factor that depends on the expected number of $Z \rightarrow \tau_\mu \tau_h$ events in each category. The fit is performed using the visible mass of the muon and the tau, or the number of tracks within the signal and isolation cones of the tau candidate, as the observable. Figure 2 shows the postfit Pass and Fail regions used for the tag and probe measurement of the tau identification efficiency scale factor for the MVA tight isolation working point.

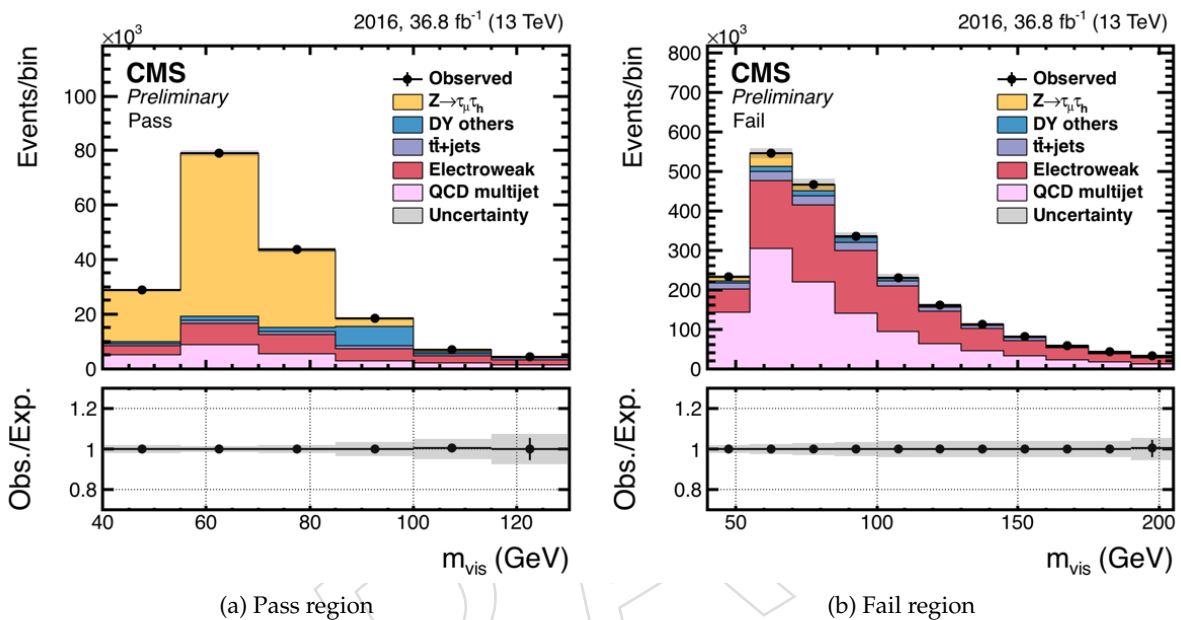


Figure 2: Tag-and-probe measurement of the tau identification efficiency scale factor in $Z \rightarrow \tau_\mu \tau_h$ events, for the MVA tight isolation working point, using the visible mass between the muon and the tau candidate as an observable. The distributions shown are the visible mass of the μ and τ_h postfit in the Pass region, (2a), and the Fail region, (2b). All τ_h decay modes are included; p_T is required to be greater than 20 GeV and $|\eta| < 2.3$.

The MVA discriminators are stored in miniAOD and are accessed by, for example, `tauID (byTightIsolationMVArun2v1DBoldDMwLT)` has a scale factor of 0.95 ± 0.05 applied to real tau backgrounds. If there are two hadronic taus in the final state, for example in $Z \rightarrow \tau_h \tau_h$ events, the weights for each leg are multiplied together. There is no evidence for a variation of the tau identification efficiency scale factor with the p_T of the tau candidate, with its pseudorapidity or with its decay mode.

4.3 Anti-lepton discriminator tau-ID scale factors

The anti-lepton discriminator scale factors, measured by Tau POG, are applied to the backgrounds where a reconstructed tau is matched at generator-level to a prompt lepton. The scale factor of the tighter discriminator is chosen. In $\mu\tau$, the scale factor for `tauID (againstMuonTight3)` is applied to background simulation where a μ fakes a τ . The scale factors are found with a tag and probe method in $Z+jets$ events. In the Fail region

Table 4: Efficiency scale factors for the discriminators used to reject prompt leptons in the tau identification process.

Tau discriminator	η range	Scale factor
againstElectronMVAVLoose	$ \eta < 1.460$	1.213 ± 0.07
againstElectronMVALoose	$ \eta < 1.460$	1.320 ± 0.04
againstElectronMVAMedium	$ \eta < 1.460$	1.323 ± 0.07
againstElectronMVATight	$ \eta < 1.460$	1.402 ± 0.11
againstElectronMVAVTight	$ \eta < 1.460$	1.207 ± 0.18
againstElectronMVAVLoose	$ \eta > 1.558$	1.375 ± 0.05
againstElectronMVALoose	$ \eta > 1.558$	1.380 ± 0.04
againstElectronMVAMedium	$ \eta > 1.558$	1.527 ± 0.13
againstElectronMVATight	$ \eta > 1.558$	1.900 ± 0.30
againstElectronMVAVTight	$ \eta > 1.558$	1.968 ± 0.46
againstMuonLoose3	$ \eta < 0.4$	1.010 ± 0.02
againstMuonTight3	$ \eta < 0.4$	1.263 ± 0.07
againstMuonLoose3	$0.4 < \eta < 0.8$	1.007 ± 0.03
againstMuonTight3	$0.4 < \eta < 0.8$	1.364 ± 0.28
againstMuonLoose3	$0.8 < \eta < 1.2$	0.870 ± 0.03
againstMuonTight3	$0.8 < \eta < 1.2$	0.854 ± 0.04
againstMuonLoose3	$1.2 < \eta < 1.7$	1.154 ± 0.13
againstMuonTight3	$1.2 < \eta < 1.7$	1.712 ± 0.5
againstMuonLoose3	$1.7 < \eta < 2.3$	2.281 ± 0.26
againstMuonTight3	$1.7 < \eta < 2.3$	2.324 ± 0.5

(tau candidates fail the anti-lepton discriminator under study), the major contribution comes from $Z \rightarrow ll$ events, which form a narrow peak around the Z boson mass. The scale factors have been measured in Remini-AOD data.

The scale factors used in the analysis depend on the pseudorapidity of the tau candidate, and are indicated in Tab. 4. The uncertainties typically range between 5% and 30%, and are related to the more statistically limited populations of the Pass region.

4.4 Lepton ID/isolation scale factors

Lepton identification and isolation efficiencies are measured in data and MC using a tag-and-probe technique, and the efficiency ratio $\epsilon_{data}/\epsilon_{MC}$ is applied as a weight on an event-by-event basis to correct the simulation. Efficiencies are measured in $Z \rightarrow ee$ and $Z \rightarrow \mu\mu$ events, in bins of lepton p_T and $|\eta|$.

The selection of the tag-and-probe pairs is defined as follows. The tag lepton must satisfy the kinematic, ID, and isolation requirements used in the analysis, in data it should also be matched to a trigger object within $\Delta R = 0.5$. Probe leptons are only required to pass the kinematic cuts. Pairs of tag and probe leptons are considered when the leptons are same flavor and opposite sign charge, are well separated ($\Delta R > 0.5$) and their invariant mass $m_{ll} > 50$ GeV. The ID and isolation requirements used in the analysis are tested on the probe leptons, that can either pass or fail. The ID and isolation efficiency is defined as the number of passing probes divided by the total number of probes. The final efficiencies are extracted from a fit to the di-lepton invariant mass in the mass window around the Z mass, $75 < m_{ll} < 105$ GeV, using an exponential

function to model the background and two asymmetric gaussians to model the signal. This procedure is repeated in bins of $p_T = [10, 15, 20, 25, 30, 40, 60, >60]$ GeV and η of the probe lepton. For muons, the binning in $|\eta| = [0.0, 0.9, 1.2, 2.1, 2.4]$ while for electrons $|\eta| = [0.0, 1.48, 2.1, 2.5]$. The scale factor applied to MC events is given by the ratio $\epsilon_{data}/\epsilon_{MC}$ for the (p_T, η) bin of the selected lepton.

4.5 Trigger efficiencies

Trigger efficiencies for the single muon and the $e + \mu$ triggers have been measured in data using a tag-and-probe technique. The trigger used to collect the tag-and-probe samples are HLT_IsoMu22 and HLT_Ele27_WP Loose_Gsf for the muon and electron samples, respectively. These are the triggers which the tag lepton is required to be matched to. The efficiency measurement proceeds in a similar way as for the lepton identification and isolation, described in 4.4, the main difference being the requirements on the tag and probe leptons. In this case, both the tag and the probe leptons must pass the ID and isolation requirements applied in the analysis. Passing probes are the ones firing the trigger under study. More precisely, it is required that the trigger object lies in a cone $\Delta R < 0.5$ around the offline reconstructed probe. The requirements on the tag-and-probe pair are unchanged with respect to the ones described in 4.4. For the electron and muon legs of the $e + \mu$ cross-triggers, efficiencies are determined separately for each trigger leg, with the help of a double electron (HLT_Ele23_Ele12_CaloIdL_TrackIdL_IsoVL) and a double muon (HLT_Mu17_TrkIsoVVL_Mu8_TrkIsoVVL) monitoring trigger, having the same legs of the triggers used in the analysis. The only exception occurs for the Mu23 leg, whose efficiency is measured from the Mu17 leg placing an additional cut of 23 GeV on the online reconstructed probe p_T . Efficiencies are measured as a function of (p_T, η) of the probe lepton.

The scale factor applied to correct the simulation is $\epsilon_{data}/\epsilon_{MC}$, assuming $\epsilon_{MC} = 1$, as trigger requirements are not currently applied in the analysis MC selection process. In the $e\mu$ channel, ϵ_{data} is calculated based on the following combination of efficiencies for the trigger legs:

$$\epsilon_{data} = \epsilon_{data}(\text{Mu23})\epsilon_{data}(\text{Ele12}) + \epsilon_{data}(\text{Mu8})\epsilon_{data}(\text{Ele23}) - \epsilon_{data}(\text{Mu23})\epsilon_{data}(\text{Ele23}) \quad (2)$$

For the di-tau trigger used in the $\tau_h\tau_h$ channel the efficiencies have been measured and are provided by the trigger subgroup of the Tau POG. Efficiencies are currently provided for data and for MC. To derive the efficiencies, the Tau POG applies a luminosity weighted approach to correctly handle the fact that the two HLT triggers used are from differing data Runs with no overlap. To calculate an average efficiency turn-on curve for data, the Run BCDEFG and Run H dataefficiency curves are luminosity weighted to provide an average turn on curve for all 2016 data.

The efficiencies were measured using a tag-and-probe method in the $\mu\tau_h$ final state. The tag is a well defined muon passing HLT_IsoMu20 || HLT_IsoMu22 || HLT_IsoMu24 || HLT_IsoMu27. The probe is a well defined tau passing anti-lepton discriminants and matching to the tau leg of either HLT_IsoMu21_eta2p1_MediumIsoPFTau32_Trk1_eta2p1_Reg or HLT_IsoMu21_eta2p1_MediumCombinedIsoPFTau32_Trk1_eta2p1_Reg depending on which trigger is under consideration. For MC efficiencies, only HLT_IsoMu21_eta2p1_MediumIsoPFTau32 is currently used because the CombinedIsolation trigger is still under study. This method produces efficiencies for the tau portion of this muon-tau cross trigger.

Scale factors are calculated as Lumi Weighted Data Efficiency / MC Efficiency and are applied to each τ_h leg of the double tau triggers.

294 4.6 Reweighting of LO Madgraph Drell-Yan samples

295 A reweighting is applied to Drell-Yan samples to correct the generator-level p_T and generator-
 296 level $m_{\ell\ell}$ distributions in LO madgraph samples. A correction is produced in the $Z \rightarrow \mu\mu$ con-
 297 trol region, as a function of $Z p_T$ and generator $m_{\ell\ell}$ to reduce the shape discrepancy between
 298 data and simulation. The $m_{\ell\ell}$ is defined the same way as in the recoil correction sample. The
 299 generator-level p_T is found by summing all generator particles that satisfy the (fromHardProcessFinalSta-
 300 && (isMuon || isElectron || isNeutrino)) || isDirectHardProcessTauDecayProduct
 301 requirements. The visible generator-level p_T is found the same way, but the isNeutrino re-
 302 quirement is removed.
 303 The weights are extracted from a dimuon region. Events in this region are selected by requiring
 304 two opposite sign muons passing the medium ID (medium2016 ID for runs B to F) and with
 305 a relative isolation less than 0.15. The leading muon is required to have $p_T > 26$ GeV and the
 306 subleading muon $p_T > 15$ GeV. Events with additional identified and isolated electrons and
 307 muons are discarded. The weights are computed in such a way as to make the two-dimensional
 308 distributions of the $Z p_T$ and the Z boson reconstructed mass match between data and expected
 309 backgrounds. The weights are then corrected not to introduce a general yield variation of the
 310 Drell-Yan background, but to only have a shape effect. The $\mu\mu$ distributions before and after
 311 reweighting are shown in Fig. 3, whereas the weights are illustrated in Fig. 4.

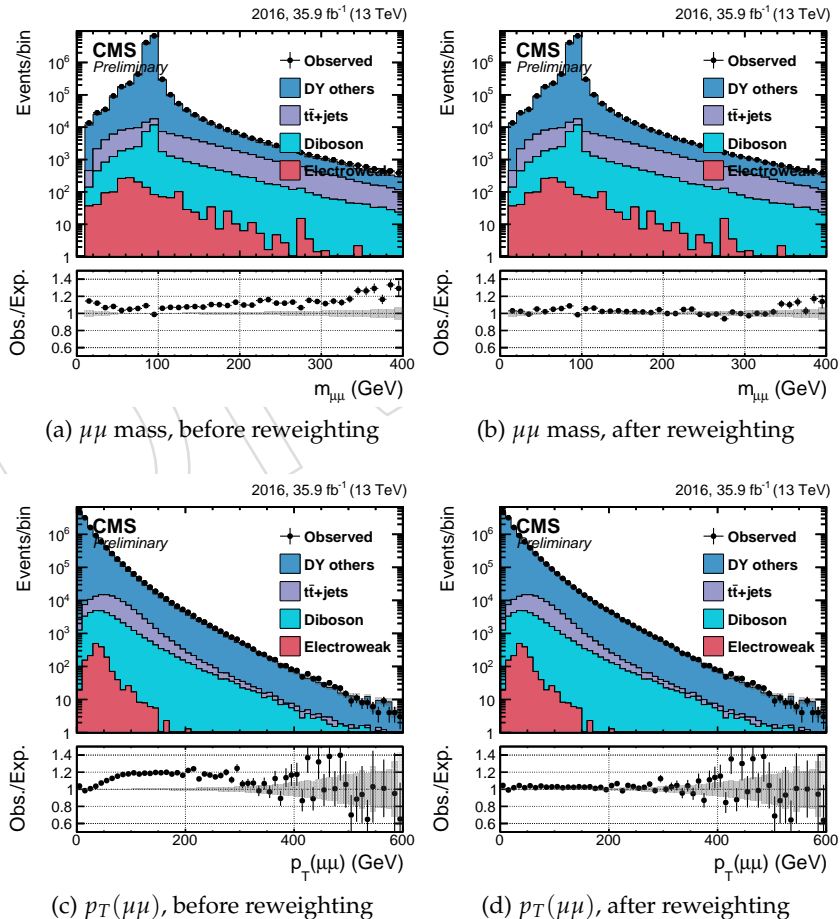


Figure 3: Di-muon mass and p_T distributions in $Z \rightarrow \mu$ data before and after the reweighting discussed in this section.

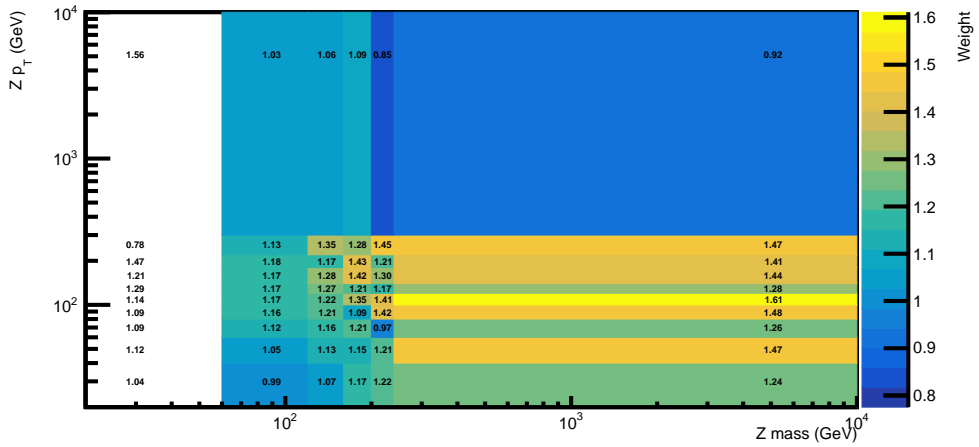


Figure 4: Weights applied to the Drell-Yan LO MC simulation based on the generated Z boson mass and p_T . These weights only correct the shape of the distribution and do not cause a variation of the process yield.

4.7 Top p_T reweighting

There is evidence that the top p_T distribution is softer in data than in simulation, so corrections are applied to account for this mismodeling. These weights are only applied to $t\bar{t}$ and not to single top samples. The uncertainty on the correction is equal to the value of the correction. The correction derived in Run-2 is applied.

4.8 Recoil corrections

Recoil corrections are applied to correct for the mismodeling of \vec{E}_T^{mis} in the simulated samples of the Drell-Yan, W+Jets and Higgs production. The corrections are performed on the variable defined as the vectorial difference of the measured missing transverse momentum and total transverse momentum of neutrinos originating from the decay of Z, W or Higgs boson.

$$\vec{U} = \vec{E}_T^{\text{mis}} - \vec{p}_{T,\nu}. \quad (3)$$

In the case of leptonically decaying boson this variable can be expressed as

$$\vec{U} = -\vec{p}_{T,B} - \vec{H}_T, \quad (4)$$

where \vec{H}_T is the transverse momentum of hadronic recoil and $\vec{p}_{T,B}$ is the transverse momentum of leptonically decaying Z, W or Higgs boson (leptonic recoil).

The vector \vec{U} is projected onto the axes parallel (U_1) and orthogonal (U_2) to the boson p_T and it is measured in $Z \rightarrow \mu\mu$ events, where leptonic recoil does not contain neutrinos and four-vector of the Z boson can be measured precisely. Events are selected by requiring the HLT_IsoMu22 trigger in data, and opposite-sign muon pairs are selected by requiring two muons with opposite charge, passing the medium HIP safe muon ID, the same impact parameter cuts as in the muon selection for the analysis, $I_{rel}^\mu < 0.15$. The leading muon must have a p_T of at least 23 GeV, with the trailing muon having a p_T of at least 10 GeV. In addition, for data events, the leading muon must have fired the HLT_IsoMu22 trigger. The requirements on muon η are $|\eta_1| < 2.1$ and $|\eta_2| < 2.4$. At pair level, the two muons must be separated by $\Delta R > 0.5$, and the di-muon

mass must be at least 20 GeV. Pile-up reweighting, the muon ID, isolation, and trigger scale factors are applied, as are the muon tracking efficiencies. The DY shape reweighting is applied to Drell-Yan MC samples. $Z \rightarrow \mu\mu$ events from around the Z peak are selected by requiring $70 < m_{\mu\mu} < 110$ GeV. The offset with respect to zero of the U_1 projection and the resolution of the $U_{1,2}$ projections are determined for both $Z \rightarrow \mu\mu$ data and MC events. A double symmetric Gaussian centered at zero is used to fit the U_2 component, while double asymmetric Gaussian with freely floating central value is used to fit the U_1 component. These fits are performed in bins of $Z p_T$ (0-10, 10-20, 20-30, 30-50, and > 50 GeV), and bins of number of jets ($N_{\text{jets}} = 0$, 1 or at least 2). From the fitted functions the mean values of the U_1 projection, $\langle U_1 \rangle$, and the resolutions of the $U_{1,2}$ projections, $\sigma(U_{1,2})$, are determined for data and simulated events as a function of $Z p_T$ and jet multiplicity. This is shown in figures 5-7.

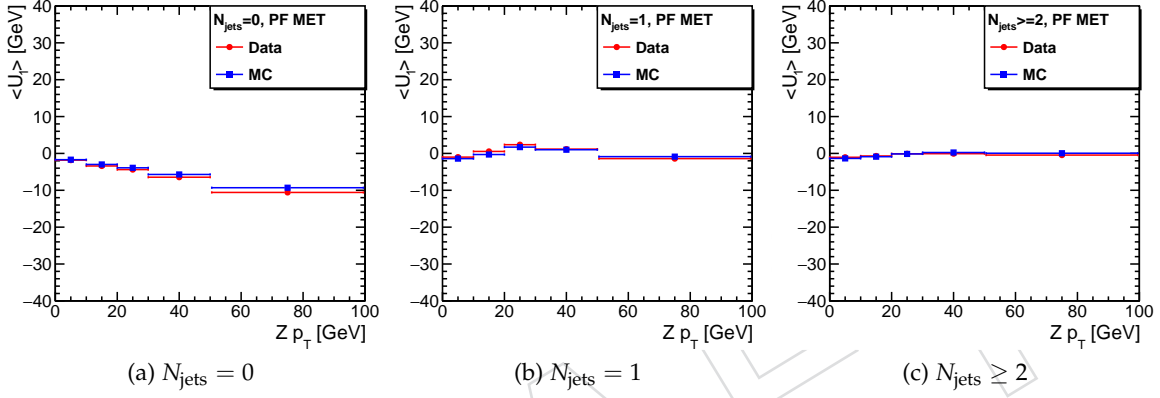


Figure 5: Mean value of U_1 in data and simulation as a function of $Z p_T$ and jet multiplicity.

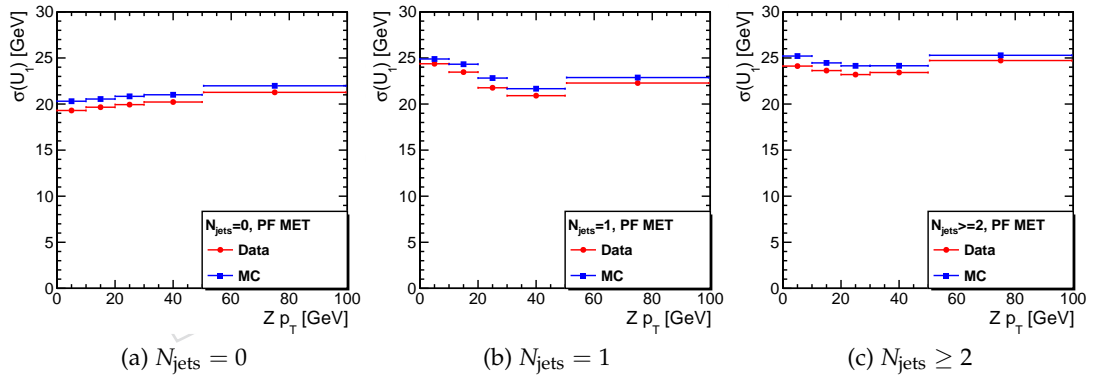


Figure 6: Resolution of the U_1 projection in data and simulation as a function of $Z p_T$ and jet multiplicity.

344 The corrections to the $U_{1,2}$ variables are computed as

$$U'_1 = \langle U_1 \rangle_{\text{data}} + (U_1 - \langle U_1 \rangle_{\text{MC}}) \frac{\sigma(U_1)_{\text{data}}}{\sigma(U_1)_{\text{MC}}}, \quad (5)$$

$$U'_2 = U_2 \frac{\sigma(U_2)_{\text{data}}}{\sigma(U_2)_{\text{MC}}}. \quad (6)$$

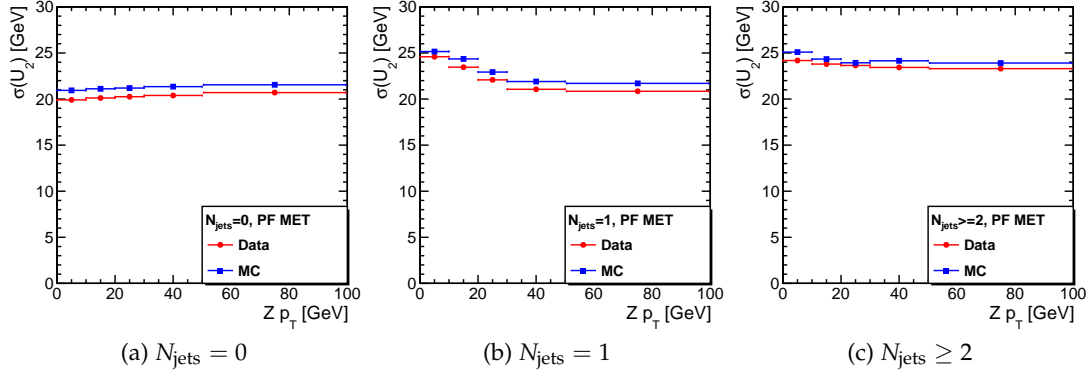


Figure 7: Resolution of U_2 in data and simulation as a function of $Z p_T$ and jet multiplicity.

- 345 The corrections are propagated to \vec{E}_T^{miss} using equation 3 and applied to the simulated samples
 346 of Drell-Yan, W+Jets and Higgs boson production.
 347 The effect of the recoil corrections on the $Z \rightarrow \mu\mu$ selection is shown in figure 8. The recoil
 348 correction improved modeling of E_T^{miss} in events without genuine missing transverse energy.

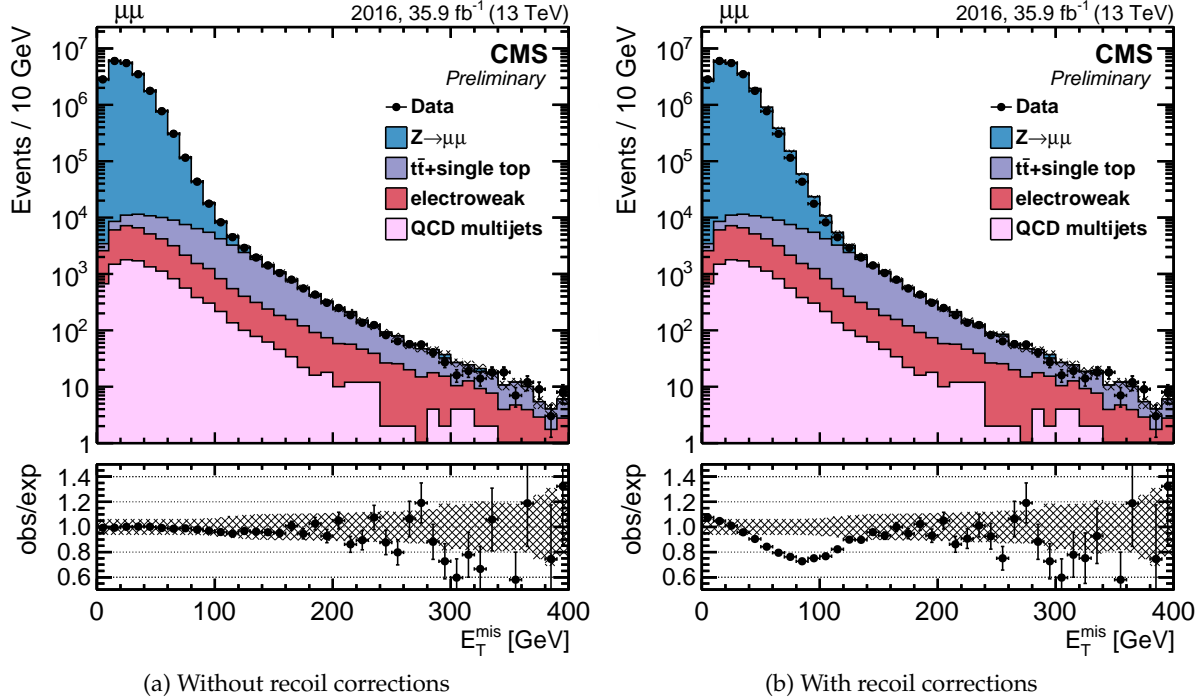


Figure 8: Effect of applying recoil corrections to the E_T^{miss} distribution in the $Z \rightarrow \mu\mu$ selection. The recoil corrections improve the agreement between data and MC.

349 4.9 Generator event weights and luminosity

- 350 Generator weights are applied on an event-by-event basis. Samples produced with the aM-
 351 CatNLO generator contain both positive and negative event weights. The aMCatNLO samples
 352 used in this analysis are diboson samples. The presence of negative event weights reduces the
 353 effective statistics of the samples.

³⁵⁴ The event weights for simulation are scaled to the expected yields for each sample. The number
³⁵⁵ of generated events in each sample is used, however in the aMCatNLO sample this sum of
³⁵⁶ generated events is weighted by the generator weights, effectively making the aMCatNLO
³⁵⁷ samples smaller when weighting for luminosity and cross section.

DRAFT

358 5 Signal extraction

359 The signal extraction for this analysis is based on fitting two-dimensional distributions. The
 360 two observables are chosen category per category as the ones with the maximal discriminative
 361 power between signal and various backgrounds.

362 In each final state, events are divided into three different categories:

- 363 • **0 jet:** This category targets events produced via gluon-gluon fusion. As the name
 364 indicates, it contains events with no jet with p_T greater than 30 GeV, $|\eta|$ less than 4.7,
 365 and passing the loose PF identification. The gluon-gluon fusion has the largest cross
 366 section for the SM Higgs boson at the LHC, but this category contains a large amount
 367 of background, including a large contribution of irreducible Drell-Yan events. This
 368 category is useful to constrain the different backgrounds with large statistics.

- 370 • **VBF:** This category targets events produced via vector boson fusion. Events are se-
 371 lected with two jets with p_T greater than 30 GeV, $|\eta|$ less than 4.7, and passing the
 372 loose PF identification. The leading two jets are required to have a large invariant
 373 mass, which effectively reduces SM backgrounds, such as $t\bar{t}$ events. The threshold
 374 on m_{jj} is 300 GeV in this analysis. The selection in the $\tau_h \tau_h$ final state is slightly dif-
 375 ferent because of the lower statistics and different background composition (mostly
 376 QCD multijet events): events with at least two jets separated by $\Delta\eta > 2.5$, and with
 377 a Higgs boson p_T , defined as the vectorial sum of the τ_h candidates and MET four-
 378 vectors, greater than 100 GeV, enter the VBF category.

- 380 • **Boosted:** This last category contains all other events that did not enter one of the pre-
 381 vious categories. It contains a mixture of boosted gluon-gluon fusion Higgs events
 382 produced in association with one or more jets, of VBF Higgs boson events where one
 383 of the jets has escaped detection or with low m_{jj} , as well as Higgs bosons produced
 384 in association with a W or a Z+jets decaying hadronically.

385 In the 0-jet category, the two variables chosen to extract the results are the visible mass between
 386 the tau candidates, as well as the transverse momentum of the hadronic tau (in $\mu\tau_h$ and $e\tau_h$)
 387 or of the muon (in $e\mu$). In the $\tau_h \tau_h$ final state however, only one dimension, the invariant mass
 388 of the di-tau pair, is considered because of the already high p_T thresholds on the hadronic
 389 taus due to trigger requirements. The visible invariant mass is chosen over the full invariant
 390 mass, which has a better resolution, because it permits to separate the signal from the poorly-
 391 described $Z \rightarrow \ell\ell$ contribution, which forms a narrow peak around the Z boson mass when
 392 the visible invariant mass is used. Signal events typically have leptons with higher p_T than
 393 other backgrounds, especially Drell-Yan events, which is the reason why the the transverse
 394 momentum of the hadronic tau (in $\mu\tau_h$ and $e\tau_h$) or of the muon (in $e\mu$), are used as second
 395 dimension in the fit. Two-dimensional distributions for the signal and various processes in the
 396 0-jet category of the $\mu\tau_h$ final state are shown in Fig. 9.

397 In the VBF category, the two variables are the invariant mass $m_{\tau\tau}$ and the invariant mass of
 398 the two leading jets, m_{jj} . The signal purity increases together with m_{jj} , but it is also important
 399 to consider intermediate m_{jj} values not to throw away any signal event. The pseudorapidity
 400 difference between the two jets is so correlated to m_{jj} that it has been found that cutting addi-
 401 tionally on this variable would not improve the sensitivity of the analysis. Two-dimensional
 402 distributions for the signal and various processes in the VBF category of the $\mu\tau_h$ final state are
 403 shown in Fig. 10.

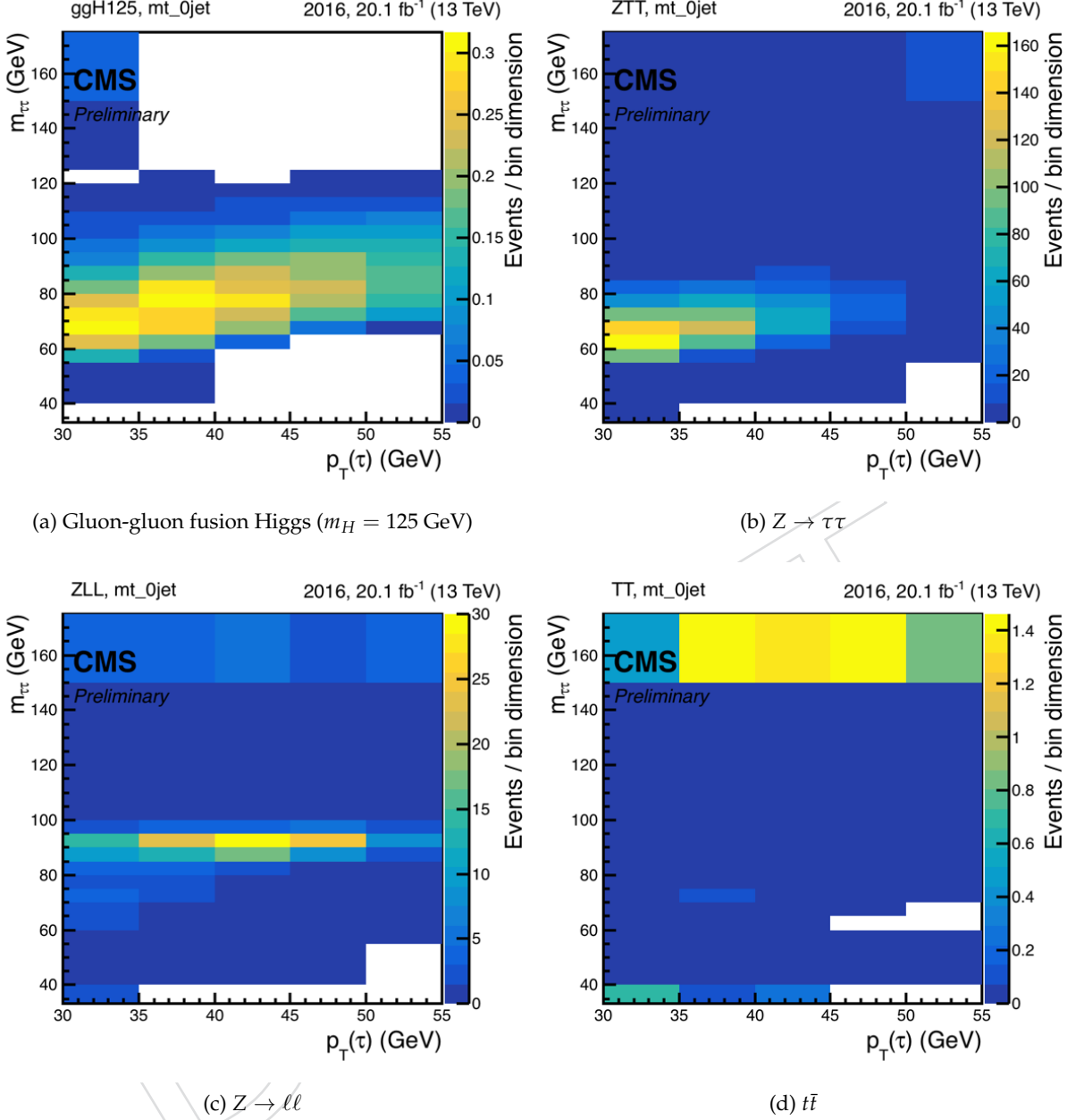


Figure 9: 2D distributions for the signal and various background processes in the $\mu\tau_h$ final state, in the 0-jet category. The y-axis is the visible invariant mass between the tau candidates, and the x-axis is the transverse momentum of the τ_h candidate. The bin contents are divided by the bin areas. MC scaling to $20.1/\text{fb}$ only used in these purely MC-based plots, MC scaled to $12.9/\text{fb}$ everywhere else.

404 In the boosted category, results are extracted from a fit to the 2D distributions of the invariant
 405 mass and of the reconstructed Higgs boson candidate p_T . The Higgs boson candidate p_T is
 406 defined as the vectorial sum of the transverse momenta of the tau candidates and of the missing
 407 transverse energy:

$$\vec{p}_T(H) = \vec{p}_T(\tau_1) + \vec{p}_T(\tau_2) + \vec{MET}. \quad (7)$$

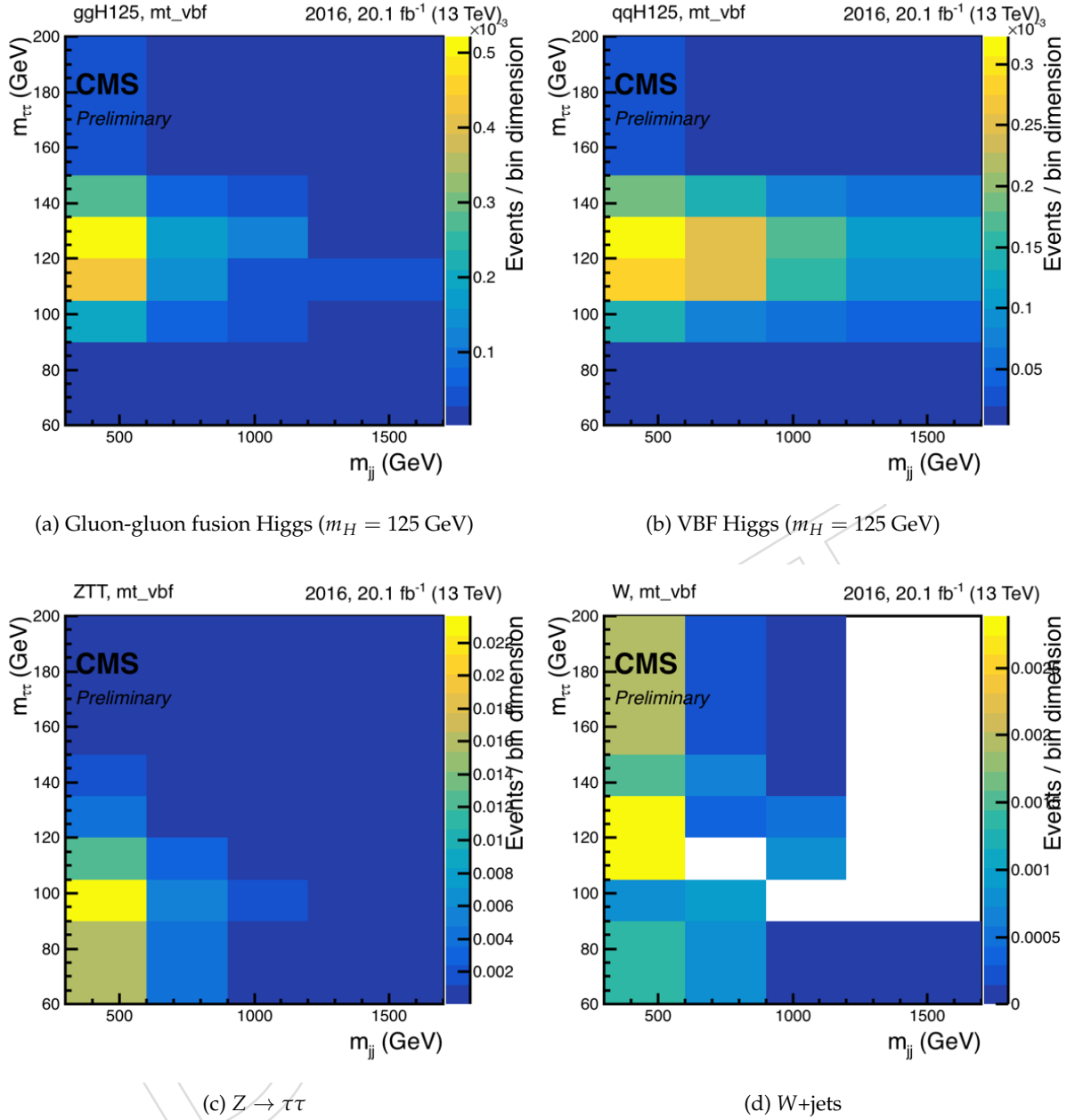


Figure 10: 2D distributions for the signal and various background processes in the $\mu\tau_h$ final state, in the VBF category. The y-axis is the invariant mass between the tau candidates, and the x-axis is the invariant mass of the two leading jets. The bin contents are divided by the bin areas. MC scaling to 20.1/fb only used in these purely MC-based plots, MC scaled to 12.9/fb everywhere else.

408 This variable is estimated by the SVfit algorithm together with the invariant mass, based on the
 409 most likely values of full p_T of the tau candidates. A higher signal purity is achieved at large
 410 Higgs boson p_T because Higgs bosons produced in association with jets in the gluon-gluon
 411 fusion tend to be boosted. In addition, Higgs boson events from associated production with
 412 W and Z bosons, and from vector boson fusion, are also boosted. At high Higgs boson p_T , SM
 413 backgrounds, such as QCD, are strongly reduced. Two-dimensional distributions for the signal

and various processes in the boosted category of the $\mu\tau_h$ final state are shown in Fig. 11.

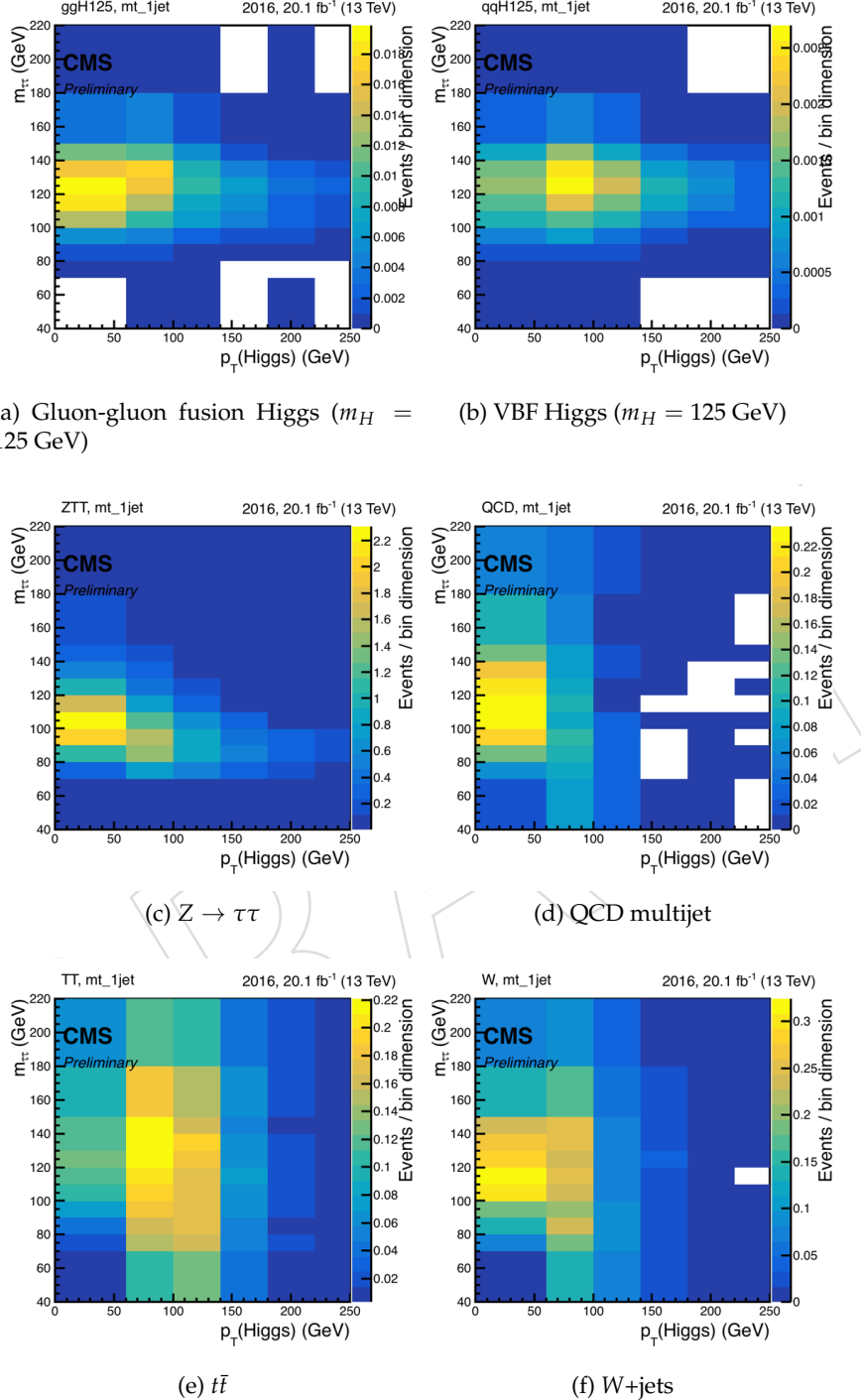


Figure 11: 2D distributions for the signal and various background processes in the $\mu\tau_h$ final state, in the boosted category. The y-axis is the visible invariant mass between the tau candidates, and the x-axis is the Higgs boson candidate p_T . The bin contents are divided by the bin areas. MC scaling to 20.1/fb only used in these purely MC-based plots, MC scaled to 12.9/fb everywhere else.

Making two-dimensional fits instead of dividing events into a variety of categories, and fitting

416 using one-dimensional mass distributions presents several advantages. First, the selection of
 417 events that enter the two-dimensional distributions is particularly straightforward, whereas 1D
 418 categories would require designing complex selection criteria based on a variety of variables,
 419 in order to achieve an optimal sensitivity. Similarly the 2D fitting introduces three categories
 420 per final state, with very similar definitions across final states, while a larger number of 1D
 421 categories would be needed (up to seven per final state in Run-1), with fine-tuned selection
 422 criteria for each final state. Additionally 2D distributions allow to keep a large number of
 423 events, even in signal-poor regions, which allows good control of the backgrounds in highly
 424 populated regions, and gives a handle to control the migrations between different bins of the
 425 distributions. Finally, the 2D procedure has a larger flexibility with respect to the integrated
 426 luminosity: more data allows to simply add additional bins in the 2D distributions, whereas
 427 new optimization studies would be needed to fine-tune the definitions of the 1D categories.

428 6 The $\mu\tau_h$ final state

429 6.1 Trigger requirements

430 Events are recorded using `HLT_IsoMu22` or `HLT_IsoTkMu22` or `IsoMu22_eta2p1` or `IsoTkMu22_eta2p1`
 431 or `HLT_IsoMu19_eta2p1_LooseIsoPFTau20*` triggers. The selected muon candidate must
 432 be matched to the HLT muon within $\Delta R < 0.5$. All trigger paths are summarized in Table 5.
 433 The trigger selection is required for MC simulations. Please see section on trigger efficiencies.
 434 Events with a muon with p_T between 20 and 23 GeV are required to fire the cross trigger, and
 435 the corresponding data/MC trigger scale factor is applied to MC events. Events with a muon
 436 with p_T greater than 23 GeV are required to fire the single lepton trigger, and the corresponding
 437 data/MC trigger scale factor is applied to MC events. Including events with a muon with p_T
 438 between 20 and 23 GeV increases the signal acceptance by about 25%, and the analysis sensi-
 439 tivity by a bit more than 10%.

HLT Trigger	Runs available	Notes
<code>HLT_IsoMu22_v*</code>	B,C,D,E,F	This is the required trigger for all data events
<code>HLT_IsoTrkMu22_v*</code>	B,C,D,E,F	This is the required trigger for all data events
<code>HLT_IsoMu22_eta2p1_v*</code>	C,D,E,FG,H	This is the required trigger for all data events
<code>HLT_IsoTrkMu22_eta2p1_v*</code>	C,D,E,FG,H	This is the required trigger for all data events
<code>HLT_IsoMu19_eta2p1_LooseIsoPFTau20_SingleL1_v*</code>	B,C,D,E,F,G,H	This is the required trigger for all data events.
<code>HLT_IsoMu19_eta2p1_LooseIsoPFTau20_v*</code>	B,C,D,E,F,G,H	Seeded by single L1 muon. This is the required trigger for all data events.
		Seeded by both L1 tau and L1 muon.

Table 5: List of relevant HLT triggers for the $\mu\tau_h$ final state.

440 6.2 Event selection

441 An event is selected if at least one $\mu\tau_h$ pair is found. In case more than one muon or τ_h is found
 442 in the event, the most isolated objects are taken. In case of equal isolation, the highest p_T objects
 443 are taken. The μ and τ_h must have opposite sign (OS) electric charges and must be separated
 444 by $\Delta R > 0.5$.

445 The muon is required to pass the following criteria:

- 446 • The μ is required to pass the ICHEP Medium Muon ID developed by the Muon POG
 447 for Run B,C,D,E,F dataset. This identification criteria is resistant to HIP effects. On
 448 simulated events, and in events recorded in Runs G,H the muon is required to pass
 449 the Standard Medium ID.

- The muon must have $p_{T,\mu} > 20 \text{ GeV}$ that is 1 GeV above the HLT trigger p_T threshold for the cross trigger. The triggers applied are eta restricted, thus muon must satisfy $|\eta_\mu| < 2.1$ requirement.
- The delta-beta muon isolation that is defined within a cone of $\Delta R < 0.4$ around the muon must be less than 0.15. This is the tight working point suggested by the Muon POG.
- The muon track must match to the primary vertex satisfying the requirements on the impact parameters in the longitudinal direction, and in the transverse plane $dZ < 0.2 \text{ cm}$ and $d0 < 0.045 \text{ cm}$.

The τ_h candidate is required to pass the following criteria:

- The τ_h must be identified as 1- or 3-prong according to discriminator `byDecayModeFinding`
- The τ_h must satisfy the tight working point of the MVA-based isolation trained for Run II analysis by Tau POG: `byTightIsolationMVArun2v1DBoldDMwLT > 0.5`.
- $p_{T,\tau_h} > 30 \text{ GeV}$ and $|\eta_{\tau_h}| < 2.3$;
- Selected τ_h must match to the primary vertex satisfying requirement $dZ_\tau < 0.2 \text{ cm}$.
- To reduce contribution from background processes where lepton (electron or muon) is misidentified as a hadronic tau the selected τ_h must satisfy anti-lepton discriminators `againstMuonTight3` and `againstElectronVLooseMVA6`. The tight working point of the discriminator against muon is chosen to reduce the large $Z \rightarrow \mu\mu$ background. A looser working point is chosen for the discriminator against electrons to keep a high signal efficiency, and because few backgrounds have an electron and a muon in the final state.

6.2.1 Transverse mass

The transverse mass, M_T , from a muon and missing transverse energy is defined as given in Eq 8:

$$M_T = \sqrt{2p_T^\ell E_T^{\text{miss}}(1 - \cos(\phi))}, \quad (8)$$

where p_T^ℓ and E_T^{miss} are transverse momentum of the muon and missing transverse energy, and ϕ is an angle between these two objects in transverse plane. The distribution of M_T in signal and background processes is shown in Fig. 12.

The transverse mass in signal processes is expected to be small, while for some dominant background processes, such as $W+\text{jets}$ and $t\bar{t}$, it is expected to be large. Thus, selected events must satisfy a requirement $M_T < 50 \text{ GeV}$. The threshold is obtained by an optimization scan using $S/\sqrt{S+B}$, as seen in Fig.13.

6.2.2 Third lepton veto

An event is rejected if an extra lepton, muon or electron, which passes a `Loose` selection is found in the event. This ensures that there is no overlap between the different channels. The third lepton veto also reduces contribution from $DY+\text{Jets}$. If, in a $\mu\tau$ event, there is one more loose OS μ , then the event is vetoed, as it is likely that the reconstructed hadronic tau was faked by a jet.

The loose electron is defined as follows:

- $p_{Te} > 10 \text{ GeV}$

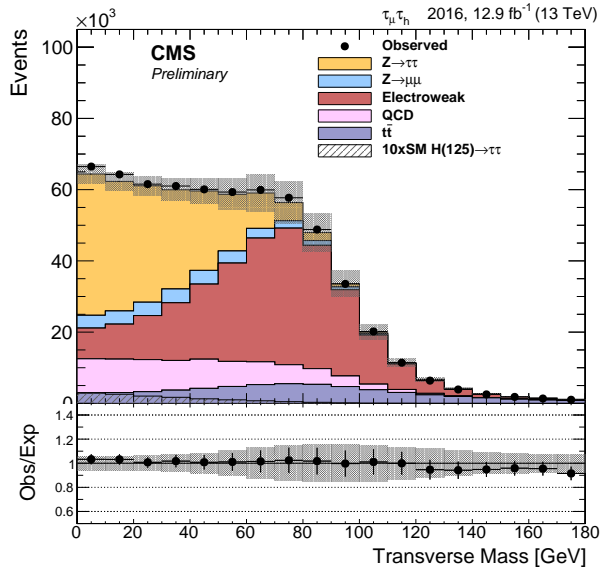


Figure 12: $\mu\tau_h$ before M_T cut, with no QCD subtraction used in the W sideband method.

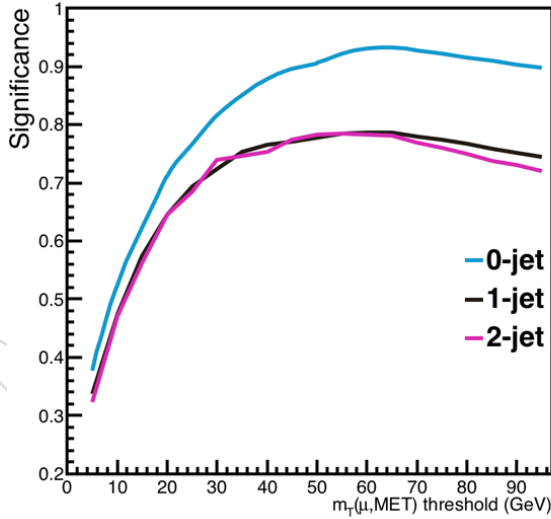


Figure 13: Signal significance as a function of the M_T cut applied in the $\mu\tau_h$ selection.

- $|\eta_e| < 2.5$
- $dXY_e < 0.045$
- $dZ_e < 0.2$
- e MVA-based 90% efficiency working point.
- e passes Conversion veto, `passConversionVeto`.
- e track has ≤ 1 missing inner track hit.
- e is loosely isolated, require corrected relative isolation $\text{iso}_e < 0.3$.

The loose muon is selected as follows:

- 496 • $p_{T\mu} > 10 \text{ GeV}$
- 497 • $\eta_\mu < 2.4$
- 498 • $dXY_\mu < 0.045$
- 499 • $dZ_\mu < 0.2$
- 500 • μ passes medium ID working point. The μ is required to pass the ICHEP Medium
501 Muon ID for Run B,C,D,E,F dataset. On simulated events and in events recorded in
502 Runs G,H the μ is required to pass the Standard Medium ID.
- 503 • μ is loosely isolated $\text{iso}_\mu < 0.3$.

504 6.3 Background estimation

505 6.3.1 Drell-Yan

506 For all Z+Jets backgrounds a correction related to the generated mass and p_T is applied as
507 described in section 4.6.

508 The MC description is checked in $Z \rightarrow \mu\mu$ events. The $Z \rightarrow \mu\mu$ enriched region is obtained
509 by selecting events with two OS muons passing the medium muon ID (medium 2016 for runs
510 B to F, medium for runs G and H), with relative isolation less than 0.15, $p_T > 26 \text{ GeV}$, and
511 $|\eta| < 2.1$. The events are required to fire `HLT_IsoMu24_v*` OR `HLT_IsoTkMu24_v*`. The
512 purity is increased by requiring the visible mass of the muons to be between 70 and 110 GeV.
513 Events with additional electrons or muons are vetoed. The events are divided into the same 2D
514 categories as in the signal region. The data/MC distributions are shown in Fig. 14 for the 0 jet,
515 VBF, and boosted categories.

516 The Higgs p_T , which is one of the fitting variables in the boosted category, is equivalent to the
517 dimuon p_T in dimuon events. It is well modeled in MC simulation because the simulation
518 has already been reweighted to match the Z boson mass and p_T distributions in data. Some
519 data/MC differences are observed as a function of the invariant mass of the leading jets in the
520 VBF category.

521 The scale factors are remeasured after selecting muons with higher p_T thresholds in order to be
522 closer to the kinematic selection in the signal regions, where the taus before decaying should
523 have large p_T to give, for example, a muon with $p_T > 20 \text{ GeV}$ and a τ_h with $p_T > 30 \text{ GeV}$. In the
524 case of the VBF category, the scale factors become flat when selecting muons with a higher p_T
525 threshold, as shown in Fig. 6.3.1 for a threshold of 50 GeV on both muons. Therefore half of the
526 scale factors measured with a threshold of 25 GeV are applied to the nominal shapes, whereas
527 the scale factors obtained with 25 GeV as a threshold, and no scale factor, are considered as two
528 alternative shapes as systematic uncertainties.

529 The Z+Jets backgrounds are separated into 3 main components based on whether or not the τ_h
530 candidate is matched at generator-level to a true generated τ_h . The components are labeled in
531 the following fashion:

- 532 • If the tau is matched to generator-level hadronically decaying tau, then it is classified
533 as ZTT.
- 534 • If the tau is matched to generator-level prompt lepton, then it is classified as ZL.
- 535 • All other cases are classified as a jet faking a tau and it is classified as ZJ.

536 Additional systematic uncertainty is assigned based on the recommendation from the Tau POG
537 for leptons faking τ_h 's. ZJ is estimated in a similar fashion with additional systematic uncer-
538 tainty applied to account for jet $\rightarrow \tau_h$ fake efficiency uncertainty between data and MC.

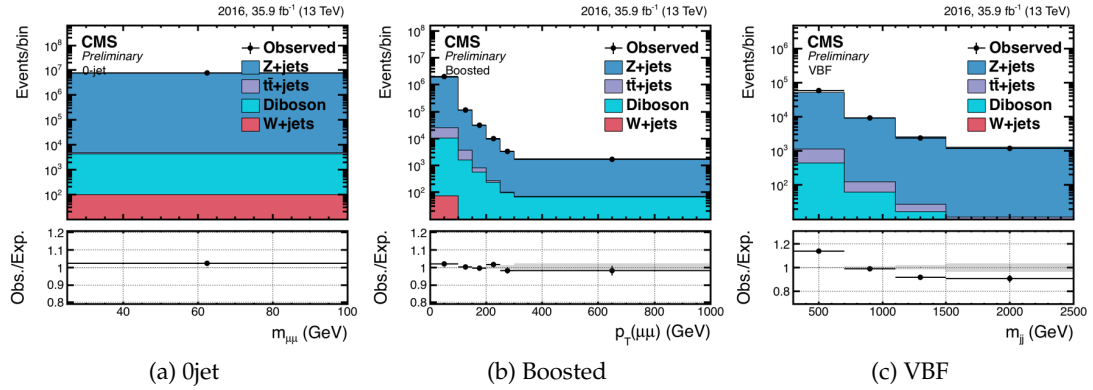


Figure 14: Data/MC comparison in a $Z \rightarrow \mu\mu$ control region. The data/MC ratio are applied as scale factors for the $Z \rightarrow \tau\tau$ background in the signal region.

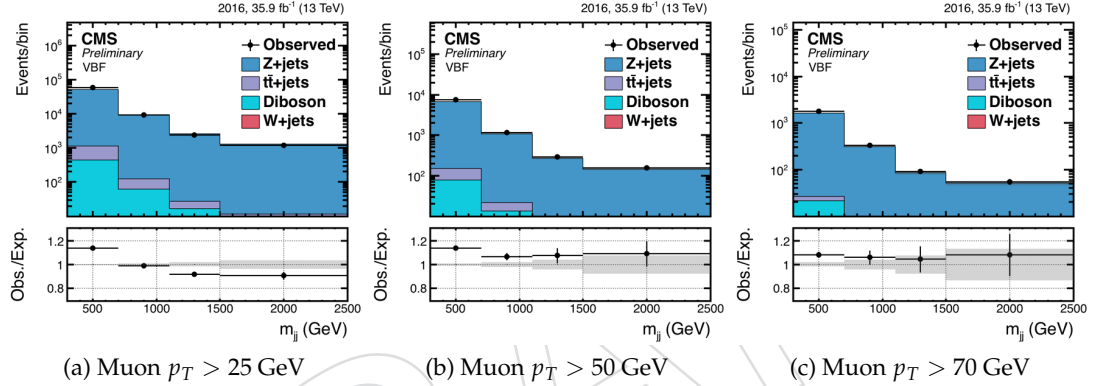


Figure 15: Data/MC comparison in a $Z \rightarrow \mu\mu$ control region in the VBF category, for different muon p_T thresholds.

539 6.3.2 $t\bar{t}$

540 The $t\bar{t}$ background is separated into two main components based on the generator-level matching
541 information of the hadronic tau:

- 542 • If the tau is matched to generator-level hadronically decaying tau, then it is classified
543 as TTT.
- 544 • Otherwise it is classified as TTJ, as it most likely that a jet faked the reconstructed
545 hadronic tau.

546 The normalization of the $t\bar{t}$ background is estimated from a $t\bar{t}$ -enriched control region, as de-
547 tailed in Section 10.

548 Additional corrections/systematic uncertainty are assigned based on whether or not the τ_h is a
549 true τ_h or faked by a jet or lighter lepton.

550 6.3.3 W+Jets background

551 Events selected with the requirement $M_T > 80\text{GeV}$ are used to check the normalization of
552 the W+Jets background. This high- M_T is dominated by the W+Jets background, but there is
553 contribution from other processes as well. In particular, with the increase of QCD cross section

554 in Run II, we expect a larger fraction of QCD in the high- M_T region than in the Run I analysis.
 555 New background methods are developed to account for this infiltration of QCD. The W+Jets
 556 shape and yield are found separately for the signal $M_T < 50\text{ GeV}$ region.

In this OS high- M_T sideband, denoted $_{OS,W}$, the W+jets yield is found by subtracting all expected backgrounds from observed data as follows:

$$W_{yield,OS,W} = \text{DATA}_{OS,W} - \text{VV,St,Other,EWK}_{OS,W} \\ - \text{DY}_{OS,W} - \text{TT}_{OS,W} - \text{QCD}_{OS,W} \quad (9)$$

557 Here, all but QCD background prediction are estimated using simulation. The data-driven
 558 QCD $_{OS,W}$ is found from the same-sign (SS) high M_T events, by subtracting MC from data
 559 and multiplying by a factor for QCD to go from same-sign to opposite sign:

$$QCD_{OS,W} = \text{QCD OSSS factor} \times \\ (\text{DATA}_{SS,W} - \text{VV,St,Other EWK}_{SS,W} - \text{DY}_{SS,W} - \text{TT}_{SS,W} - W_{SS,W}), \quad (10)$$

560 where the QCD OSSS factor is found as detailed in section 6.3.4. The QCD definition is de-
 561 pendent on the $W_{SS,W}$ yield but it is a second order effect to the overall QCD impact in the
 562 opposite-sign W sideband. The effect on the W normalization at this stage will be roughly 20
 563 % of 20%. The estimated $W_{yield,OS,W}$ yield is extrapolated to the signal region ($M_T < 50\text{ GeV}$)
 564 by a factor obtained from the W+Jets simulation.

$$W_{OS,LowMt} = \text{High-Low W factor} \times W_{yield,OS,W} \\ = \left(\frac{W_{\text{relaxed lowMT MC}}}{W_{\text{relaxed W MC}}} \right) \times W_{yield,OS,W} \quad (11)$$

565 where the $W_{\text{relaxed lowMT MC}}$ is the $M_T < 50\text{ GeV}$ yield using a relaxed event selection in sim-
 566 ulation, and likewise the $W_{\text{relaxed W MC}}$ is the $M_T > 80\text{ GeV}$ yield from simulation with a relaxed
 567 event selection. This High-Low W factor allows us to get the W estimation for the signal re-
 568 gion. The overall normalization W_{SF} of the data-driven W method compared to the MC-only
 569 yield, defined as

$$W_{SF} = \frac{W_{yield,OS,W}}{W_{\text{MC yield,OS, W}}} \quad (12)$$

570 will be used later in the QCD method.

571 The shape of the W+jets process is estimated from simulation. A relaxed selection is used; it is
 572 the same as described in section 6.3.5. The relaxed selection is verified not to bias the shape of
 573 the W+jets distributions, while reducing statistical fluctuations. The shape is then normalized
 574 to $W_{yield,OS,W}$, the yield in the signal region with the full selection. The W method is repeated
 575 for each category.

576 In practice the VBF category at high m_T has a low W purity, and no difference is expected
 577 between the W data/MC scaling in the boosted and VBF regions because they both target
 578 events with several jets. Therefore, two control regions (0 jet and boosted) with $M_T > 80\text{ GeV}$
 579 are included as control regions in the final fit to constrain dynamically the normalization of the
 580 W+jets process. The W+jets in the VBF signal region is linked to the boosted control region.
 581 normalization of the W+jets process.

582 **6.3.4 QCD multijet**

583 QCD multijet events are estimated using the same-sign low-transverse mass ($M_T < 50$) events
 584 in data, denoted $_{SS,Low}$. The contribution from other background processes is subtracted from
 585 data. Shape is relaxed according to section 6.3.5. The remaining yield is scaled by a factor
 586 describing ratio of OS to SS events in QCD dominated region containing anti-isolated muons.
 587 This factor is measured independently for each category and these results are summarized in
 588 Table 6. The distributions in the regions with anti-isolated muons, from which the scale factors
 589 are extracted, are shown in Fig. 16.

The QCD yield is found as follows:

$$QCD_{Yield,OS,Low} = QCD \text{ OSSF factor} \times \\ (\text{DATA}_{SS,Low} - VV, St, \text{Other EWK}_{SS,Low} - DY_{SS,Low} - TT_{SS,Low} - W_{SF} \times (W_{SS,Low})) \quad (13)$$

590 The QCD shape is similarly taken from Eq. 13, though all the MC simulations and data distri-
 591 butions are obtained with the relaxed selection for the boosted and VBF categories.

Category	OS/SS QCD ratio	Error	Proportion of W in high M_T SS	Proportion of QCD in high M_T OS
0-jet	1.07	15 %	0.72	0.18
Boosted	1.06	15 %	0.50	0.16
VBF	1.00	30 %	0.50	0.28

Table 6: QCD OS/SS ratios measured in the $\mu\tau_h$ final state.

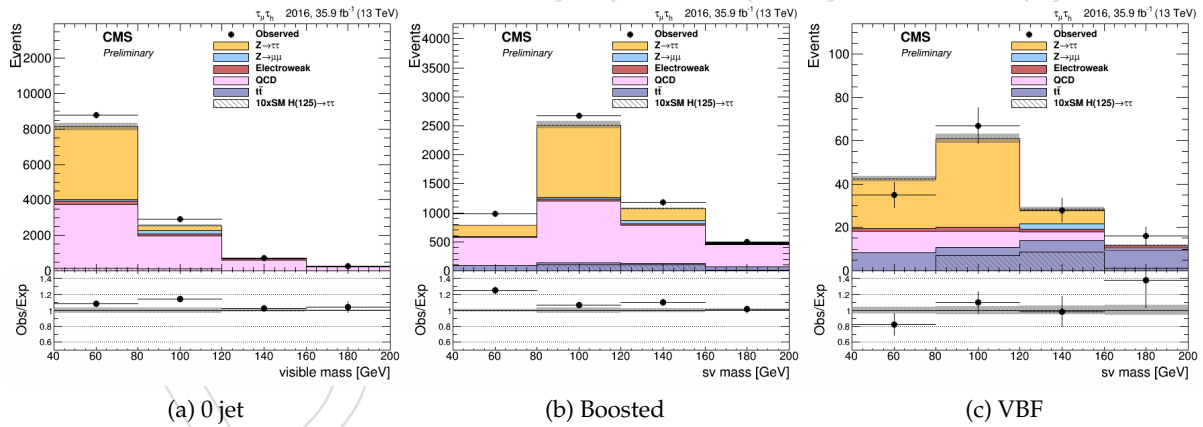


Figure 16: Anti-isolated regions used to compute the QCD OS/SS scale factors in the $\mu\tau_h$ final state.

592 **6.3.5 Relaxed selection**

593 To improve statistics in distributions of some of the background processes a relaxed selection
 594 is used. The selection is determined so that it does not bias the shape of the distribution.
 595 Kolmogorov-Smirnov tests were performed between the nominal and various loosened isol-
 596 ation working points to determine the most relaxed, high statistics shape that is still compatible
 597 with the original nominal shape. The criteria used to determine whether distributions were
 598 compatible was that the KS test values between the two shapes must be ≥ 0.10 . A KS test
 599 result $\ll 1$ indicates incompatibility. The relaxed selection that uses looser isolation criteria
 600 for muons (electrons in the $e\tau_h$ final state) is chosen. The relative delta-beta corrected muon

isolation is loosened to < 0.3 (from < 0.15) and the tau ID is loosened to the Medium MVA working point. The extra lepton vetoes are the same as in the signal region, as well as the other τ_h or muon (electron in $e\tau_h$) identification criteria. The relaxed selection is most important in the boosted and VBF categories.

The KS test indicates the relaxed selection is not incompatible with the nominal selection. However, the KS test does not show whether any other potential biases could be expected by using a relaxed selection. Relaxed selection bias tests are performed on the limits using the relaxed QCD multijet and W+Jets shapes, as illustrated in Fig 17 and 18, for the boosted and VBF categories, respectively. The bias tests consist in comparing the expected limits obtained with an Asimov dataset generated based on the non-relaxed shapes considering either the relaxed or non-relaxed background shape. Both expected limits are highly compatible with each other.

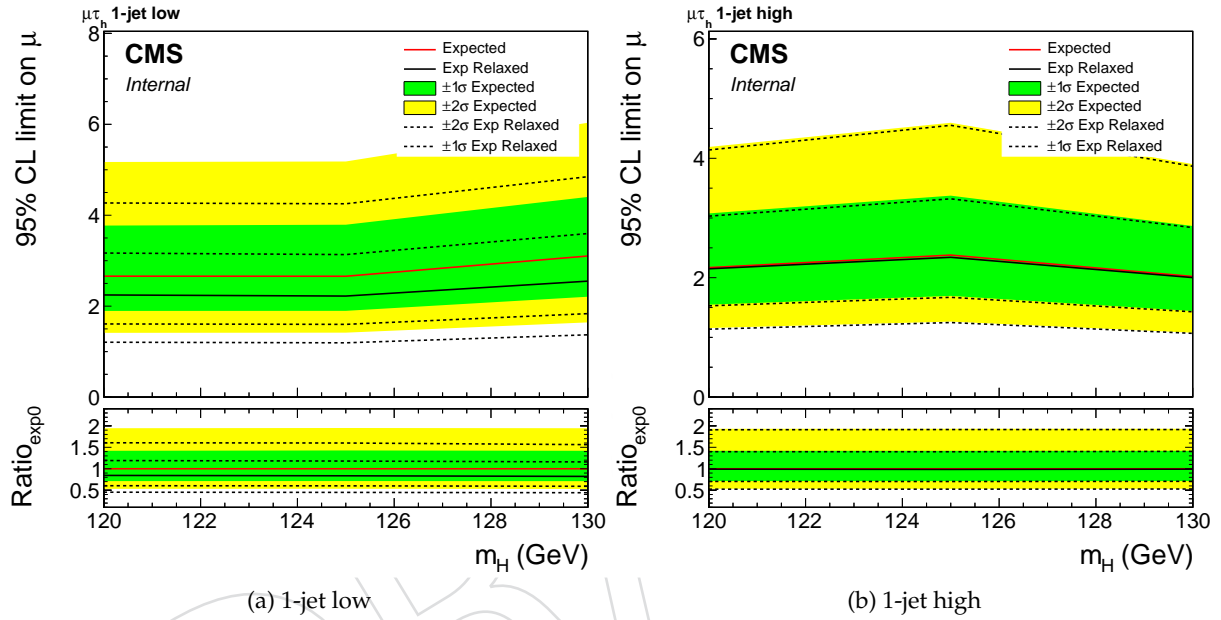


Figure 17: Bias test results in 1-jet 1D categories.

6.4 Signal extraction

6.4.1 SVFit and Visible Mass

The SVfit algorithm is used to reconstruct the di-tau mass that is used as final observable in the boosted and VBF categories. For 0-jet categories visible mass is used for signal extraction as separation between signal and the $Z \rightarrow \ell\ell$ background is much better with the m_{vis} than with the SVfit. The leptons from Drell-Yan that fake taus have a reconstructed mass at 90 GeV, while other taus and fakes peak closer to 60 GeV. Comparison of visible mass and SVfit distributions in 0-jet category can be seen in Fig. 19.

More information about the 2D signal extraction can be found in Section 5. The definition of the three 2D categories in the case of the $\mu\tau_h$ final state is given in Tab. 7.

The definition of optimized 1D categories, following the same approach as the legacy 2012 Higgs search, is presented in Tab. 8. In practice these categories are not used to extract the results as the 2D fit is the chosen method.

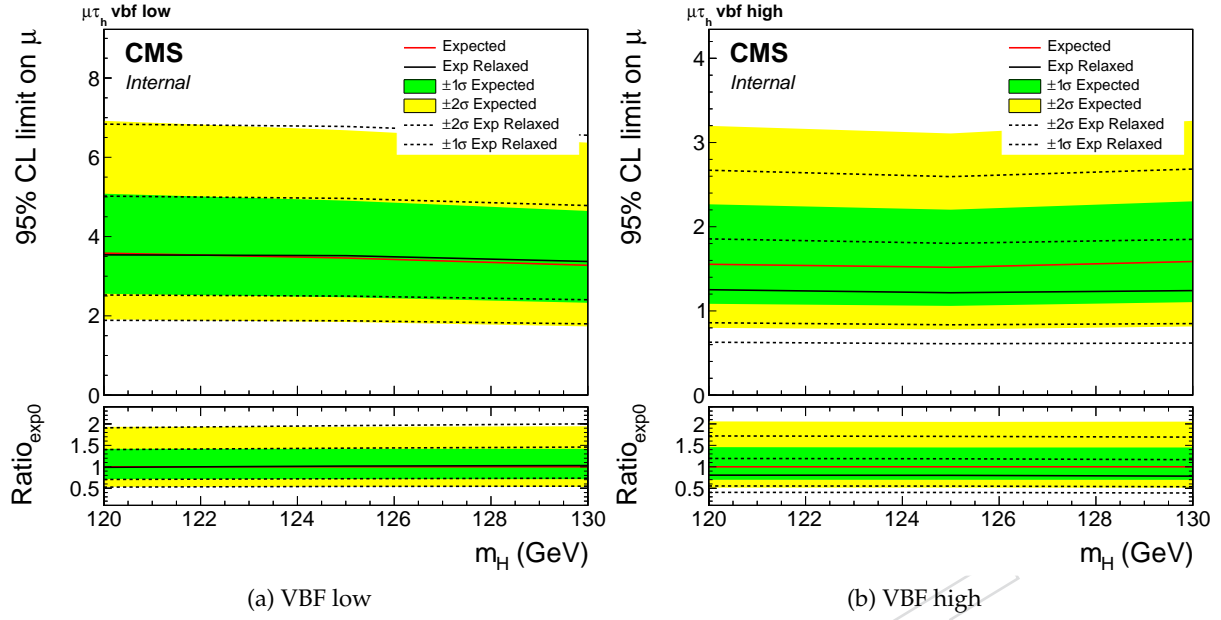
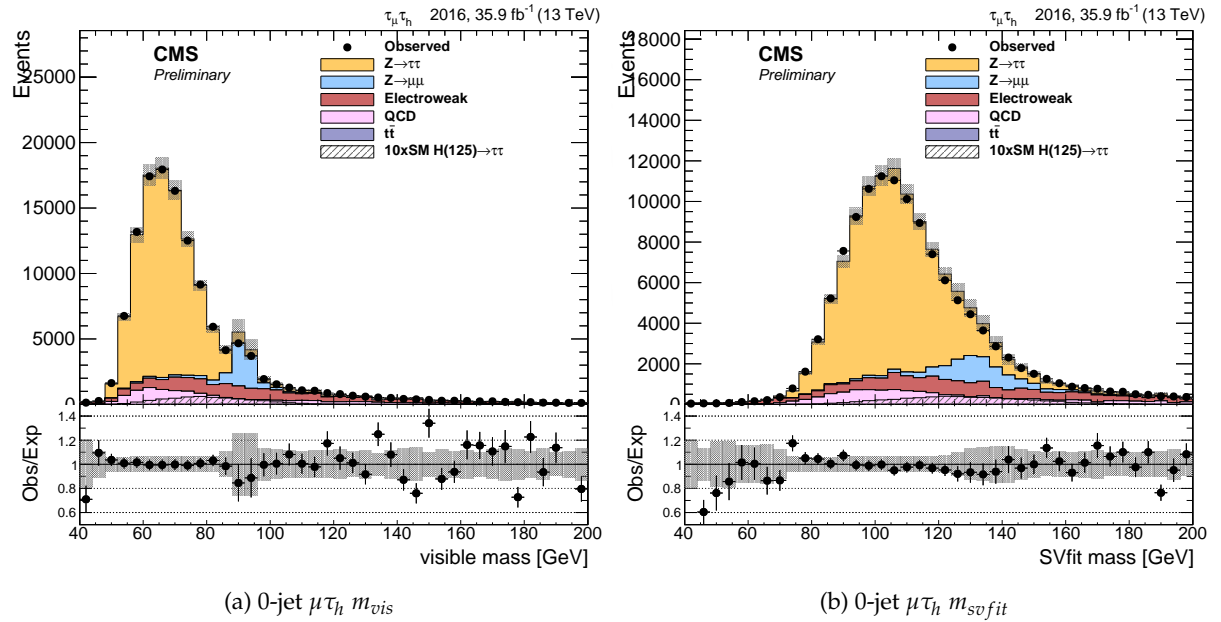


Figure 18: Bias test results in VBF 1D categories.

Figure 19: Prefit comparison of SVfit mass and visible mass in the 0 jet category. In the above plots the $p_{T,\tau} > 20$ GeV.

6.4.2 0-jet Signal Extraction

The 0-jet category is helpful for constraining systematics and targeting the gluon-gluon production. The distribution is unrolled in three bins of reconstructed decay τ decay mode: 1 prong, 1 prong + π^0 (s), 3 prongs. The main advantage of separating the reconstructed τ decay modes is that the $Z \rightarrow \mu\mu$ background with a muon faking a τ_h is absent in the 3prong decay modes, whereas it is a large contribution in the 1 prong decay mode.

Category	Definition
0-jet	$p_{T,\tau_h} > 30 \text{ GeV}$, $\text{njets} = 0$, $M_T < 50 \text{ GeV}$
Boosted	$p_{T,\tau_h} > 30 \text{ GeV}$, ($\text{njets} = 1$ or ($\text{njets} \geq 2$ and ($m_{jj} \leq 300 \text{ GeV}$ or $p_{T,\tau_h} \leq 40 \text{ GeV}$ or $p_T(H) \leq 50 \text{ GeV}$)), $M_T < 50 \text{ GeV}$)
VBF	$p_{T,\tau_h} > 40 \text{ GeV}$, $\text{njets} \geq 2$, $m_{jj} > 300 \text{ GeV}$, $p_T(H) > 50 \text{ GeV}$, $M_T < 50 \text{ GeV}$

Table 7: Category definition for the 2D analysis in the $\mu\tau_h$ channel.

Category	Definition
0-jet low	$p_{T,\tau} > 20 \text{ GeV}$ and $p_{T,\tau} < 50$ and $\text{njets} == 0$ and $M_T < 50 \text{ GeV}$
0-jet high	$p_{T,\tau} > 50 \text{ GeV}$ and $\text{njets} == 0$ and $M_T < 50 \text{ GeV}$
1-jet low	($\text{njets} == 1$ or ($\text{njets} == 2$ and $m_{jj} < 500 \text{ GeV}$)) and $p_{T,\tau} > 30 \text{ GeV}$ and ($p_{T,\tau} < 40$ or $p_{Thiggs} < 140$) and $M_T < 50 \text{ GeV}$
1-jet high	$p_{T,\tau} > 40 \text{ GeV}$ and ($\text{njets} == 1$ or ($\text{njets} == 2$ and $m_{jj} < 500 \text{ GeV}$)) and $p_{Thiggs} > 140$ and $M_T < 50 \text{ GeV}$
vbf low	$p_{T,\tau} > 20 \text{ GeV}$ and $\text{njets} == 2$ and $m_{jj} > 500$ and ($m_{jj} < 800$ or $p_{Thiggs} < 100$) and $M_T < 50 \text{ GeV}$
vbf high	$p_{T,\tau} > 20 \text{ GeV}$ and $\text{njets} == 2$ and $m_{jj} > 800$ and $p_{Thiggs} < 100$ and $M_T < 50 \text{ GeV}$

Table 8: Category definition for the 1D analysis in the $\mu\tau_h$ channel.

631 The anti-lepton discriminators were measured in an inclusive selection for the TAU POG. How-
 632 ever we find a variation in the energy scale and the SF depending on the decay Mode of the
 633 reconstructed τ_h , this can be seen in figure 20. The simulation yields except for ZL(lepton fak-
 634 ing tau) are subtracted from the data. Data, and ZL are fit with gaussians to extroplate the m_{vis}
 635 shift and scale factor correction per decay mode. The results are in 9.

	1-Prong Decay Mode	1-Prong + $\pi^0(s)$	3-Prong
$\mu\tau_h M_{vis}$ ES Correction	$1\% \pm 0.3\%$	- $\pm 0.4\%$	-
$\mu\tau_h \mu \rightarrow \tau_h$ fake rate correction	$0.74 (\pm 25\%)$	$1.0 (\pm 25\%)$	-

Table 9: 0-jet M_{vis} $\mu \rightarrow \tau_h$ fake rate corrections.

636 6.5 Control plots

637 A few control plots for the $\mu\tau_h$ final state are shown in Figs 21 to 23.
 638 The postfit distributions for unrolled 2D distributions are shown in Figs 24, 25, 26.

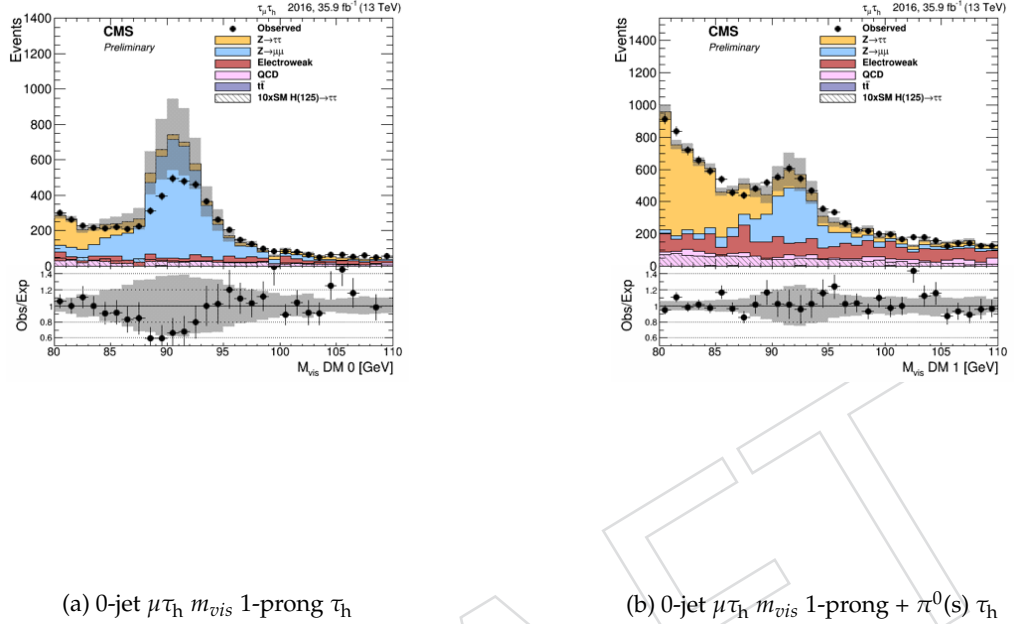


Figure 20: Prefit comparison of visible mass in the 0 jet category per τ_h decay mode in 1-prong and 1-prong + $\pi^0(s)$.

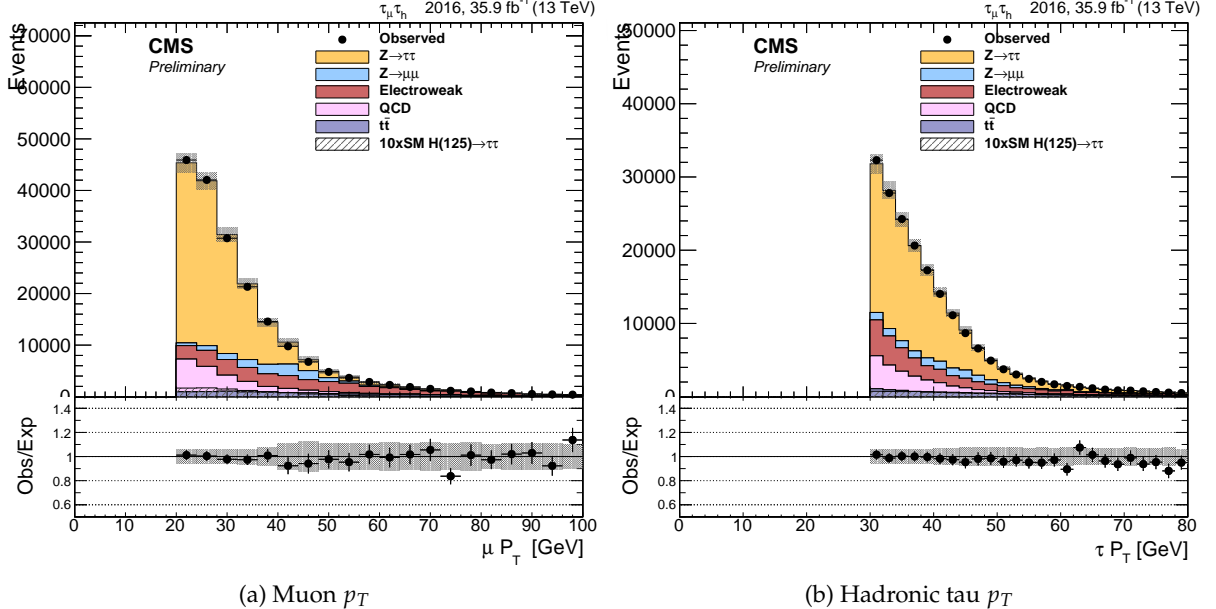


Figure 21: Prefit control distributions of the muon and tau p_T in the $\mu\tau_h$ final state before dividing into categories.

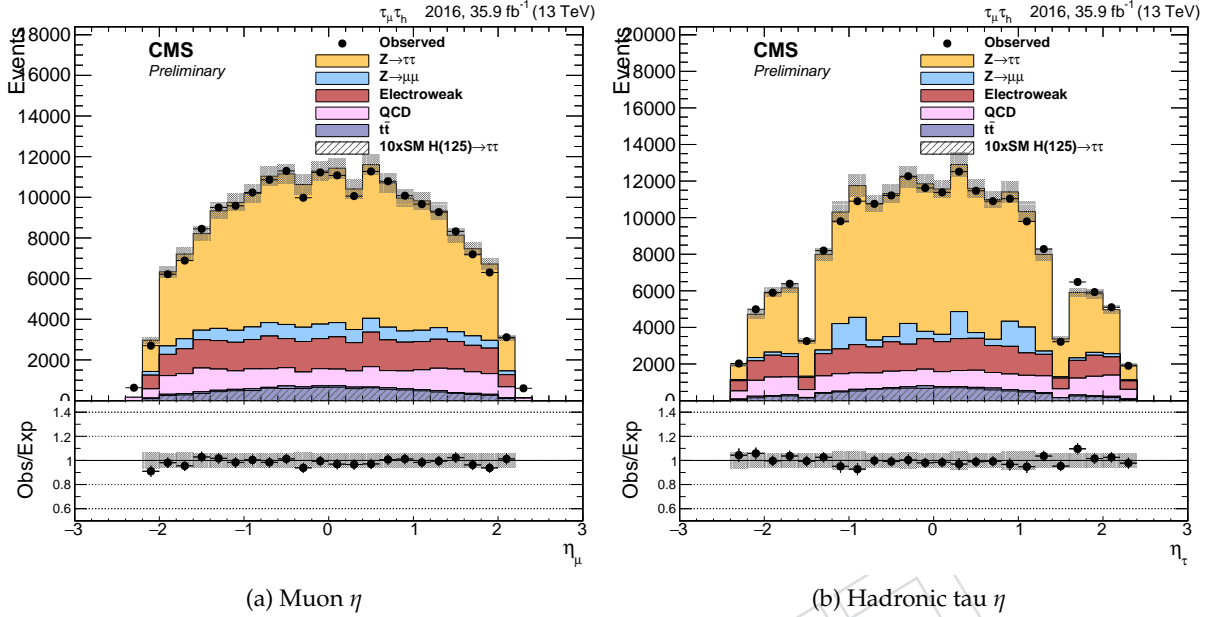


Figure 22: Prefit control distributions of the muon and tau pseudorapidities in the $\mu\tau_h$ final state before dividing into categories.

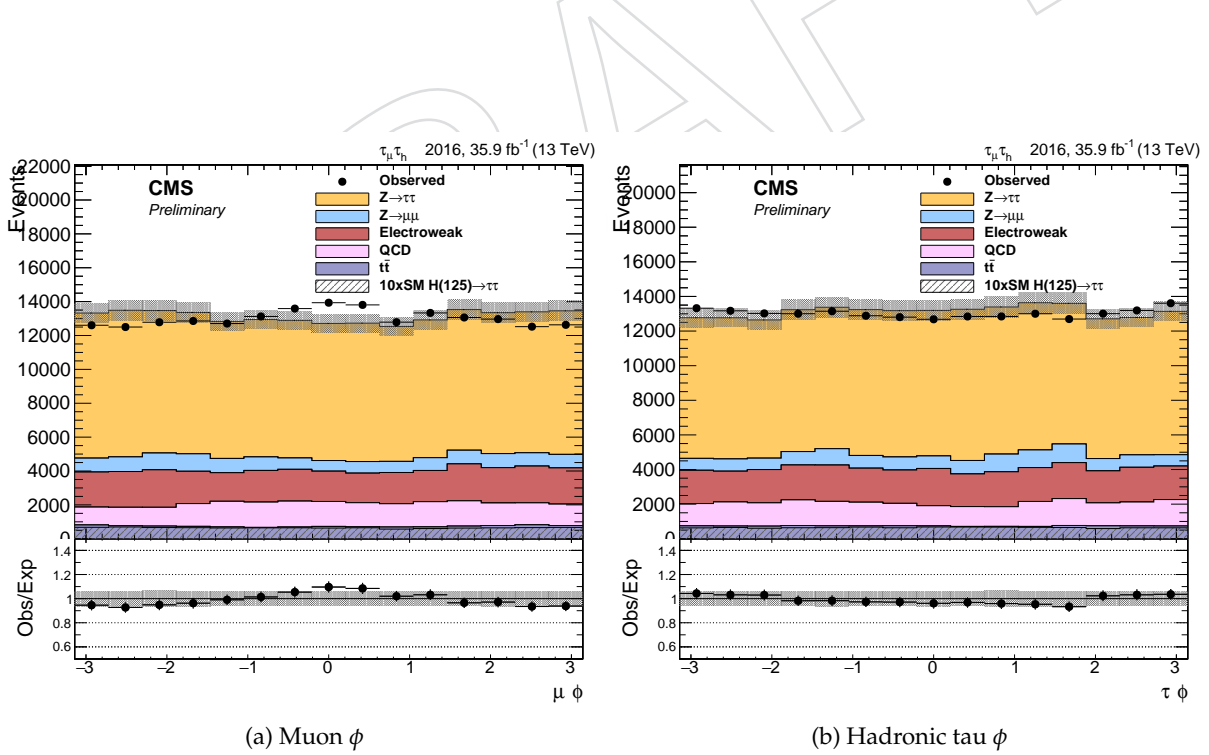


Figure 23: Prefit control distributions of the muon and tau ϕ angle in the $\mu\tau_h$ final state before dividing into categories.

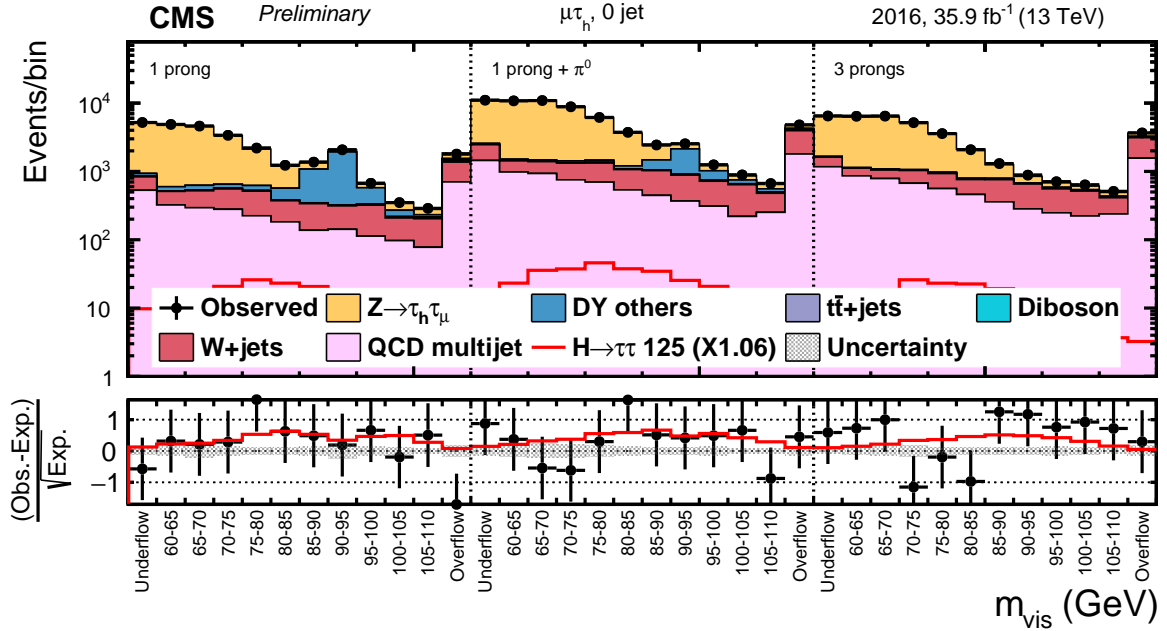


Figure 24: Prefit unrolled 2D distribution in the 0 jet category in the $\mu\tau_h$ final state.

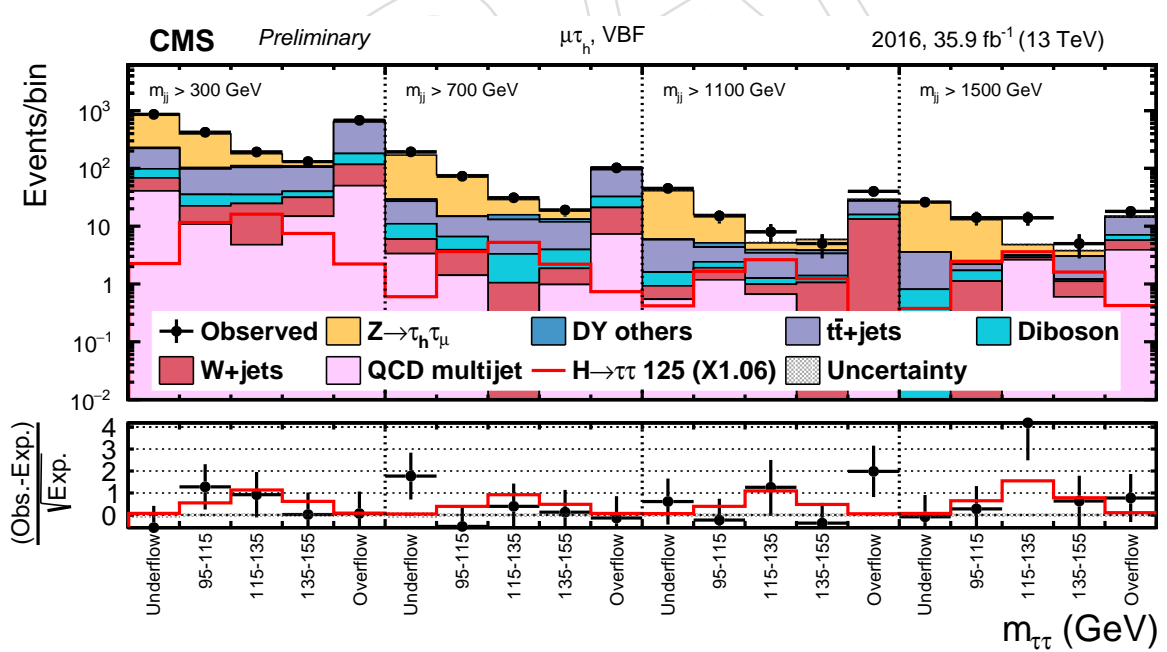


Figure 25: Prefit unrolled 2D distribution in the VBF category in the $\mu\tau_h$ final state.

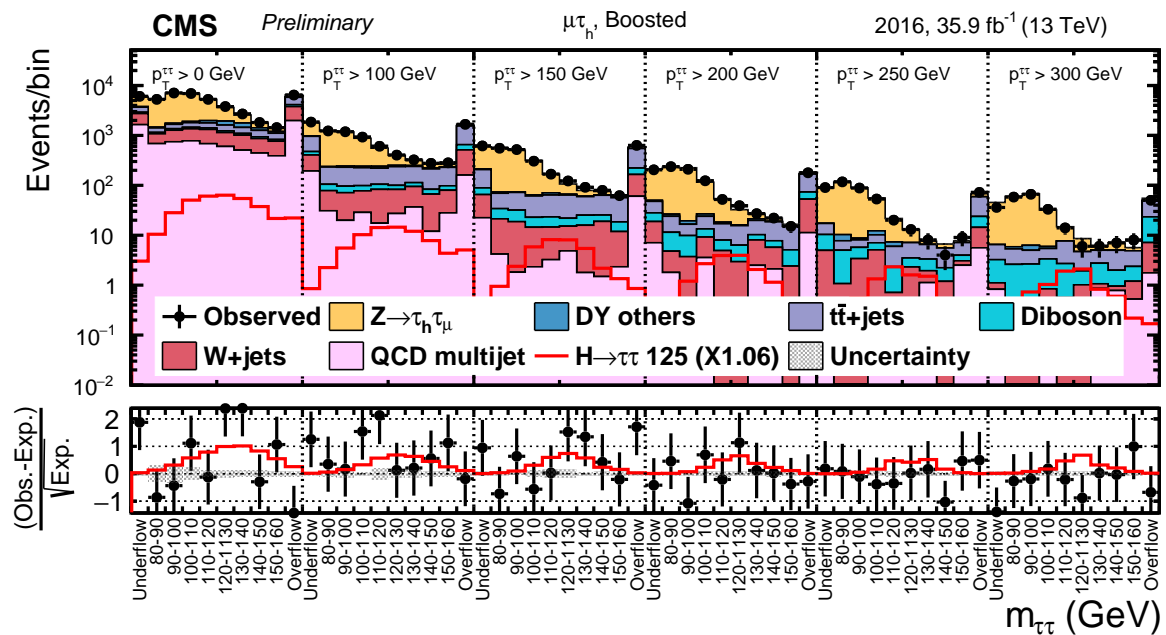


Figure 26: Prefit unrolled 2D distribution in the boosted category in the $\mu\tau_h$ final state.

- 639 Other prefit control plots for the $\mu\tau_h$ final state can be seen in Figs. ?? to 28; a good data/MC
 640 prefit agreement is observed everywhere.

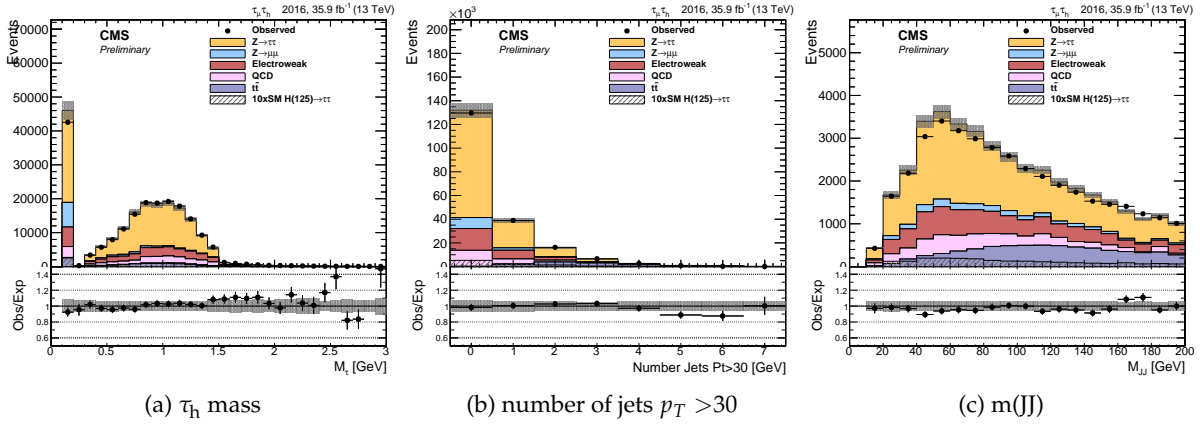


Figure 27: Prefit control plots of τ_h mass, number of jets with $p_T > 30$, and m_{JJ} in the $\mu\tau_h$ channel.

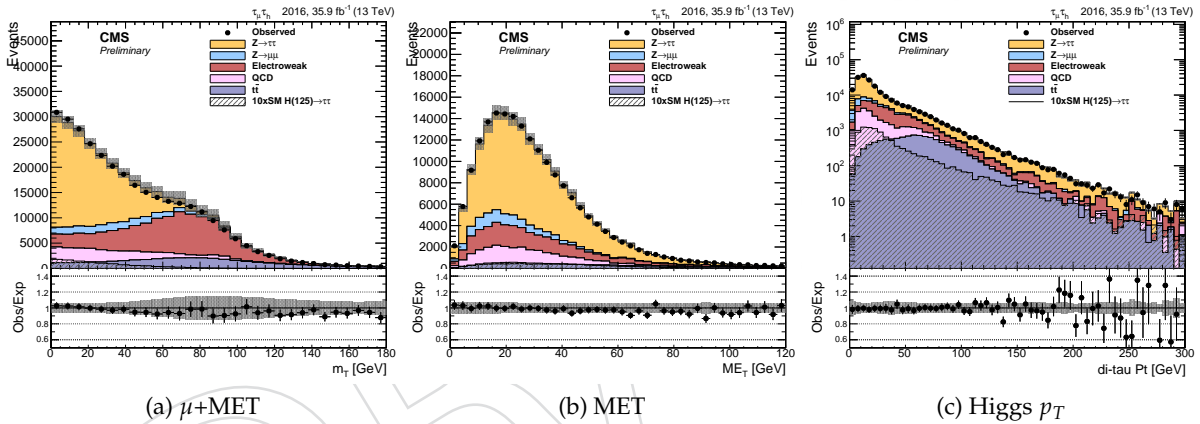


Figure 28: Prefit control plots of $\mu+\text{MET}$, MET, and Higgs p_T in the $\mu\tau_h$ channel.

641 7 The $e\tau_h$ final state

642 7.1 Trigger requirements

- 643 We consider events collected using the single electron HLT trigger, `HLT_Ele25_eta2p1_WPTight_Gsf`
 644 and we require the HLT electron and offline reconstructed electron to match within $\Delta R = 0.5$.
 645 Please see trigger section for more details.

646 7.2 Event selection

- 647 In order to select good $e\tau_h$ pairs, the following requirements on the single objects as well as on
 648 the pair must be satisfied.
- 649 In case more than one electron (hadronic tau) is found that pass the selection described above
 650 and in the following bullets, all possible pairs are considered and only the one with the most
 651 isolated electron (tau) is selected. If this is still not sufficient to select only one pair, the lepton
 652 (tau) with the highest p_T is preferred.

653 The electron is identified with the non-triggering MVA ID algorithm, using a working point
 654 that corresponds to an efficiency of 80%, and it must fulfil the following criteria:

- 655 • The longitudinal and transverse impact parameters of the electron track with respect
 656 to the primary vertex $d_z < 0.2$ cm and $d_{xy} < 0.045$ cm, respectively;
- 657 • the electron track has at most 1 missing inner hit ;
- 658 • the electron passes the conversion veto;
- 659 • offline $p_{T,e} > 26$ GeV, which is 1 GeV higher than the trigger threshold, and $|\eta_e| <$
 660 2.1, corresponding to the trigger acceptance. The offline p_T selection must be tighter
 661 than the trigger;
- 662 • the corrected relative isolation, measured in a cone with $\Delta R = 0.3$, should be smaller
 663 than 0.1.

664 The reconstructed hadronic tau candidate identification and selection is the same as the $\mu\tau_h$
 665 channel described in section 6.2, except for the anti-lepton discriminators: here the `againstElectronTight`
 666 is applied to strongly suppress Drell-Yan events, while the loose working point of the anti-
 667 muon discriminator `againstMuonLoose3` is chosen to reject other multi-leptonic backgrounds.

668 Moreover, events are vetoed that contain an additional electron identified with the cut-based
 669 ID (Spring15) algorithm, having $p_{T,e} > 15$ GeV, $d_z < 0.2$ and $d_{xy} < 0.45$ and a relative $\Delta\beta$ -
 670 corrected isolation smaller than 0.3. In the same way as for the $\mu\tau_h$ channel, events containing
 671 additional loosely identified electrons or muons passing the requirements listed in 6.2.2 are also
 672 vetoed.

673 7.3 Background methods

674 7.3.1 Drell-Yan

675 As described for the $\mu\tau_h$ final state in Section 6.3.1, data/MC scale factors are applied to the
 676 Drell-Yan background based on the data/MC agreement in a $Z \rightarrow \mu\mu$ enriched control region.
 677 The scale factors are applied inclusively for the 0jet and boosted categories, and per slice of m_{jj}
 678 in the VBF category.

679 The Drell Yan background is separated into 3 components based on the generator-level matching
 680 info of the hadronic tau

- 681 • If the τ_h candidate is matched to generator-level hadronically decaying tau, then it
 682 is classified as ZTT.
- 683 • If the τ_h candidate is matched to generator-level prompt lepton, then it is classified
 684 as ZL.
- 685 • All other cases are classified as a jet faking a τ_h and it is classified as ZJ.

686 7.3.2 $t\bar{t}$

687 The $t\bar{t}$ background is separated into two components based on the generator-level matching
 688 info of the hadronic tau

- 689 • If the τ_h candidate is matched to generator-level hadronically decaying tau, then it
 690 is classified as TTT.
- 691 • Otherwise it is classified as TTJ, as it most likely that a jet faked the reconstructed
 692 hadronic tau.

As explained for the $\mu\tau_h$ final state, the normalization is extracted from a control region enriched in $t\bar{t}$ events. This is detailed in Section 10.

7.3.3 W+jets

Please see section 6.3.3 for more details. The procedure follows the $\mu\tau_h$ channel exactly. The 0 jet and boosted high- m_T regions are included in the fit as control regions for the W+jets normalization, and the VBF signal region is linked to the boosted high m_T control region because the event topology is similar, and because the VBF high m_T control region would have a low W+jets purity.

7.3.4 QCD multijet

Please see section 6.3.4 for more details. The procedure follows the $\mu\tau_h$ channel exactly except for different QCD OS/SS ratios used in subtracting the QCD contribution. The plots used to extract the $e\tau_h$ OS-to-SS scale factors are shown in Fig. 29. Scale factors were extracted by using isolation-sorted $e\tau_h$ pairs or p_T -sorted $e\tau_h$ pairs; both methods produced similar results. Additionally the variation of the W+jets into the QCD yield was used as an extra systematic uncertainty. The errors on the QCD ratio reported by the Combine Tool contribute to the error. In addition, the statistical only errors if the scale factors are computed by-hand, are included in the error estimate of the OS/SS ratio. The results are shown in Tab. 10.

Control regions for the QCD obtained in the OS region with anti-isolated taus are added to the fit to adjust the QCD normalization dynamically.

Category	OS/SS QCD ratio	Error
0-jet	1.00	15 %
boosted	1.28	15 %
vbf	1.0	30 %

Table 10: QCD OS/SS ratios in the $e\tau_h$ final state.

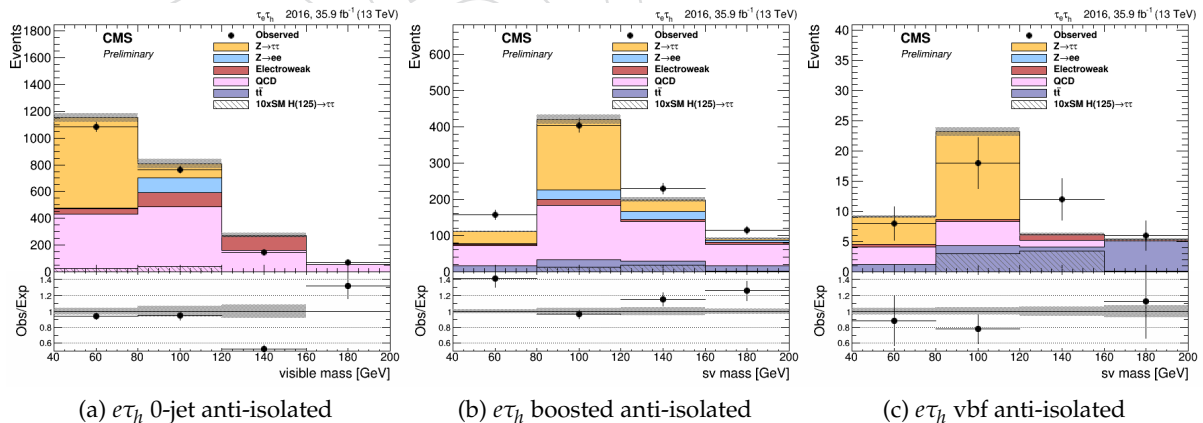


Figure 29: Distributions used to extract the $e\tau_h$ OS/SS QCD Factor.

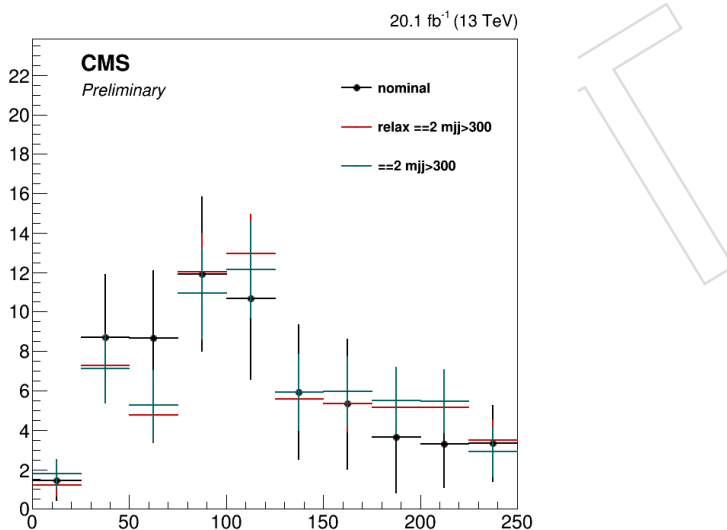
7.3.5 Relaxed selection

Please see section 6.3.5 for more information. The same criteria as in the $\mu\tau_h$ final state are used to extract the relaxed shapes for the W+jets and QCD backgrounds.

Category	Definition
0-jet	$p_{T,\tau_h} > 30 \text{ GeV}$ and $\text{njets}=0$ and $M_T < 50 \text{ GeV}$
Boosted	$p_{T,\tau_h} > 30 \text{ GeV}$ and ($\text{njets}==1$ or ($\text{njets}>=2$ and ($m_{jj} <= 300 \text{ GeV}$ or $p_T(H) < 50 \text{ GeV}$))) and $M_T < 50 \text{ GeV}$
VBF	$p_{T,\tau_h} > 30 \text{ GeV}$ and $\text{njets}>= 2$ and $p_T(H) > 50 \text{ GeV}$ and $m_{jj} > 300$ and $M_T < 50 \text{ GeV}$

Table 11: Definition of 2D categories in the $e\tau_h$ final state.

An example of alternative shapes for which KS tests have been performed is shown in Fig 30 for the $e\tau_h$ final state. In this figure, the nominal shape with full selection is compared to shapes with either relaxed lepton isolation (as chosen in the analysis), either relaxed conditions on the jets in the VBF category. Both shapes are found to be compatible with the nominal shape. The same bias tests as performed in the $\mu\tau_h$ final states are shown in Fig. 31 and 32: again, relaxing the shapes for the W+jets and QCD backgrounds does not bias the expected limits.

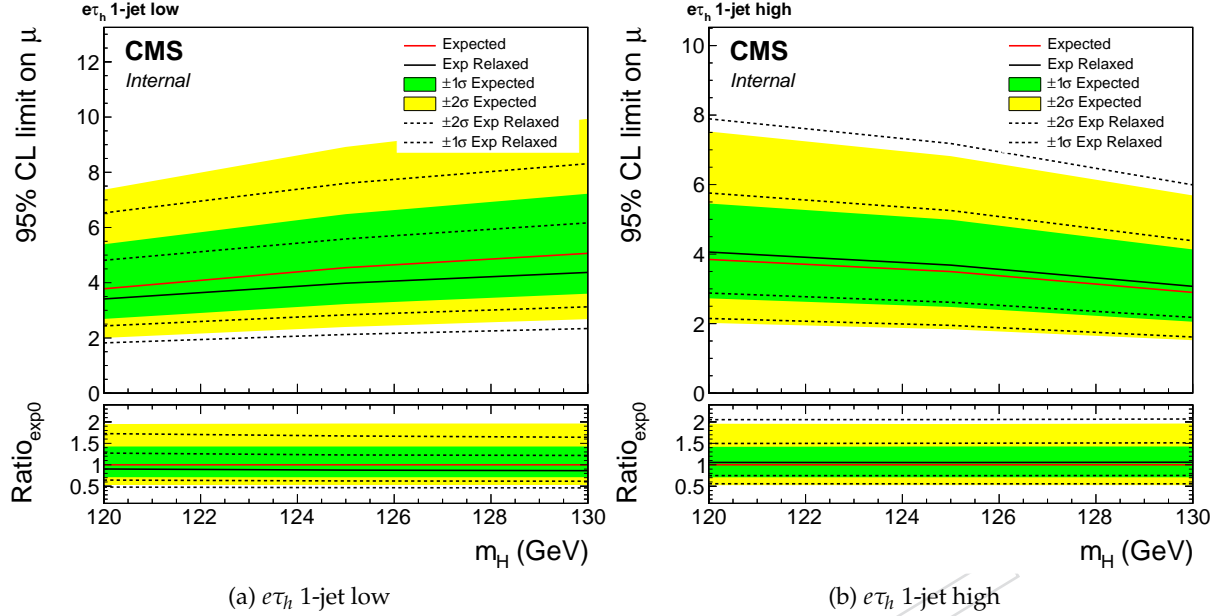
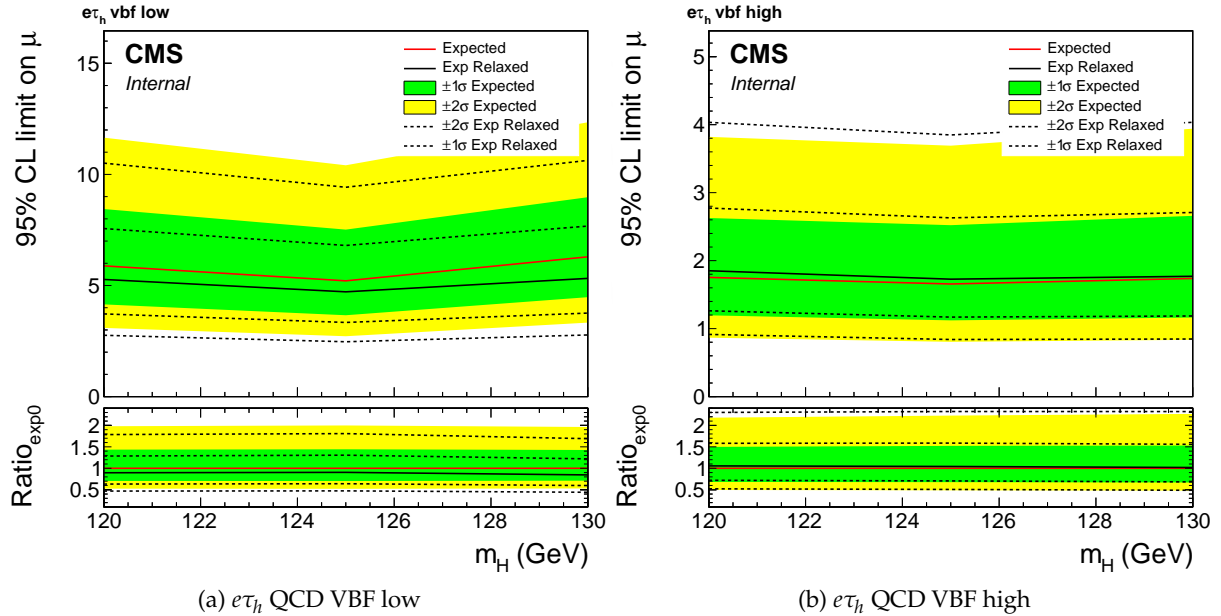
Figure 30: A shape comparison from the KS test study showing the $e\tau_h$ relaxed shape options where either the lepton isolation is relaxed (shown in orange) or the jet requirements are relaxed (shown in blue). The nominal selection is shown in black.

Relaxed selection bias tests were performed on the limits using the relaxed QCD multijet and W+jets shapes. The relaxed shapes do not affect the expected limits by more than about 10% in the low stat categories. These bias tests were performed on the 1-D categories.

7.4 Signal extraction

The final results are extracted via a 2D fit to distributions in three separate categories. These categories in the case of the $e\tau_h$ final state are defined in Tab. 11. The fitting variables are m_{vis} and the τ_h reconstructed decay mode in the 0-jet category, $m_{\tau\tau}$ and higgs p_T in the boosted category, and $m_{\tau\tau}$ and m_{jj} in the VBF category.

Although not used in the final results, 1D categories, close to those used for the Run-1 analysis, are defined and optimized to compare to the performance of the 2D signal extraction method. These optimized 1D categories are defined in Tab. 12.

Figure 31: $e\tau_h$ QCD bias test results for 1D categories.Figure 32: $e\tau_h$ Bias test result for 1D categories.

7.4.1 0-jet Signal Extraction

The 0-jet category is helpful for constraining systematics and targeting the gluon-gluon production. The distribution is unrolled in three bins of reconstructed decay τ decay mode: 1 prong, 1 prong + $\pi^0(s)$, 3 prongs. The main advantage of separating the reconstructed τ decay modes is that the Z background with a electron faking a τ_h is absent in the 3prong decay modes, whereas it is a large contribution in the 1 prong decay mode.

Category	Definition
0-jet low	$p_{T,\tau_h} > 20 \text{ GeV}$ and $P_{T,\tau} < 50$ and $\text{njets} == 0$ and $M_T < 50 \text{ GeV}$
0-jet high	$p_{T,\tau_h} > 50 \text{ GeV}$ and $\text{njets}=0$ and $M_T < 50 \text{ GeV}$
1-jet low	($\text{njets}=1$ or ($\text{njets}=2$ and $m_{jj} < 500 \text{ GeV}$)) and $P_{T,\tau} > 30 \text{ GeV}$ and ($p_{T\tau} < 40$ or $p_{Thiggs} < 140$) and $M_T < 50 \text{ GeV}$
1-jet high	$p_{T,\tau_h} > 40 \text{ GeV}$ and ($\text{njets} = 1$ or ($\text{njets}=2$ and $m_{jj} < 500 \text{ GeV}$))
vbf low	$p_{T,\tau_h} > 20 \text{ GeV}$ and $\text{njets}=2$ and $m_{jj} > 500$ and ($m_{jj} < 800$ or $p_{Thiggs} < 100$) and $M_T < 50 \text{ GeV}$
vbf high	$p_{T,\tau_h} > 20 \text{ GeV}$ and $\text{njets}=2$ and $m_{jj} > 800$ and $p_{Thiggs} < 100$ and $M_T < 50 \text{ GeV}$

Table 12: 1D categories for the $e\tau_h$ final state. They are not the default categories for the signal extraction.

738 The anti-lepton discriminators were measured in an inclusive selection for the TAU POG. How-
 739 ever we find a variation in the energy scale and the SF depending on the decay Mode of the
 740 reconstructed τ_h , this can be seen in figure 33. The simulation yields except for ZL(lepton fak-
 741 ing tau) are subtracted from the data. Data, and ZL are fit with gaussians to extroplate the m_{vis}
 742 shift and scale factor correction per decay mode. The results are in Table 13.

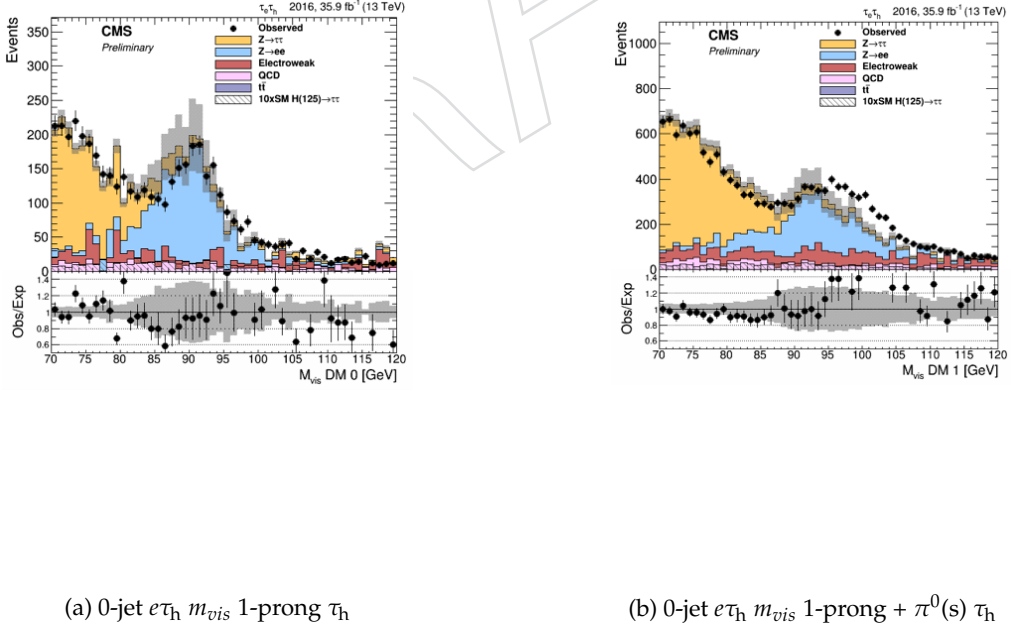


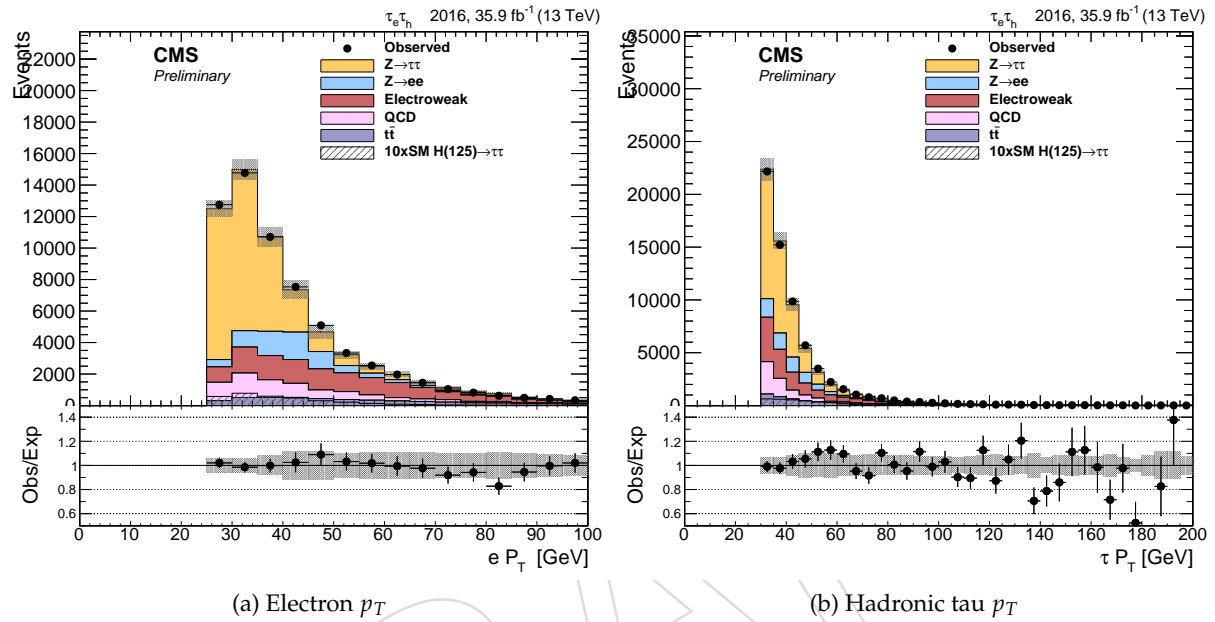
Figure 33: Prefit comparison of visible mass in the 0 jet category per τ_h decay mode in 1-prong and 1-prong + $\pi^0(s)$.

	1-Prong Decay Mode	1-Prong + $\pi^0(s)$	3-Prong
$\tau_h M_{vis}$ ES Correction	$1.7\% \pm 0.5\%$	$3\% \pm 0.5\%$	-
$e\tau_h e \rightarrow \tau_h$ fake rate correction	$0.98 (\pm 12\%)$	$1.49 (\pm 12\%)$	-

Table 13: 0-jet M_{vis} $e \rightarrow \tau_h$ fake rate corrections.

743 7.5 Control plots

744 Control plots of the lepton characteristics can be found in Figs. 34 to 36.

Figure 34: Prefit distributions of lepton p_T in the $e\tau_h$ final state before dividing into categories (inclusive selection).

745 Unrolled 2D distributions for the $e\tau_h$ final state are shown in Figs. 37-39. These are used to
746 extract the results.

747 Other control plots can be found in Figs. ??-41; good agreement between data and background
748 prediction is observed everywhere.

749 8 The $\tau_h \tau_h$ final state

750 8.1 Trigger requirements

751 The analysis currently applies run-dependant trigger requirements for data all samples and an
752 OR of two triggers for MC samples. There are a variety of thresholds available for the double
753 tau trigger throughout 2016 data taking. With a change in the isolation method used at the HLT
754 level, CMS was able to maintain a double tau trigger with a 35 GeV threshold through all of
755 2016. Please see Tab. 14 for details.

756 For selection of events in data: require `HLT_DoubleMediumIsoPFTau35_Trk1_eta2p1_Reg`
757 for Run BCDEFG and `HLT_DoubleMediumCombinedIsoPFTau35_Trk1_eta2p1_Reg` for Run
758 H. For MC events: require `HLT_DoubleMediumIsoPFTau35_Trk1_eta2p1_Reg` OR `HLT_DoubleMedium`
759 Each selected offline τ_h is required to match an HLT tau within $\Delta R < 0.5$, additionally, each cho-

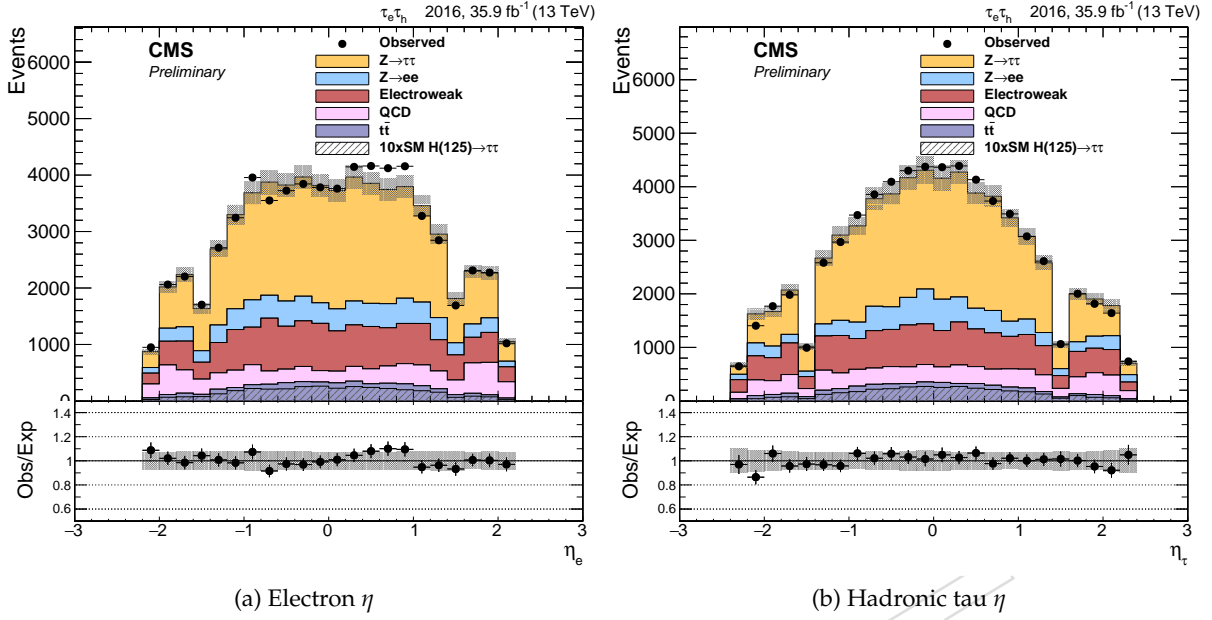


Figure 35: Prefit distributions of lepton pseudorapidities in the $e\tau_h$ final state before dividing into categories (inclusive selection).

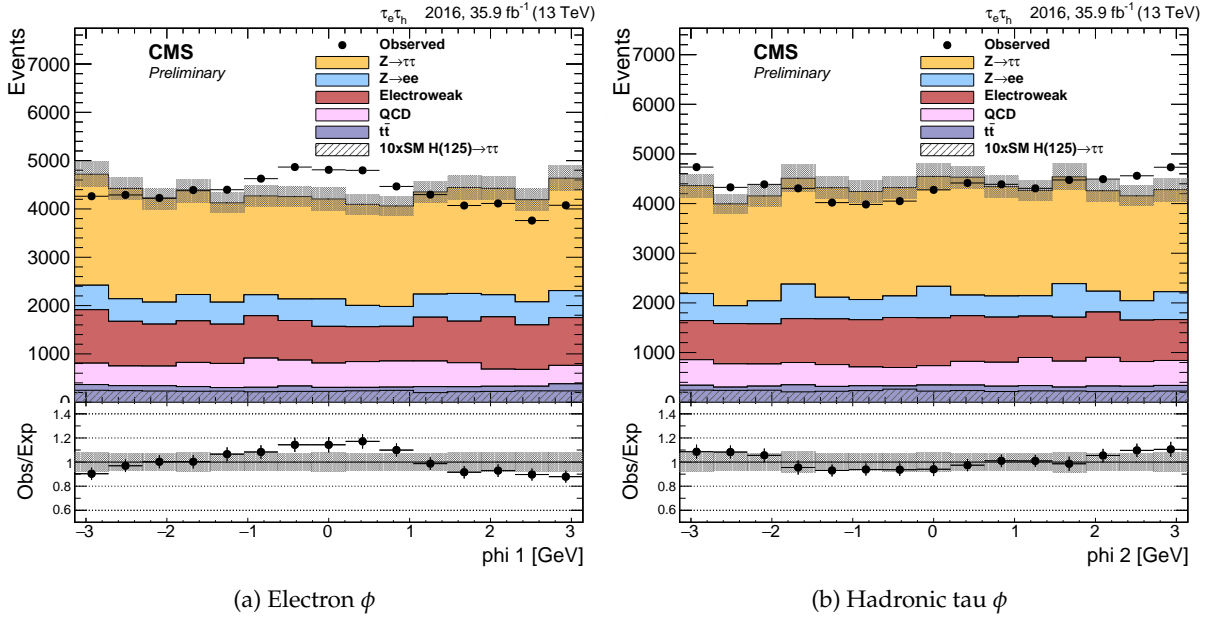


Figure 36: Prefit distributions of lepton ϕ angle in the $e\tau_h$ final state before dividing into categories (inclusive selection).

- 760 sen offline τ_h must match within $\Delta R < 0.5$ the last filter of the HLT path: `hltDoublePFTau35TrackPt1Medium`
 761 for `HLT_DoubleMediumIsoPFTau35_Trk1_eta2p1_Reg` and `hltDoublePFTau35TrackPt1MediumComb`
 762 for `HLT_DoubleMediumCombinedIsoPFTau35_Trk1_eta2p1_Reg`.
 763 Trigger efficiency based scale factors are applied to correct for differences in L1 and HLT trigger
 764 performance in data and MC. For details please refer to the section ??.

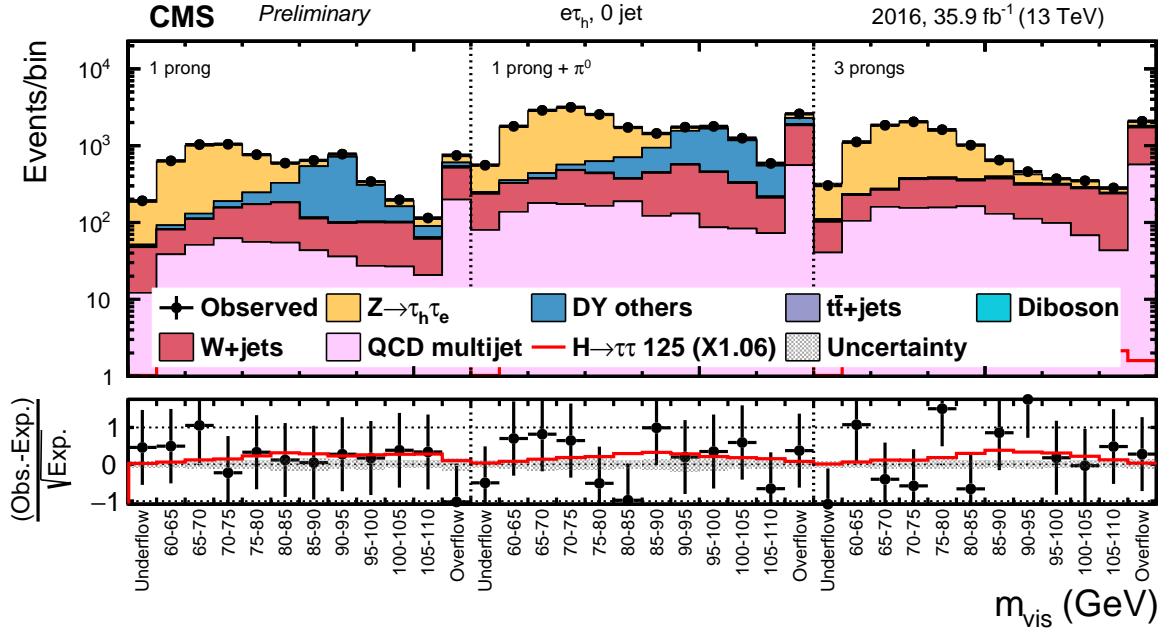


Figure 37: Prefit unrolled 2D distribution in the 0 jet category in the $e\tau_h$ final state.

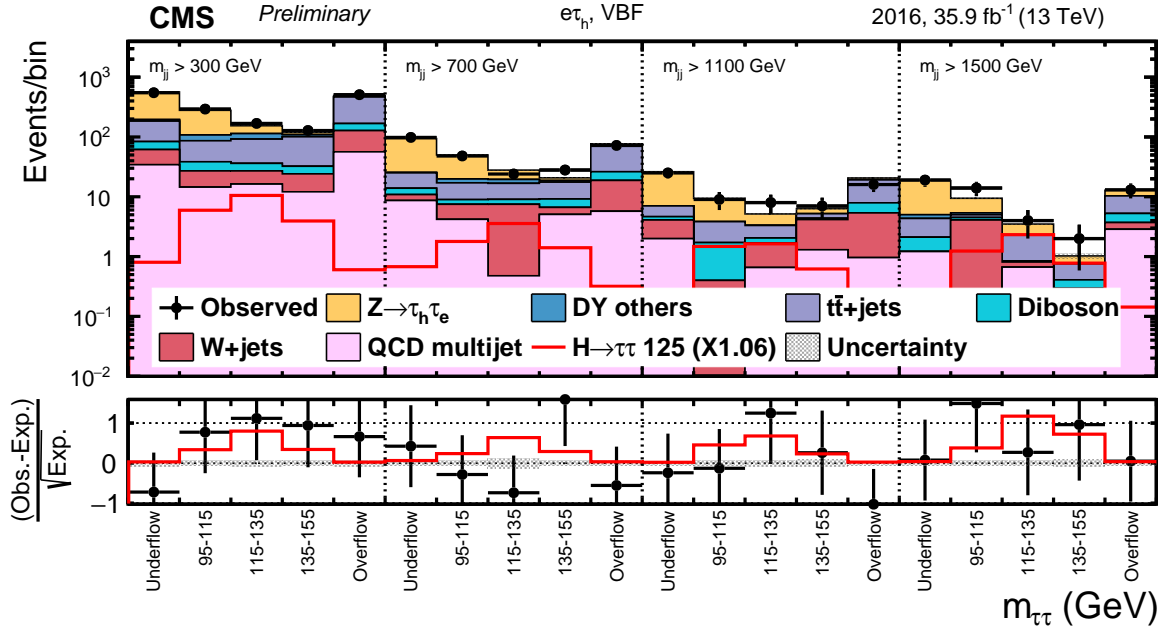


Figure 38: Prefit unrolled 2D distribution in the VBF category in the $e\tau_h$ final state.

8.2 Event selection

An event is selected if at least one $\tau_h \tau_h$ pair is found. In cases where more τ_h candidates are found in the event, the most isolated objects according to their MVA-based raw isolation value are taken. The τ_h -s must have opposite sign (OS) electric charges and must be separated by $\Delta R > 0.5$. Each τ_h should satisfy the following selection criteria:

- $p_T > 50$ (40) GeV for the leading (subleading) τ_h , and $|\eta| < 2.1$.

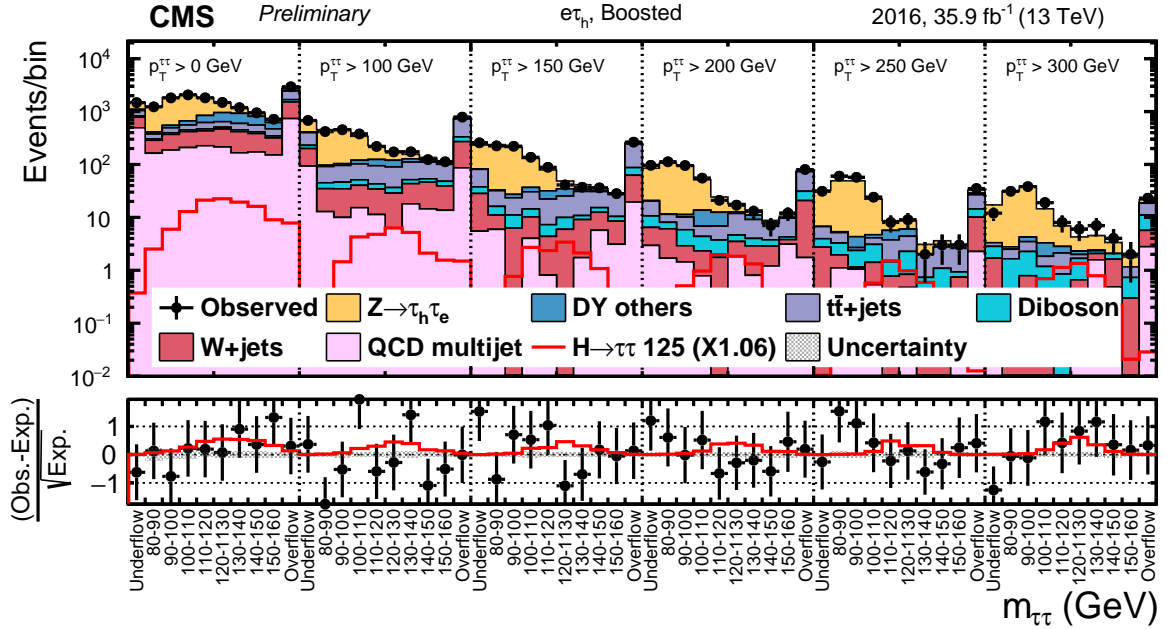


Figure 39: Prefit unrolled 2D distribution in the boosted category in the $e\tau_h$ final state.

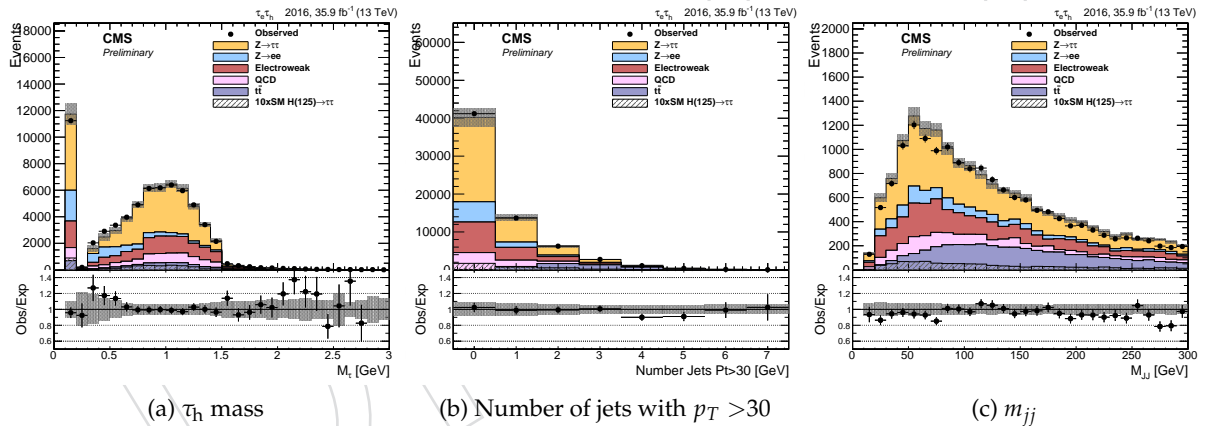


Figure 40: Prefit control plots of τ_h mass, number of jets with $p_T > 30$, and m_{jj} in the $e\tau_h$ channel.

HLT Trigger	Runs available	Notes
HLT_DoubleMediumIsoPFTau32.Trk1_etc2p1_Reg_v[2,3]	B,C,D,E	Not currently used in analysis
HLT_DoubleMediumIsoPFTau35.Trk1_etc2p1_Reg_v[3,4,5]	B,C,D,E,F,G	This is the required trigger for all MC events
HLT_DoubleMediumIsoPFTau40.Trk1_etc2p1_Reg_v[5,6,7]	B,C,D,E,F,G	100 percent overlap with PFTau35 at the moment
HLT_DoubleMediumCombinedIsoPFTau35.Trk1_etc2p1_Reg_v3	H	This is the single trigger used for Run H
HLT_DoubleMediumCombinedIsoPFTau40.Trk1_etc2p1_Reg_v2	H	100 percent overlap with PFTau35CmbIso at the moment

Table 14: List of relevant HLT triggers for the $\tau_h \tau_h$ final state.

- The τ_h must be identified as 1- or 3-prong according to discriminator byDecayModeFinding;
- $dZ < 0.2$ (defined by packedLeadTauCand->dz () with respect to the PV);
- againstElectronVLooseMVA6 > 0.5 ;
- againstMuonLoose3 > 0.5 ;

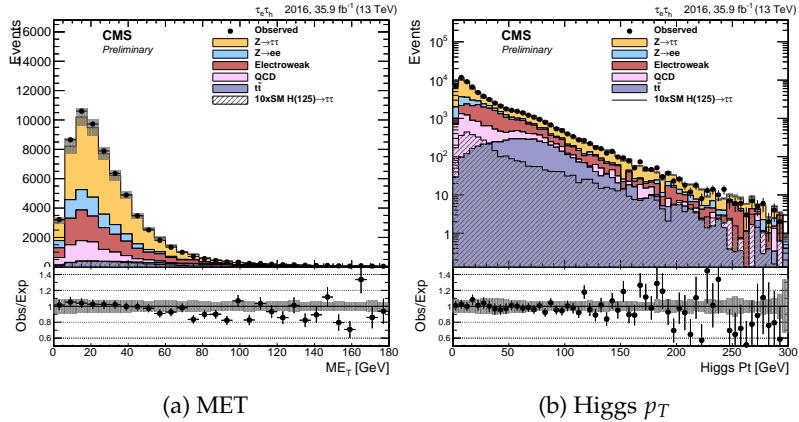


Figure 41: Control plots of MET, and p_T of the visible decay products in the $e\tau_h$ channel.

- The tau must satisfy the tight working point of the MVA-based isolation trained for Run II analysis by Tau POG: `byTightIsolationMVArun2v1DBoldDMwLT > 0.5`.

If an electron or muon, passing a loose selection criteria, is found in the event then the event is rejected. For later reference, the selected taus are ordered by their p_T , and the highest p_T and subleading taus are called $\tau_{h,1}$ and $\tau_{h,2}$, respectively. The leading tau must satisfy the requirement $p_{T,\tau_{h,1}} > 50$ GeV, which is tighter than what the trigger would allow (40 GeV offline for both τ_h). The threshold is a result of optimization studies.

8.3 Signal extraction

Three event categories are considered: 0-jet, boosted, and VBF, defined in table 15. For 0-jet category, a 1D distribution of di-tau mass (SVfit) is used for signal extraction, while, we unroll 2D distributions of reconstructed di-tau mass in `Higgs_Pt` for the boosted category and `di-jet Mass` for the VBF category. Additionally, we use the same approach as used in the Run I analysis as a cross check. These 1D categories are heavily based off of Run I categories with the addition of 0-jet and vbf_low categories, as given in Tab. 16.

Category	Definition
0-jet	<code>njets==0</code>
boosted	<code>njets==1 or not (njets>=2 and Higgs_Pt>100 and abs(jdeta)>2.5)</code>
VBF	<code>(njets>=2 and Higgs_Pt>100 and abs(jdeta)>2.5)</code>

Table 15: List of 2D signal extraction categories with their definitions.

The specific binning used to unroll the 2D histograms is critical. Following are the choices made for this channel:

- 0 jet: di-tau Mass binned as 0-300 in 10 GeV steps
- boosted: unroll in `Higgs_Pt` using `Higgs_Pt` bins of [0: 100: 170: 300: Inf] with di-tau Mass binning [0, 40, 60, 70, 80, 90, 100, 110, 120, 130, 150, 200, 250]
- VBF: unroll in `di-jet Mass` using `di-jet Mass` bins of [0: 300: 500: 800: Inf] with di-tau Mass binning [0, 40, 60, 70, 80, 90, 100, 110, 120, 130, 150, 200, 250]

Category	Definition
0-jet	$n_{\text{jets}} == 0$
1-jet low	$(\text{Higgs}_\tau.Pt > 100 \text{ and } \text{Higgs}_\tau.Pt < 170) * (\text{njets} == 1 \text{ or } (\text{njets} >= 2 \text{ and not } (\text{di-jet Mass} > 300 \text{ and } \text{abs(jdeta)} > 2.5 \text{ and } \text{njetgap30} < 1)))$
1-jet high	$(\text{Higgs}_\tau.Pt > 170) * (\text{njets} == 1 \text{ or } (\text{njets} >= 2 \text{ and not } (\text{di-jet Mass} > 300 \text{ and } \text{abs(jdeta)} > 2.5 \text{ and } \text{njetgap30} < 1)))$
vbf low	$(\text{njets} >= 2 \text{ and } \text{abs(jdeta)} > 2.5 \text{ and } \text{njetgap30} < 1) * ((\text{Higgs}_\tau.Pt < 100 \text{ and } \text{di-jet Mass} > 300) \text{ or } (\text{Higgs}_\tau.Pt > 100 \text{ and } \text{di-jet Mass} > 300 \text{ and } \text{di-jet Mass} < 500))$
vbf high	$(\text{njets} >= 2 \text{ and } \text{Higgs}_\tau.Pt > 100 \text{ and } \text{di-jet Mass} > 500 \text{ and } \text{abs(jdeta)} > 2.5 \text{ and } \text{njetgap30} < 1)$

Table 16: List of 1D signal extraction categories with their definitions.

796 8.4 Background methods

797 8.4.1 QCD estimation

798 The method for QCD estimation in the $\tau_h \tau_h$ channel differs from that used in the other channels.
 799 Instead of using a same-sign region to estimate the yield and shape, an opposite-sign sideband
 800 with inverted isolation is used. This is done because there is a significant difference in QCD
 801 shape between opposite-sign and same-sign regions in the $\tau_h \tau_h$ channel.

802 The QCD background shape and yield are estimated using p_T ordered taus and a combination
 803 of three sideband regions. In each sideband, the QCD contribution is estimated as data with
 804 all non-signal MC backgrounds subtracted. The sideband region that defines the shape and
 805 initial yield is defined by inverting the isolation requirement on one of the taus. To increase
 806 statistical yield, the isolation of the other tau is relaxed. All other selection criteria remain
 807 identical to the associated signal region (this includes also opposite sign requirement for two
 808 taus). Estimated QCD yield in this region is scaled by a loose-to-tight isolation scale factor. This
 809 factor is calculated in a region selected similarly to the previously mentioned sideband region,
 810 but instead of OS requirement, the taus must have the same sign electric charges. The specific
 811 isolation WP cuts used for these three regions are detailed in Tab. 17 and are kept the same for
 812 all categories both 2D and 1D. The final estimated yield for the QCD background is calculated
 813 according to Equation 14.

$$\text{QCD Yield} = \text{OS Loose Iso. Yield} \times \left(\frac{\text{SS Signal-like Iso. Yield}}{\text{SS Loose Iso. Yield}} \right) \quad (14)$$

Category	Isolation cuts
opposite-sign signal region	$\tau_{h,1} == \text{Tight}$ and $\tau_{h,2} == \text{Tight}$
opposite-sign loose	$(\tau_{h,1} == \text{Medium} \text{ and } \tau_{h,2} != \text{Tight} \text{ and } \tau_{h,2} == \text{Loose}) \text{ or } (\tau_{h,2} == \text{Medium} \text{ and } \tau_{h,1} != \text{Tight} \text{ and } \tau_{h,1} == \text{Loose})$
same-sign signal-like	$\tau_{h,1} == \text{Tight}$ and $\tau_{h,2} == \text{Tight}$
same-sign loose	$(\tau_{h,1} == \text{Medium} \text{ and } \tau_{h,2} != \text{Tight} \text{ and } \tau_{h,2} == \text{Loose}) \text{ or } (\tau_{h,2} == \text{Medium} \text{ and } \tau_{h,1} != \text{Tight} \text{ and } \tau_{h,1} == \text{Loose})$

Table 17: Sideband regions used for $\tau_h \tau_h$ QCD estimation

814 There are three dominant uncertainties in the QCD estimation process. There are uncertainties
 815 associated with 1) the estimated shape, 2) the yield provided by the three sideband regions,
 816 and 3) uncertainty on the QCD estimation method itself.

817 1) Shape uncertainties: The chosen isolation cut values were selected based on a balance be-
 818 tween statistical yield and shape compatibility. In the context of the MSSM $\Phi \rightarrow \tau\tau$ analysis

with 2015 data [35] KS tests were used to verify compatibility between estimated QCD shapes for 13 TeV data. The KS tests verified the statistical compatibility between shapes of varying isolation within the same charge configuration; loose same-sign shapes are compatible with other same-sign shapes and likewise for opposite-sign. These shape comparisons extended through the range of MVA Isolation discriminator WPs applied to the subleading tau while the leading tau was held at fixed, yet relaxed isolation WP. Various relaxed isolation WPs were assessed for the leading tau as well. Additionally, the reasonably wide di-tau mass variable binning chosen for the high sensitivity $\tau_h \tau_h$ categories ensures that any shape differences between the loosened isolation control region and the signal region will be minimal.

2a) Yield from opposite-sign sideband region: The different terms in Equation 14 all have uncertainties associated with them. A OS Loose Iso. Yield control region is incorporated into the final simultaneous fit to account for statistical and systematic uncertainties in this region. The control regions span the same `svFit Mass` range as their associated signal region for a given category. To simplify computation, the `svFit Mass` range is collapsed into a single bin for each control region. The simultaneous fit allows us to incorporate the effects of normalization and shape systematics, converted to asymmetric up and down normalization uncertainties, into the initial best estimate of QCD yield. No signal is included in this region. All background uncertainties are included such as JES, TES, and Drell-Yan reweighting.

Adding the simultaneous fit is important because the relative size of the non-QCD background which is subtracted while estimating QCD, $QCD_{yield} = (Data - MC)$ is sizable in the Boosted and VBF categories, see Fig. 42. An uncertainty of specific concern here is the LO Drell-Yan reweight which has an up and down shift of +/- 15% in the Boosted and VBF categories which can affect the QCD normalization in a non-negligible way.

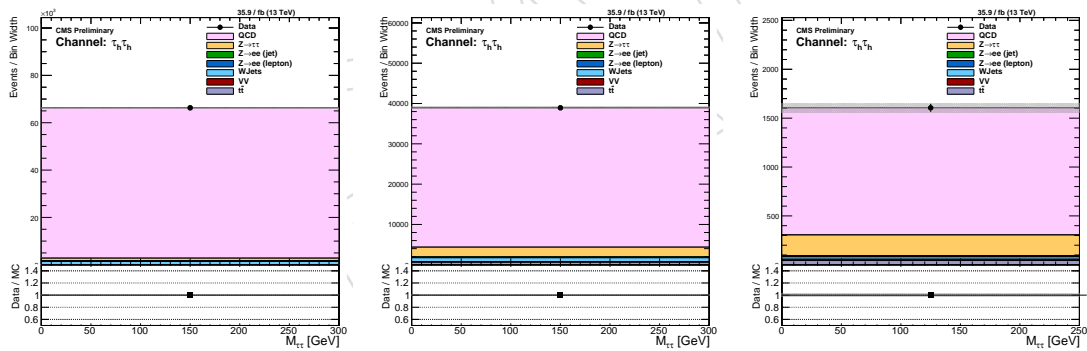


Figure 42: Plots showing the single bin based QCD normalization control regions for each category. The ratio plot agrees by construction. Only statistical uncertainty is shown. Left) 0-jet Middle) Boosted Right) VBF.

2b) Yields from same-sign sideband regions: The statistical uncertainty on the yield of the same-sign sideband regions is based on the estimated $QCD_{yield} = (Data - MC)$. The uncertainty is attributed as $\sqrt{N_{QCD_{yield}}}$. This is valid because the same-sign sideband regions are dominated by QCD, thus a \sqrt{N} uncertainty applied to the data which defines the QCD is the dominant uncertainty compared to uncertainties associated with the subtracted MC. A \sqrt{N} uncertainty is applied to the two same-sign terms from Equation 14, SS Signal-like Iso. Yield, and SS Loose Iso. Yield. These uncertainties are propagated to the final estimated QCD_{yield} . These uncertainties can be seen in Table 18.

3) Uncertainty on QCD estimation method: The method presented here for estimating QCD is

Category	QCD yield uncertainty
0-jet (2D)	1.0%
VBF (2D)	9.8%
Boosted (2D)	1.4%

Table 18: The sideband QCD_{yield} based uncertainties associated with each category are provided

likely not 100% unbiased. For that reason closure tests were conducted in a fully unblinded region to determine the degree to which this method is biased. The closure test used less isolated regions than what is used for signal extraction. One can visualize a 2-dimension plane of tau isolation working points. The selections listed in Table 17 can be viewed in this 2-dimension plane, see Figure 43.

Using the closure isolation sideband regions depicted, we use the same ABCD method to estimate the OS yield in the Tighter Validation Region region based on yields in the Looser Validation Region. Again, the Looser region is kept as close as possible to the Tight/Signal Region in Isolation WPs. We take the non-closure between the estimated yield in the OS Tighter region and the "measured" yield from $QCD_{yield} = (Data - MC)$ as the systematic uncertainty on the QCD estimation method. Table 19 shows the results of this test for the 2D categorization.

For the 2D categories, there is decent statistical agreement between the closure value, $QCD_{yield,Estimate} / QCD_{yield,"Actual"}$, and unity when uncertainties are taken into account for VBF and Boosted categories, while 0-jet shows some disagreement. This shows there is likely some yield bias in QCD Estimation Method. We account for what bias there may be, by application of the uncertainties in Table 19.

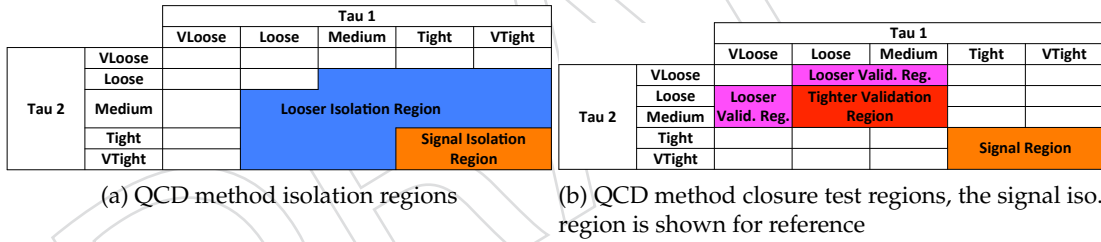


Figure 43: Illustration of regions for QCD background estimation (left) and for closure test (right).

Category	$QCD_{yield,Estimate} / QCD_{yield,"Actual"}$	Uncertainty on closure	QCD Method Syst. Uncert.
0-jet (2D)	0.98	0.94%	2.5%
VBF (2D)	0.95	7.4%	12%
Boosted (2D)	0.99	1.3%	2.3%

Table 19: Non-closure results are presented above. For each category $QCD_{yield,Estimate}$ is compared against $QCD_{yield,"Actual"}$. The closure is measured as $Estimate / "Actual"$. The Uncertainty on the closure value combines all four closure regions \sqrt{N} based uncertainty by adding them in quadrature. The QCD Method systematic uncertainty takes the deviation from unity for $Estimate / "Actual"$ as a percent and adds it with the uncertainty on closure.

The QCD yield uncertainty and QCD method uncertainty can be combined in quadrature

868 to provide a QCD normalization uncertainty for inclusion in the data cards along with the
 869 OS Loose Iso. Yield control region. This combination is shown in Table 20.

Category	QCD yield unc.	QCD method syst. unc.	QCD estimate unc.
0-jet (2D)	1.0%	2.5%	2.7%
VBF (2D)	9.8%	12%	15%
Boosted (2D)	1.4%	2.3%	2.7%

Table 20: QCD yield uncertainty from 18 and 19 are added in quadrature to calculate the QCD estimate uncertainty (sans opposite-sign control region).

870 Further study shows there is essentially a flat distribution in estimated opposite-sign / same-
 871 sign QCD yields when binned in the MVA Tau Isolation WP of the looser of the two selected
 872 taus. This can be seen in Figure 44. The events displayed here all pass the 2D Boosted category
 873 definition. They are split into 4 groups for visualization: an all inclusive group (black line),
 874 events passing ($0 \text{ GeV} < \text{Higgs.Pt} < 100 \text{ GeV}$) (red line), events passing ($100 \text{ GeV} < \text{Higgs.Pt}$
 875 $< 170 \text{ GeV}$) (green line) and events passing ($\text{Higgs.Pt} > 170 \text{ GeV}$) (blue line). An additional cut
 876 of $m_{\ell\ell} > 100$ is include in both the OS and SS regions to select high QCD purity, Drell-Yan free
 877 regions. This additional cut nearly eliminate the contribution of Drell-Yan in the opposite-sign
 878 regions.

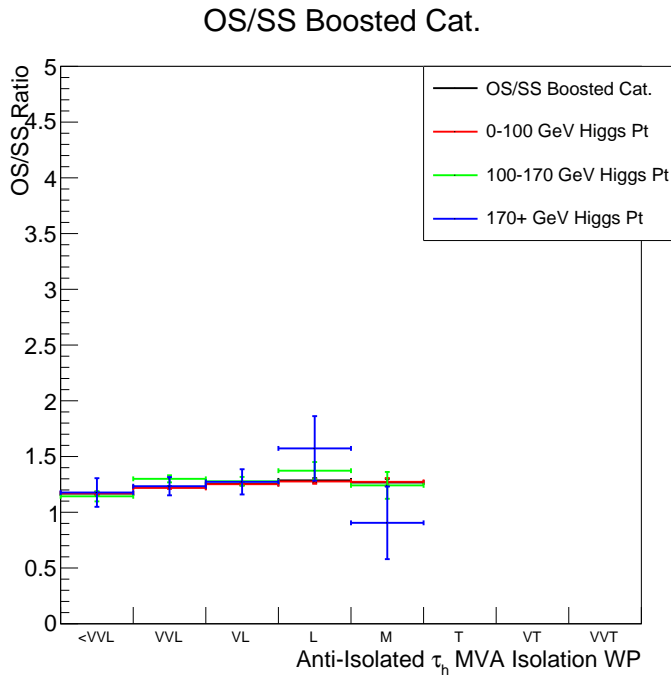


Figure 44: The events displayed here all pass the 2D Boosted category definition. Events are binned based on the MVA Tau Isolation WP of the looser of the two selected taus. Data and background events are split into 4 groups prior to the QCD estimation process to aid in visualization: an all inclusive group (black line), events passing ($0 \text{ GeV} < \text{Higgs.Pt} < 100 \text{ GeV}$) (red line), events passing ($100 \text{ GeV} < \text{Higgs.Pt} < 170 \text{ GeV}$) (green line) and events passing ($\text{Higgs.Pt} > 170 \text{ GeV}$) (blue line).

879 The main characteristic to note in Figure 44 is the agreement in the opposite-sign / same-sign
 880 ratio for each MVA Tau Isolation WP between the various Higgs.Pt boost regions. This sta-
 881 bility shows we will not have to worry about applying slice-by-slice correction factors to the

estimated QCD yield based on `Higgs_Pt`. Another characteristic to note from the plot is that the OS/SS QCD ratio moving from looser MVA Tau Isolation WPs towards tighter WPs is essentially flat. Any minor trends would be accounted for in the QCD estimation method uncertainty from the uncertainty attributed to the non-closure of the closure tests.

8.4.2 Drell-Yan background estimation

As described for the $\mu\tau_h$ final state in Section 6.3.1, data/MC scale factors are applied to the Drell-Yan background based on the data/MC agreement in a $Z \rightarrow \mu\mu$ enriched control region. The scale factors are applied inclusively for the 0-jet and boosted categories, and per slice of m_{jj} in the VBF category. The scale factors differ from the other final states in the VBF category because the selection is different. The corresponding distributions are shown in Fig. 45.

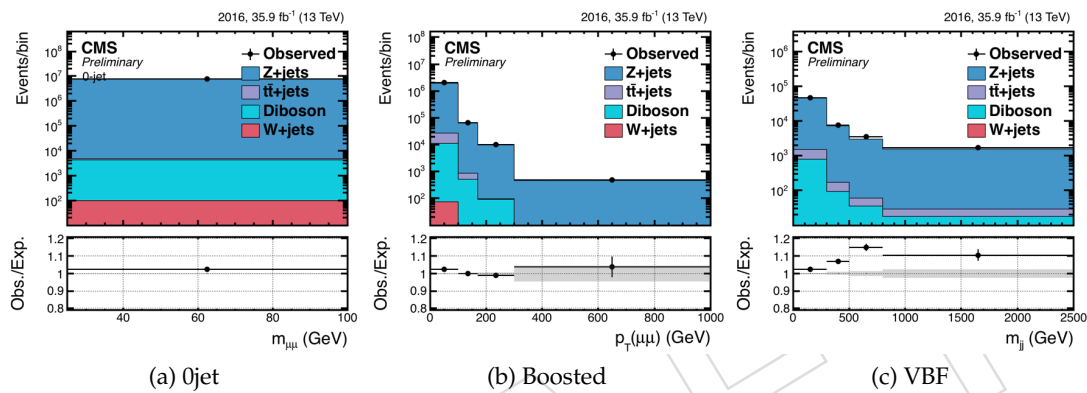


Figure 45: Data/MC comparison in a $Z \rightarrow \mu\mu$ control region, for the categories defined as in the case of the $\tau_h\tau_h$ final state. The data/MC ratio are applied as scale factors for the $Z \rightarrow \tau\tau$ background in the signal region.

8.4.3 $t\bar{t}$

The $t\bar{t}$ background is separated into two components based on generator-level matching info for the τ_h -s

- If both τ_h are matched to generator-level hadronically decaying taus, then an event is classified as TTT.
- Otherwise it is classified as TTJ, as it most likely that a jet faked the reconstructed hadronic tau.

As explained for the $\mu\tau_h$ final state, the normalization is extracted from a control region enriched in $t\bar{t}$ events. This is detailed in Section 10.

8.4.4 Diboson

The Diboson background is separated into two components based on generator-level matching info for the τ_h -s

- If both τ_h are matched to generator-level hadronically decaying taus, then an event is classified as VVT.
- Otherwise it is classified as VVJ, as it most likely that a jet faked the reconstructed hadronic tau.

Diboson processes are taken from their Monte Carlo predictions. Data / MC corrections are applied similar to all other categories.

8.4.5 Other backgrounds estimation

Contribution including those from the W+Jets and single-top background processes are taken from their Monte Carlo predictions. Data / MC corrections are applied similar to all other categories. W+jets has no data-driven estimation component.

8.5 Control plots

All plots currently included in this section are pre-fit.

8.5.1 Categorization variables

The Figs. 46, 47, 48, 49, and 50 show distributions for the primary variables of concern for the signal extraction categorization process: p_{T,τ_h} , η_{τ_h} , number of jets with $p_T > 30$ GeV, di-jet invariant mass, and p_T of Higgs candidate. Tau decay mode is also presented.

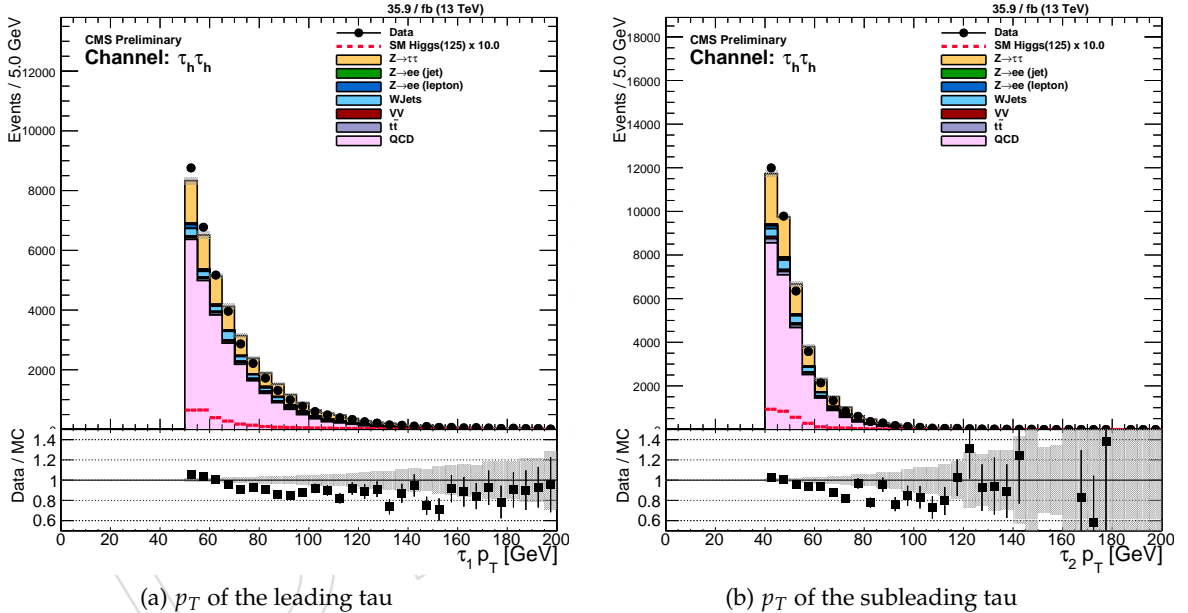


Figure 46: Prefit distribution showing statistical uncertainty only for the p_T distribution of the leading (left) and subleading (right) taus with the inclusive selection in the $\tau_h \tau_h$ final state.

8.5.2 Reconstructed Di-Tau Mass

In Fig. 51 the SVfit distribution before unrolling is shown. The Figs. 52 and 53 show the SVfit distributions in boosted and vbf categories after unrolling. The plots are blinded where we expect to see signal. In the 2D plots this corresponds to blinding and bins with significance > 0.1 , and in 1D this corresponds to blinding in the 100 - 150 GeV mass window for sensitive categories. The shown signal is the sum of ggH125 and qqH125 signal samples and has been multiplied by 10x except in the 1D vbf high category where it is multiplied by a factor of 2.5x.

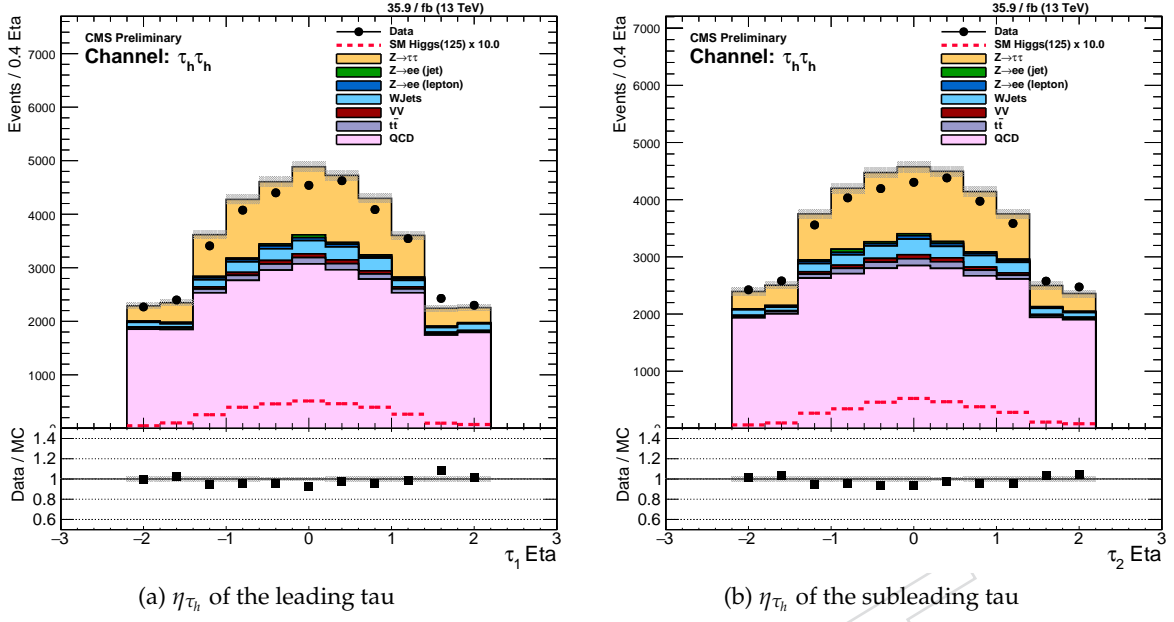


Figure 47: Prefit distribution showing statistical uncertainty only for the η distribution of the leading (left) and sub-leading (right) taus with the inclusive selection in the $\tau_h \tau_h$ final state.

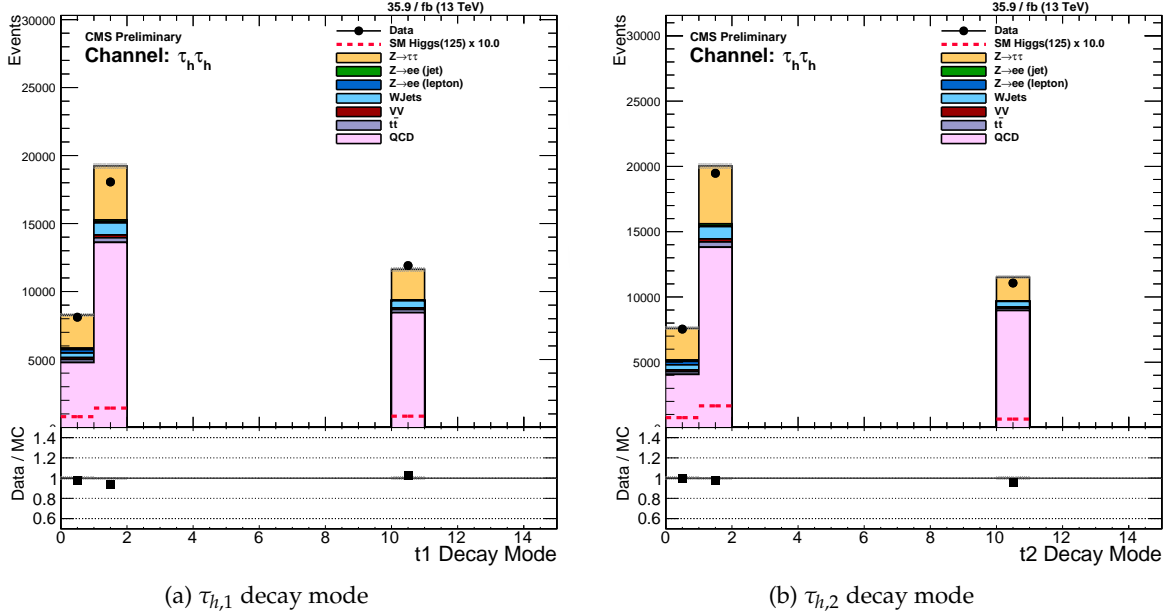


Figure 48: Prefit distribution showing statistical uncertainty only for the decay mode of the leading (left) and sub-leading (right) taus with the inclusive selection in the $\tau_h \tau_h$ final state.

928 Overall there is a good data-background agreement. Figs. ?? and ?? show the agreement for
 929 variations of the reweighting of the Drell-Yan background according to the generated mass and
 930 p_T , as detailed in section 4.6.

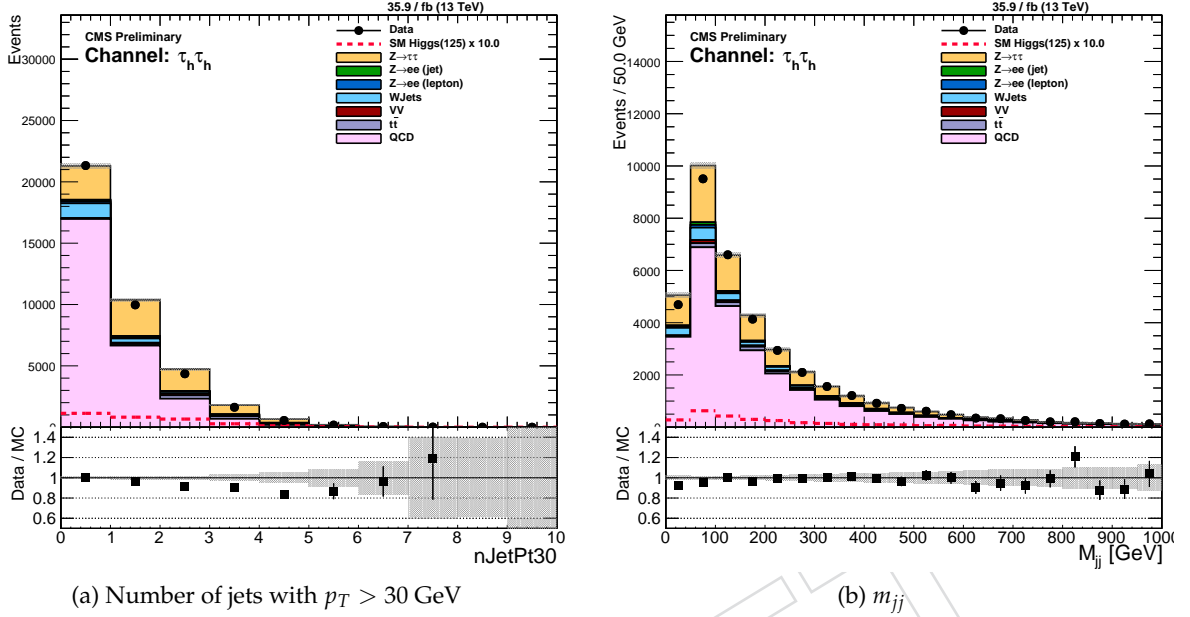


Figure 49: Prefit distribution showing statistical uncertainty only for the number of jets (left) and di-jet invariant mass (right) distributions with the inclusive selection in the $\tau_h \tau_h$ final state.

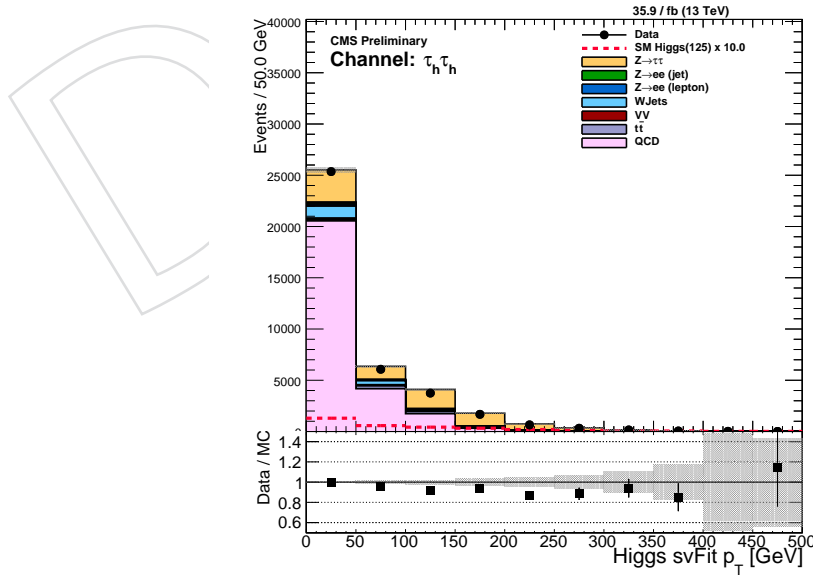
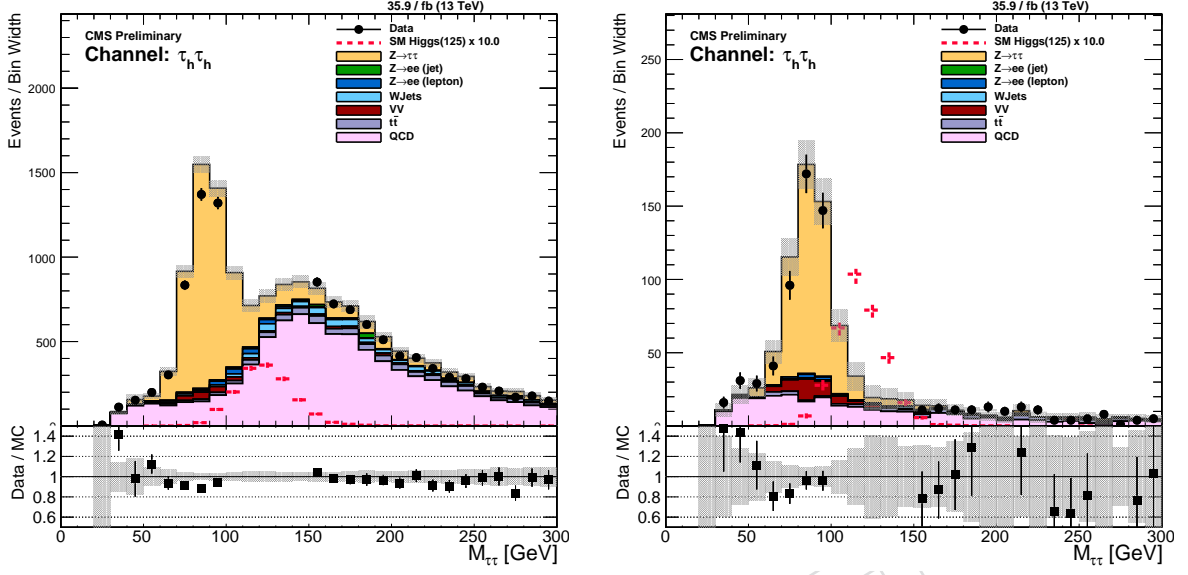


Figure 50: Prefit Higgs p_T distribution with the inclusive selection in the $\tau_h \tau_h$ final state.



(a) Pre-fit, statistical uncertainty only, $\tau_h \tau_h$ 2D boosted category no-unroll
(b) Pre-fit, statistical uncertainty only, $\tau_h \tau_h$ 2D VBF category no-unroll

Figure 51: The SVfit distribution before unrolling.

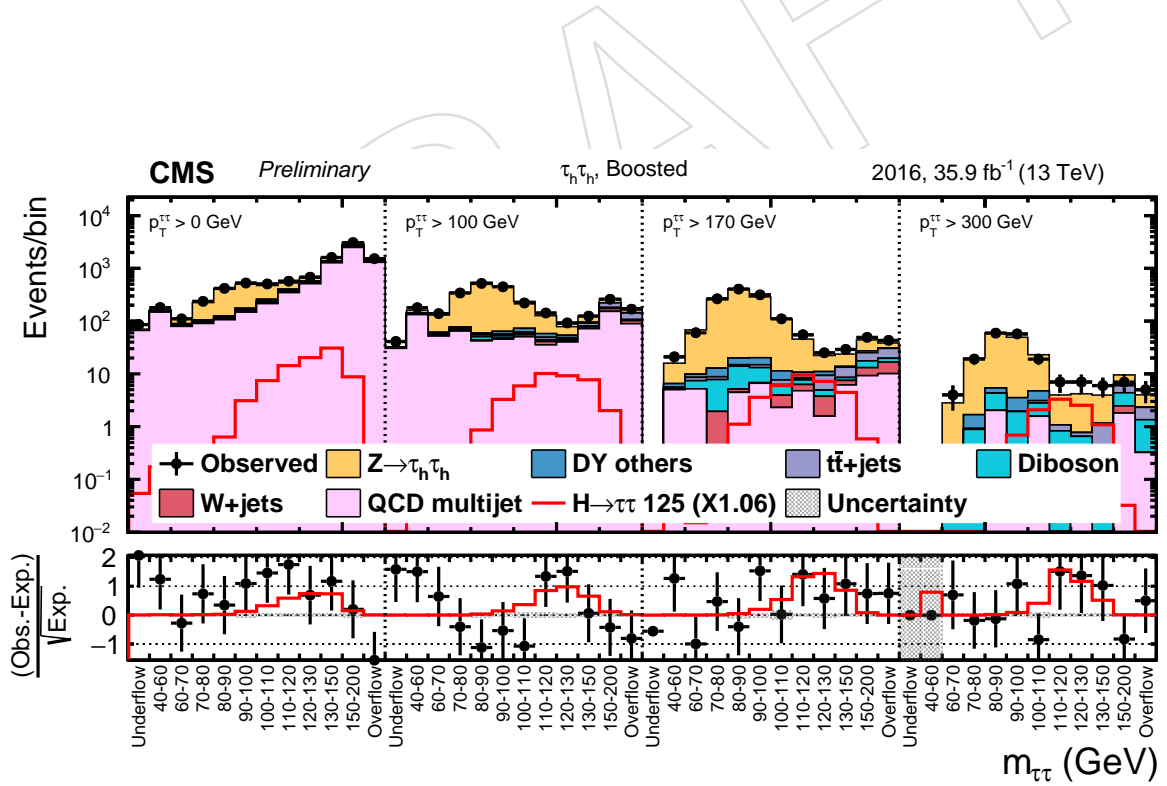


Figure 52: Pre-fit 2D distribution in the boosted category in the $\tau_h \tau_h$ final state.

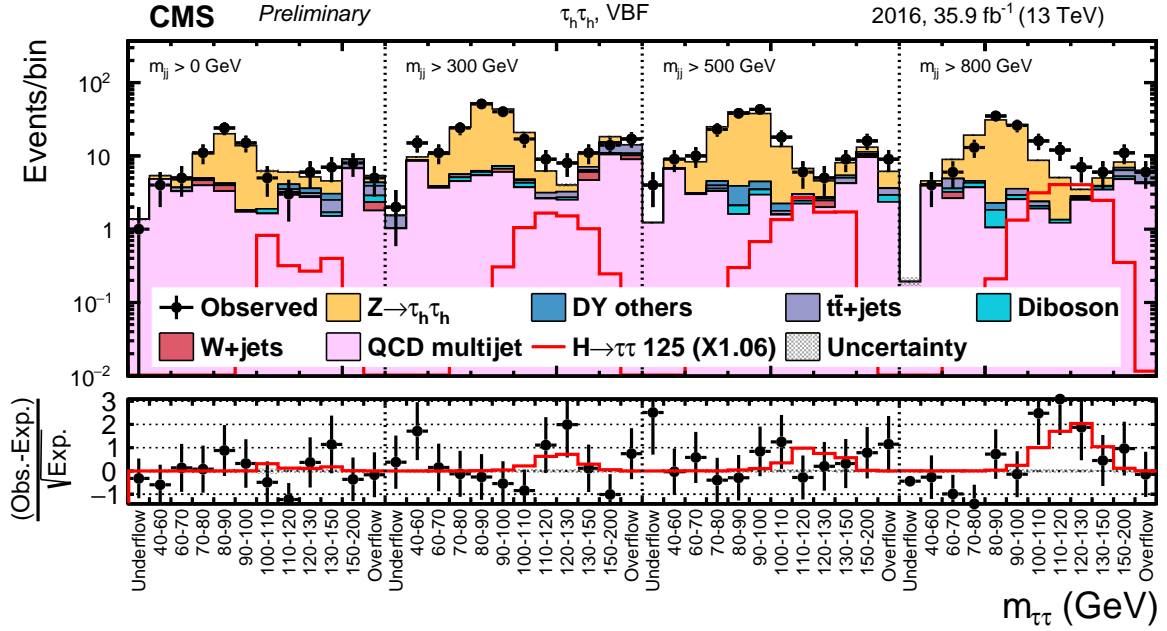


Figure 53: Prefit 2D distribution in the VBF category in the $\tau_h \tau_h$ final state.

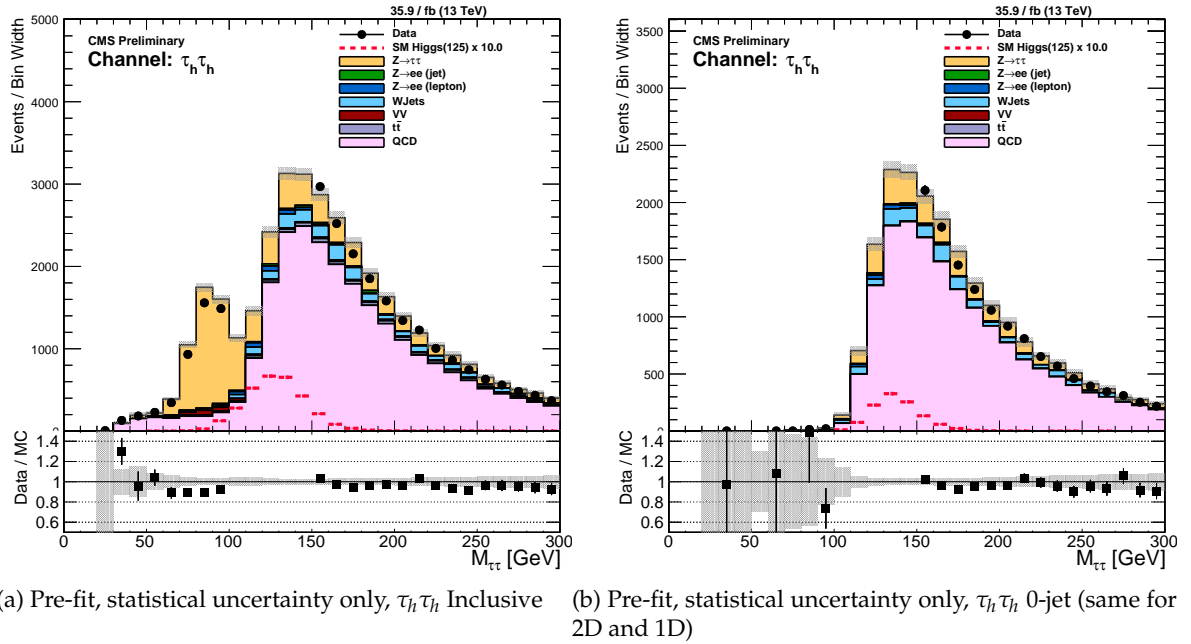


Figure 54: The SVfit distribution, inclusive selection (left) and 0 jet (right) category.

9 The $e\mu$ final state

9.1 Trigger requirements

The $e\mu$ final states are recorded with electron-muon cross triggers presented in Table 21.

9.2 Offline selection

Electrons are reconstructed by particle flow algorithm. The electron candidate is selected if it satisfies the following criteria.

- Candidate passes MVA based identification criteria discussed in section 3. The cut on the MVA discriminant is defined by the working point corresponding to the selection efficiency of 80% (WP80).
- Electron track is not identified as a photon conversion candidate (conversion veto).
- Number of missing inner hits ≤ 1 .
- Transverse and longitudinal impact parameters are required to be $d_{xy} < 0.45$ mm and $d_{xy} < 2$ mm;
- $\Delta\beta$ -corrected relative isolation, computed with the isolation cone $\Delta R < 0.3$, $Iso_e < 0.15$.
- Electron must have $p_T > 13$ GeV and $|\eta| < 2.5$. These kinematic criteria are tighter than those implemented at the HLT.

Muons are reconstructed by the PF algorithm. The muon candidate is selected if the following requirements are met.

- The muon candidate fulfills medium identification criteria outlined in section 3.
- Transverse and longitudinal impact parameters must fulfill $d_{xy} < 0.45$ mm and $d_{xy} < 2$ mm.
- $\Delta\beta$ -corrected relative isolation, computed for the isolation cone $\Delta R < 0.4$, $Iso_\mu < 0.2$.
- Muon candidate must have $p_T > 10$ GeV and $|\eta| < 2.4$. These kinematic criteria are tighter than those implemented at the HLT.

Each lepton is required to match respective trigger object of the fired trigger within the cone of $\Delta R < 0.4$. The transverse momentum of the lepton firing higher p_T leg of the trigger must be greater than 24 GeV. In MC samples, where the trigger is not simulated, at least one of the leptons must have $p_T > 24$ GeV.

The $e\mu$ pair is selected if $\Delta R(e, \mu) > 0.3$. If more than one $e\mu$ pair is accepted, the most isolated pair, i.e. with minimum sum of relative isolation variables, $\min(Iso_\mu + Iso_e)$, is chosen. The opposite sign (OS) $e\mu$ pairs are selected in the signal region, while the selected sample of the same sign (SS) pairs is used to define control regions to evaluate QCD multijet background as discussed later in this chapter.

To suppress backgrounds from the top pair events and the W+Jets(W+ $\gamma^{(*)}$) production the D_ζ observable defined in Equation 15, is exploited. This variable was introduced in the search for $H \rightarrow \tau\tau$ events by the CDF collaboration [36]. It is calculated as the difference of the projections of visible transverse momentum of τ decay products plus missing transverse momentum, $\vec{P}_{T,1}^{\text{vis}} + \vec{P}_{T,2}^{\text{vis}} + \vec{P}_T^{\text{mis}}$, and simply visible transverse momentum of τ decay products on the axis ζ . Here, ζ is the axis bisecting the directions $\vec{P}_{T,1}^{\text{vis}}$ and $\vec{P}_{T,2}^{\text{vis}}$ of the visible τ decay products in the transverse plane. This variable quantifies the compatibility of event with the topology, where

HLT Trigger	Runs available	L1 seed
HLT_Mu8_TrkIsoVVL_Ele23_CaloIdL_TrackIdL_IsoVL_v	B-F	L1_Mu5_IsoEG18 OR L1_Mu5_IsoEG20 OR L1_Mu5_EG23
HLT_Mu23_TrkIsoVVL_Ele12_CaloIdL_TrackIdL_IsoVL_v	B-F	L1_Mu20_EG10 OR L1_Mu23_EG10
HLT_Mu8_TrkIsoVVL_Ele23_CaloIdL_TrackIdL_IsoVL_DZ_v	G-H	L1_Mu5_IsoEG18 OR L1_Mu5_IsoEG20 OR L1_Mu5_EG23
HLT_Mu23_TrkIsoVVL_Ele12_CaloIdL_TrackIdL_IsoVL_DZ_v	G-H	L1_Mu20_EG10 OR L1_Mu23_EG10

Table 21: Triggers used in the analysis of the $e\mu$ final state.

the direction of missing neutrinos from τ decays are aligned with the direction of the visible τ decay products. In the $e\mu$ channel the quantities $\vec{P}_{T,1}^{\text{vis}}$ and $\vec{P}_{T,2}^{\text{vis}}$ correspond to the transverse momenta of electron and muon.

$$D_\zeta = P_\zeta - 1.85 P_\zeta^{\text{vis}}$$

with $P_\zeta = (\vec{P}_{T,1}^{\text{vis}} + \vec{P}_{T,2}^{\text{vis}} + \vec{P}_T^{\text{mis}}) \frac{\vec{\zeta}}{|\vec{\zeta}|}$

and $P_\zeta^{\text{vis}} = (\vec{P}_{T,1}^{\text{vis}} + \vec{P}_{T,2}^{\text{vis}}) \frac{\vec{\zeta}}{|\vec{\zeta}|}$

(15)

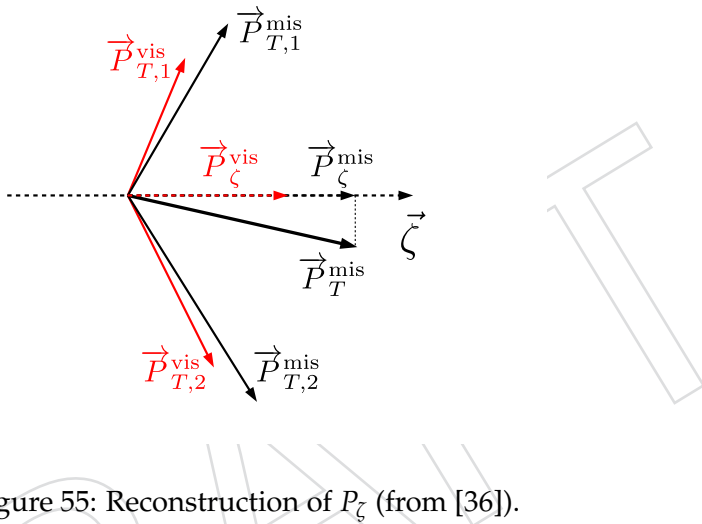


Figure 55: Reconstruction of P_ζ (from [36]).

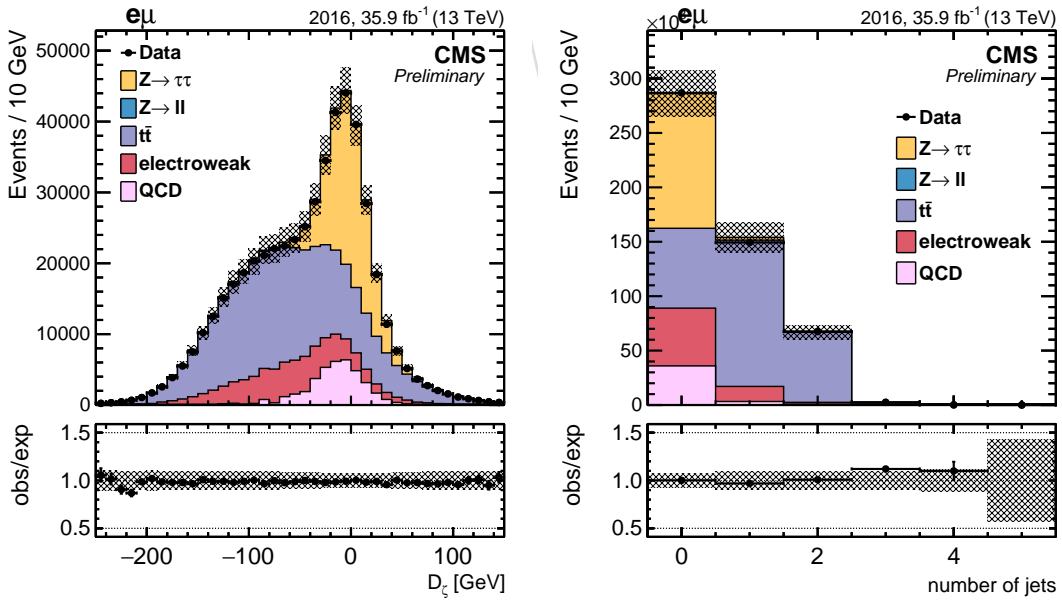


Figure 56: Distribution of the D_ζ variable (left) and b-tagged jet multiplicity (right) in data and simulated samples.

The cut on D_ζ variable is optimized separately for each event category discussed later.

Category	Definition
0-jet low	nntag=0 and njets=0 and $15 < p_T^\mu < 35$ GeV and $D_\zeta > -35$ GeV
0-jet high	nntag=0 and njets=0 and $p_T^\mu \geq 35$ GeV and $D_\zeta > -35$ GeV
1-jet low	nntag=0 and (njets=1 or (njets=2 and $m_{jj} < 500$ GeV)) and $15 < p_T^\mu < 35$ GeV and $D_\zeta > -35$ GeV
1-jet high	nntag=0 and (njets=1 or (njets=2 and $m_{jj} < 500$ GeV)) and $p_T^\mu \geq 35$ GeV and $D_\zeta > -35$ GeV
vbf low	nntag=0 and njets=2 and $p_T^\mu > 15$ GeV and $500 < m_{jj} \leq 800$ GeV and $D_\zeta > -10$ GeV
vbf high	nntag=0 and njets=2 and $p_T^\mu > 15$ GeV and $m_{jj} > 800$ GeV and $D_\zeta > -10$ GeV

Table 22: Definition of event categories in the $e\mu$ channel.

976 The top-pair and single-top background processes are further suppressed by rejecting events
 977 with at least one b-tagged jet. The distribution of the D_ζ variable and b-tagged jet multiplicity
 978 are presented in Figure 56.

979 9.3 MC corrections

980 A set of corrections is applied to simulated events to improve agreement between data and
 981 simulation. These corrections are discussed in detail in Section 4

982 9.4 Event categories and signal extraction

983 The search sensitivity is improved by exploiting distinct signatures of the various signal pro-
 984 duction processes, the gluon-gluon fusion without hard jets accompanying Higgs boson, the
 985 gluon-gluon fusion production of the Higgs boson in association of one or more jets, and the
 986 vector boson fusion process. Events are classified into categories based on jet multiplicity
 987 (njets), muon transverse momentum (p_T^μ), and invariant mass of two leading jets (m_{jj}) in events
 988 with two or more jets. Definition of optimized categories for the 1D analysis is detailed in Ta-
 989 ble 22. In each event category signal is extracted from the fit of the invariant mass distribution
 990 of the τ pair. The mass of the τ pair is reconstructed by SVFit algorithm. In practice, these
 991 categories are not used to extract the final results, but can be used to compare the sensitivity of
 992 the 2D analysis with the 1D analysis.

993 The signal extraction for this analysis implies fits of two-dimensional (2D) distributions. For
 994 this option, the event categorization and variables used in 2D fit are presented in Table 23.

Category	Definition	Variables used in 2D fit
0-jet	nntag = 0 and njets = 0 and $D_\zeta > -35$ GeV	(m_{vis}, p_T^μ)
boosted	nntag = 0 and (njets=1 or (njets≥2 and $m_{jj} < 300$ GeV)) and $D_\zeta > -35$ GeV	$(m_{\tau\tau}, p_{\tau\tau})$
vbf	nntag = 0 and njets≥2 and $m_{jj} \geq 300$ GeV and $D_\zeta > -10$ GeV	$(m_{\tau\tau}, m_{jj})$

Table 23: Definition of event categories in the $e\mu$ channel for the option of extracting signal with fits of the 2D distributions.

995 9.5 Background estimation

996 Drell-Yan background

997 The Drell-Yan background is estimated with MC simulation. To improve the modeling of the Z
 998 boson kinematics, the Z boson (p_T ,mass)-dependent weights are applied to simulated events,
 999 as detailed earlier.

1000 As described for the $\mu\tau_h$ final state in Section 6.3.1, data/MC scale factors are applied to the
 1001 Drell-Yan background based on the data/MC agreement in a $Z \rightarrow \mu\mu$ enriched control region.

1002 The scale factors are applied inclusively for the 0-jet category, and per slice of m_{jj} or Higgs p_T
 1003 in the VBF or boosted categories respectively.

1004 Top pair background

1005 The $t\bar{t}$ shape is estimated from Monte Carlo samples. To improve the modeling of top pair
 1006 kinematics, a top and anti-top p_T dependent weighting is applied to $t\bar{t}$ events, as detailed in
 1007 Section 4. The correction is validated in the control regions with high $t\bar{t}$ purity. We define a
 1008 control region in the $e\mu$ channel as $P_\zeta < -35$ and $E_T^{\text{miss}} > 80$ GeV. Distribution of the invariant
 1009 mass of the $e\mu$ pair (m_{vis}) without and with applying reweighting is shown in Figure 57. The
 1010 correction flattens the ratio of data yield to the yield of simulated events as a function of (m_{vis}),
 1011 indicating improvement in the modeling of the shape of $t\bar{t}$ background.

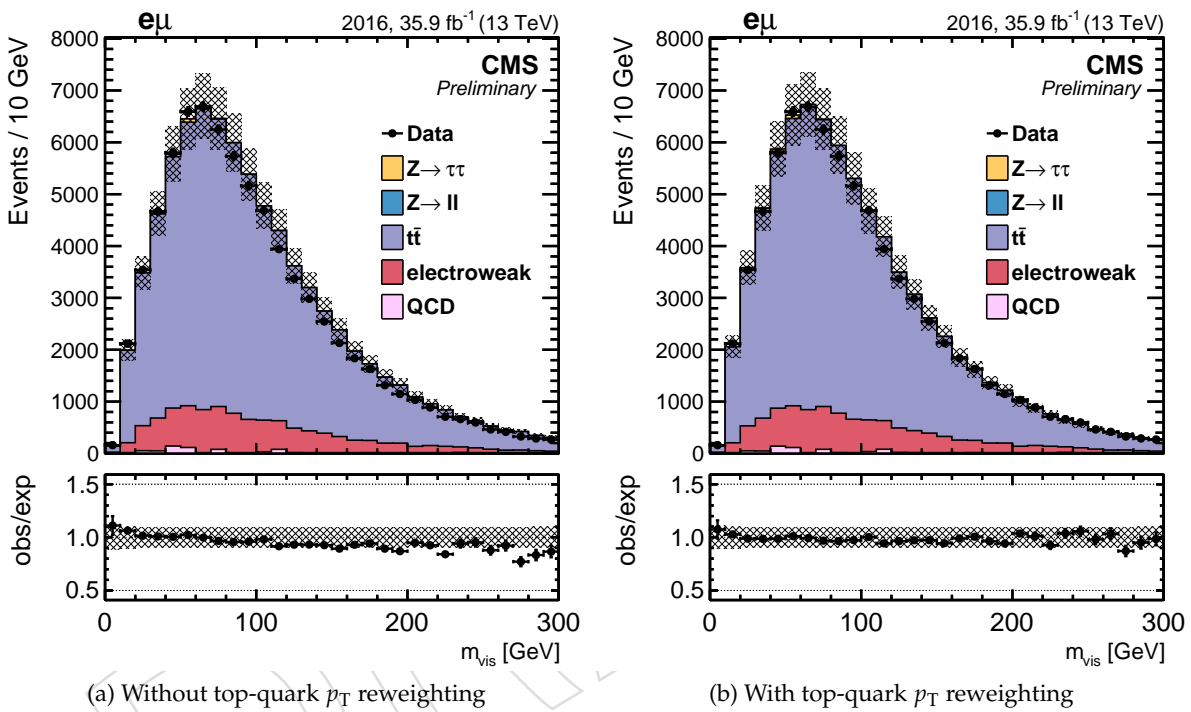


Figure 57: Effect of applying top quark p_T reweighting on the distribution of the $e\mu$ pair invariant mass (m_{vis}) in a $t\bar{t}$ enriched region ($D_\zeta < -35$, $E_T^{\text{miss}} > 80$ GeV) in the $e\mu$. Applying the reweighting improves agreement in the shape of the distribution between data and simulation.

1012 As explained for the other final states and detailed in Section 10, the $t\bar{t}$ normalization is ex-
 1013 tracted from the simultaneous fit of a $t\bar{t}$ -enriched control region together with the various sig-
 1014 nals. The control region is defined in the $e\mu$ final state, with an inverted cut on P_ζ to
 1015 reject the signal and increase the $t\bar{t}$ purity.

1016 QCD multijets

1017 The contribution of the multijet background in the signal region, in which electron and muon
 1018 are required to be of opposite (OS) charge, is estimated using a control region in which electron
 1019 and muon are of the same (SS) charge. The ratio of $e\mu$ pairs with OS to $e\mu$ pairs with SS
 1020 charge is measured in events which fail the nominal lepton isolation criterion of $Iso_e < 0.15$
 1021 and $I_\mu < 0.20$. The OS/SS ratio is found to vary as a function of the isolation criteria that are
 1022 applied in the isolation sideband (SB). The nominal OS/SS ratio is measured in the SB region
 1023 that is defined by requiring that both leptons satisfy a relaxed isolation criterion of $Iso_{e,\mu} < 0.5$

and at least one lepton fails the nominal isolation requirement, $I_e > 0.15$ or $I_\mu > 0.20$, to avoid overlap with the signal region. The measurement is performed in the event sample of selected $e\mu$ pairs with additional requirement $D_\zeta > -35$ GeV, which suppresses contribution from the $t\bar{t}$, W+Jets and diboson backgrounds and after rejecting events with at least one b-tagged jet. The OS/SS ratio is computed after subtraction from data yields the contribution of non-QCD processed estimated from simulation (Equation 16).

$$\frac{\text{OS}}{\text{SS}} = \frac{N_{\text{data}}^{\text{OS}} - N_{\text{MC}}^{\text{OS}}(\text{Non QCD})}{N_{\text{data}}^{\text{SS}} - N_{\text{MC}}^{\text{SS}}(\text{Non QCD})} \quad (16)$$

Table 24 compares the integrated OS/SS ratio measured in SB with predictions from simulation. Also presented is the OS/SS ratio determined from simulation in the signal region with isolated electron and muon (SR).

Table 24: The integrated OS/SS ratio measured in isolation sideband region SB. The measurement is compared with the prediction from simulation. Also presented is the OS/SS ratio in the signal region as predicted by simulation.

Region	Data	Simulation
SB	2.41 ± 0.02	2.70 ± 0.19
SR	—	2.49 ± 0.30

The measurement is then performed in SB individually for each event category presented in Table 23. The measurements performed in SB are extrapolated to SR using extrapolation factor determined from simulation for inclusive selection:

$$F_{\text{iso}} = \frac{(\text{OS/SS})_{\text{MC}}^{\text{SR}}}{(\text{OS/SS})_{\text{MC}}^{\text{SB}}}, \quad (17)$$

where $(\text{OS/SS})_{\text{MC}}^{\text{SR}}$ and $(\text{OS/SS})_{\text{MC}}^{\text{SB}}$ are OS/SS ratio derived in SB and SR respectively, from the simulated sample of QCD multijet events as presented in Table 24. The limited statistics of QCD MC sample doesn't allow to determine extrapolation factor F_{iso} in "boosted" and "vbf" categories in reliable way.

The OS/SS ratio in each event category is computed as presented in Eq. 18.

$$(\text{OS/SS})_{\text{data}}^{\text{SR,cat}} = F_{\text{iso}} \cdot (\text{OS/SS})_{\text{data}}^{\text{SB,cat}}, \quad (18)$$

where F_{iso} extrapolation factor from SB to SR determined from Eq. 17, and $(\text{OS/SS})_{\text{data}}^{\text{SB,cat}}$ is the OS/SS ratio measured from data in SB according to Eq. 16.

Results of OS/SS ratio measurements in SB and SR are presented in Table 25. The OS/SS ratios are used to determine expected yields of QCD events:

$$N_{\text{QCD,cat}} = (N_{\text{SS,cat}}^{\text{data}} - N_{\text{SS,cat}}^{\text{non-QCD}}) \cdot (\text{OS/SS})_{\text{data,cat}}, \quad (19)$$

The SS regions with isolated electrons and muons have a large fraction of non-QCD events. The contamination from the Drell-Yan, W+Jets, $t\bar{t}$ and diboson processes ranges from 40% in the "0-jet" category up to 70% in the "boosted" category. In order to reduce contribution of the non-QCD processes and enhance statistics in the QCD templates used in extraction of signal, a

Table 25: The integrated OS/SS ratio measured in the isolation sideband region SB and OS/SS ratio is the signal region computed according to Eq. 18 for different event categories.

Event category	$(OS/SS)_{SB}$	$(OS/SS)_{SR}$
0-jet	2.46 ± 0.02	2.26 ± 0.31
boosted	2.45 ± 0.04	2.25 ± 0.31
vbf	3.08 ± 0.47	2.83 ± 0.58

1046 dedicated control sample is introduced for modelling of the QCD multijet background shape.
 1047 This control sample, denoted SB_{shape} , is defined by imposing relaxed isolation requirements
 1048 on leptons: $0.2 < Iso_\mu < 0.5$ and $Iso_e < 0.5$ in the “vbf” category and $0.1 < Iso_\mu < 0.3$
 1049 and $Iso_e < 0.3$ in the “0-jet” and “boosted” categories. The purity of QCD multijet events in
 1050 this sample ranges from 10% in the “0-jet” category to 20% in the “boosted” category. The
 1051 compatibility of shapes of the key variables between the signal region and the sideband region
 1052 SB_{shape} is illustrated in Fig. 58.

1053 The QCD templates derived in the control sample SB_{shape} in each event category, are normal-
 1054 ized to the respective yields computed according to Eq. 19.

1055 W+Jets, diboson and single-top production

1056 Contribution from the W+Jets, diboson and single-top background processes is fully estimated
 1057 from simulation.

1058 9.6 Control Plots

1059 The data/MC agreement is checked with a set of control plots. Some representative distribu-
 1060 tions obtained after applying cut $D_\zeta > -35$ GeV are shown in Fig 59.

1061 9.7 Mass plots

1062 The pre-fit plots illustrating the mass distributions in each 2D category, after compressing the
 1063 other dimension are shown in 60. A good pre-fit agreement is seen in each category. Only
 1064 statistical uncertainty is indicated in the plots.

1065 The pre-fit unrolled 2D distributions are shown in Figs. 61-63.

1066 10 Fit model

1067 Results are extracted by a simultaneous fit of the three categories (0 jet, VBF, boosted) per final
 1068 state. The systematic uncertainties included as nuisance parameters in the fit are detailed in
 1069 the next chapter.

1070 In addition to these signal regions, several control regions are included in the fit.

1071 First, a region to control the $t\bar{t}$ background is introduced in the fit. It is defined with the same
 1072 baseline selection as used for the $e\mu$ final state, except that the cut on P_ζ is inverted: $P_\zeta < -35$
 1073 GeV. To reduce the small Drell-Yan contamination in this region, the visible invariant mass
 1074 between the muon and the electron is required to be greater than 90 GeV. The diboson con-
 1075 tamination is reduced by requiring at least one jet in the final state. The purity achieved is
 1076 about 85%. No requirement is made on the number of b-tagged jets because b-tagging is not
 1077 used in the analysis, and because large uncertainties arise from tagging b jets. Only one bin is

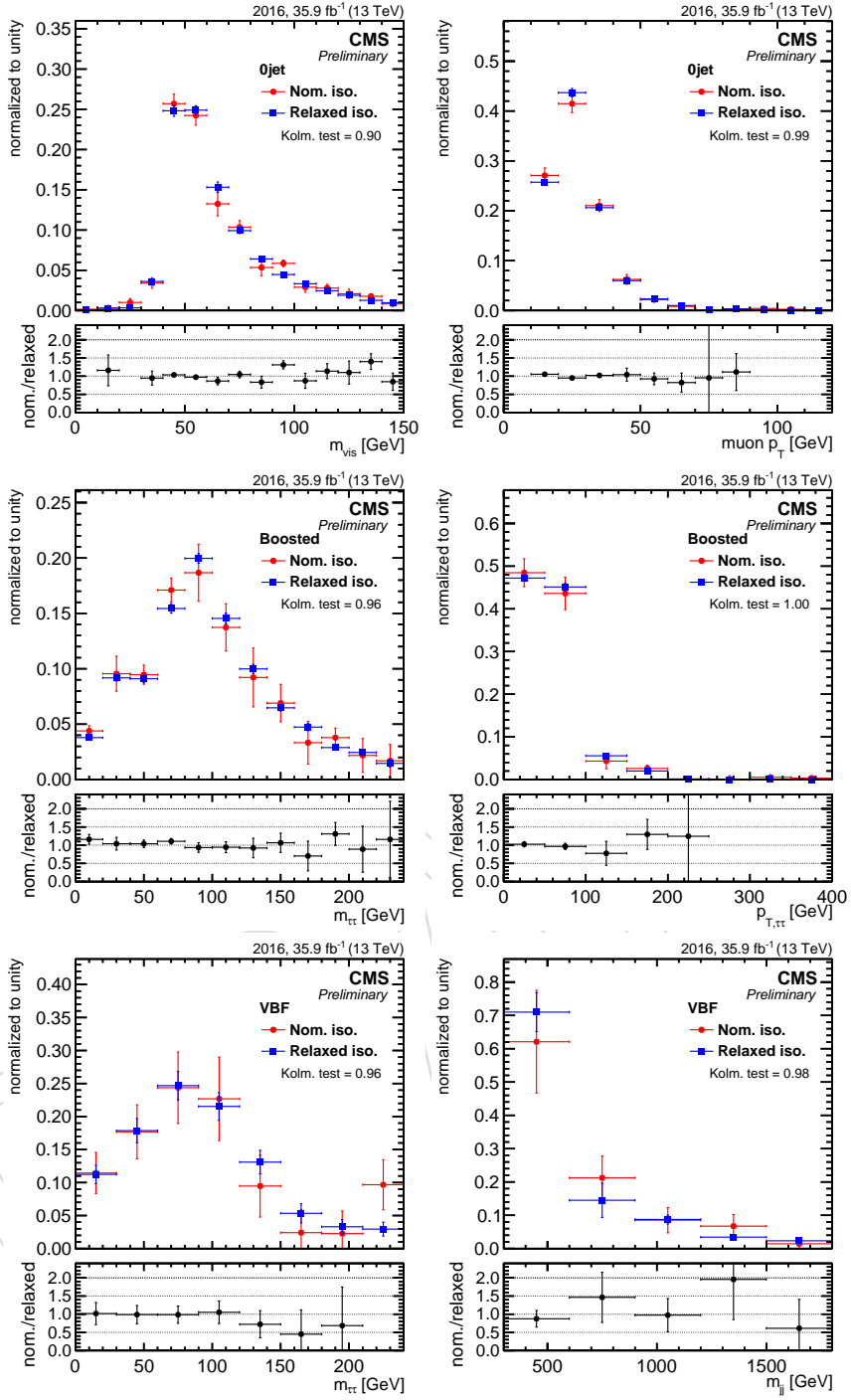


Figure 58: Distribution of the key variables used for the extraction of the signal in the signal region (red points) and sideband region SB_{shape} (blue points). Top-left : invariant mass of the $e\mu$ pair in the “0-jet” category. Top-right : muon p_T in the “0-jet” category. Middle-left : di-tau invariant mass in the “boosted” category. Middle-right : p_T of the di-tau system in the “boosted” category. Bottom-left : di-tau invariant mass in the “vbf” category. Bottom-right : dijet invariant mass in the “vbf” category.

1078 considered for the control region distribution, as shown in Fig. 64. No dedicated uncertainty
 1079 is assigned to the extrapolation from this single control region to the various categories in the

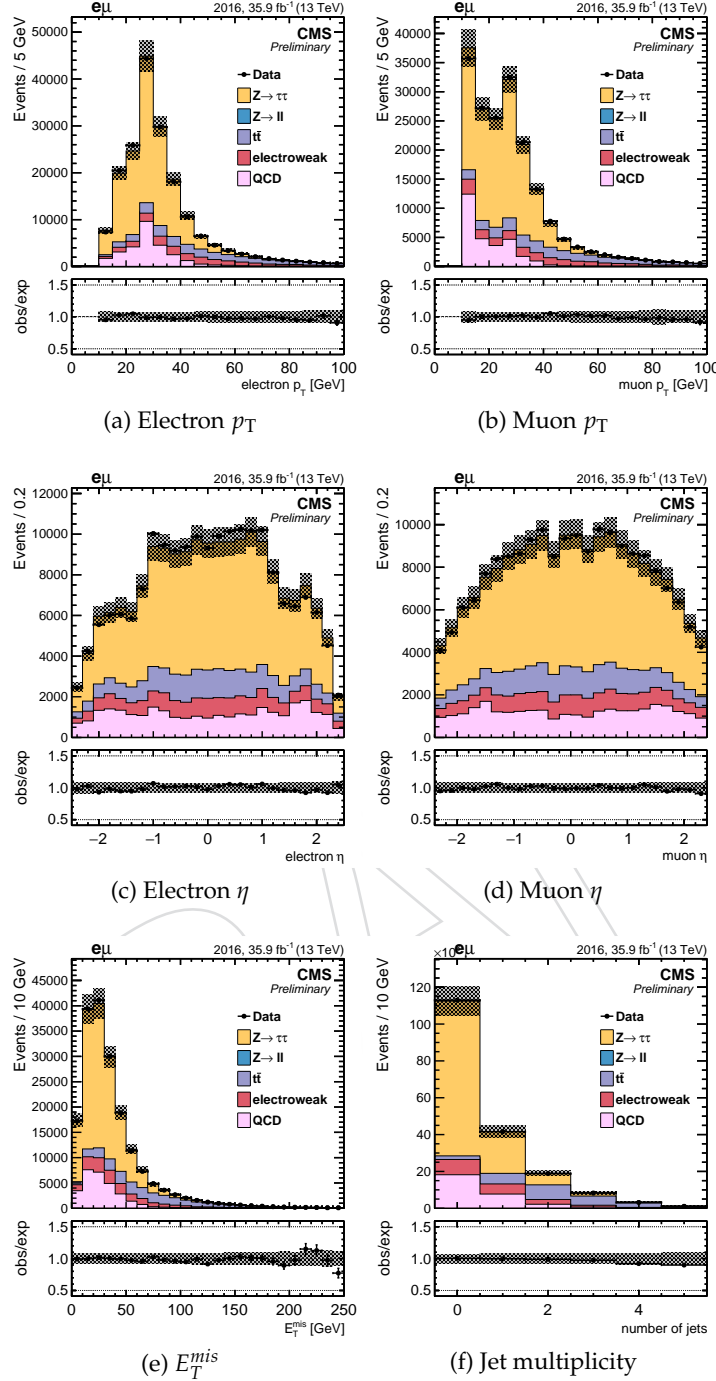


Figure 59: Control distributions in the $e\mu$ channel obtained after applying requirement $D_\zeta > -35$ GeV and rejecting events with at least one b-tagged jet.

1080 different final states, because:

- 1081 • the top p_T reweighting uncertainty, which is taken into account for the $t\bar{t}$ background
1082 in the signal and control regions, already covers uncertainties due to missing orders,
1083 which could affect the low-to-high P_ζ extrapolation scale factor;
- 1084 • the data/MC agreement in the $t\bar{t}$ control region has been checked to remain the same

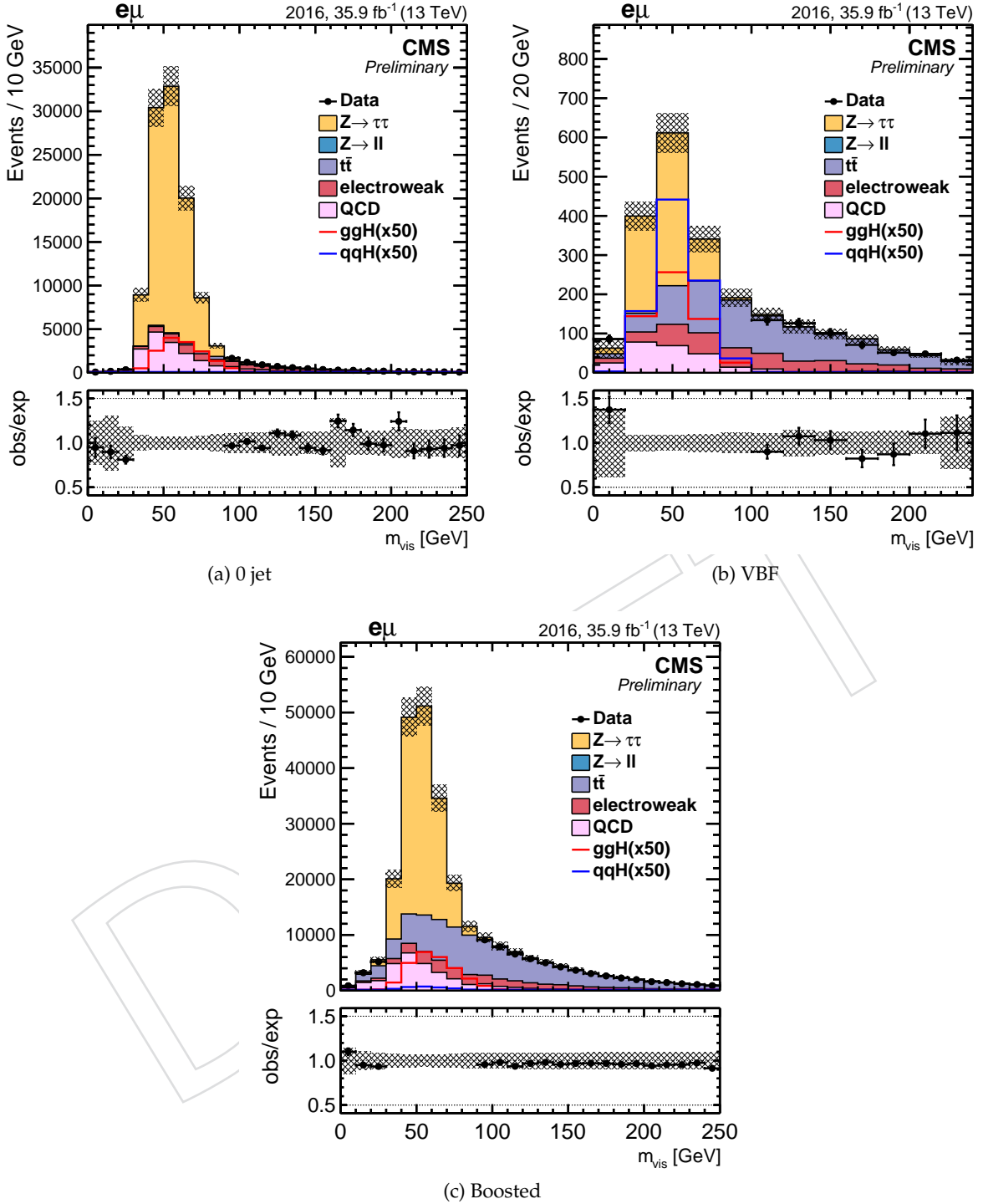


Figure 60: Pre-fit mass distributions in the $e\mu$ channel.

after changing the electron and muon p_T cuts to mimick the kinematic cuts in the $e\tau_h$, $\mu\tau_h$, and $\tau_h\tau_h$ final states better (typically higher p_T leptons).

The uncertainty from the fit in the control region is automatically propagated to the $t\bar{t}$ background in the signal region.

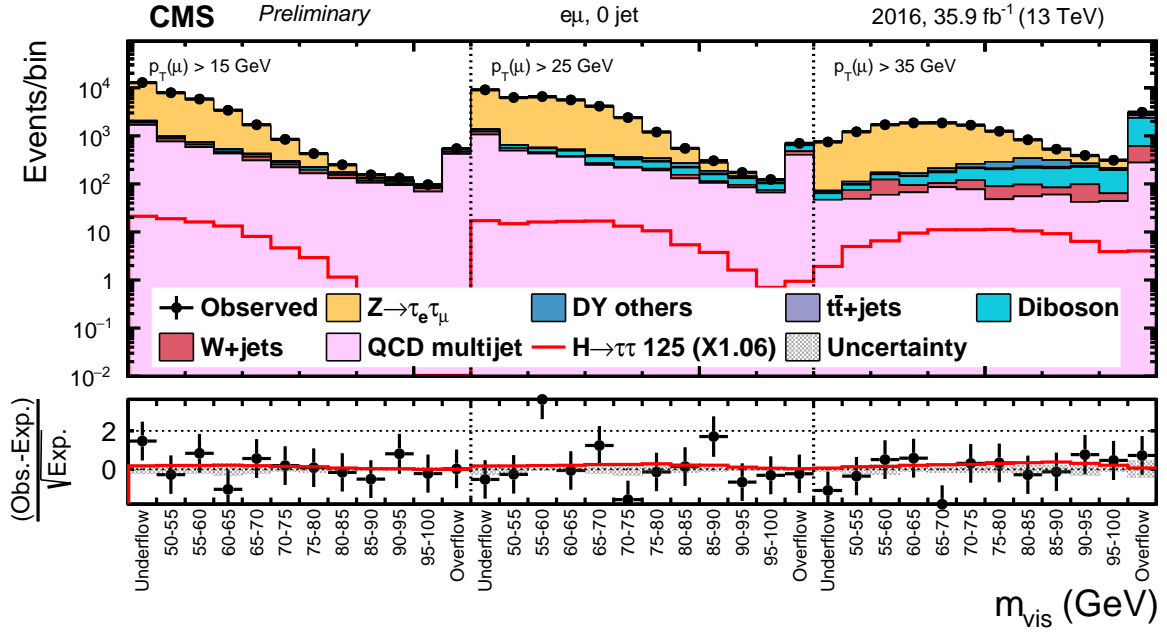


Figure 61: Pre-fit unrolled 2D distributions in the 0 jet category of the $e\mu$ channel.

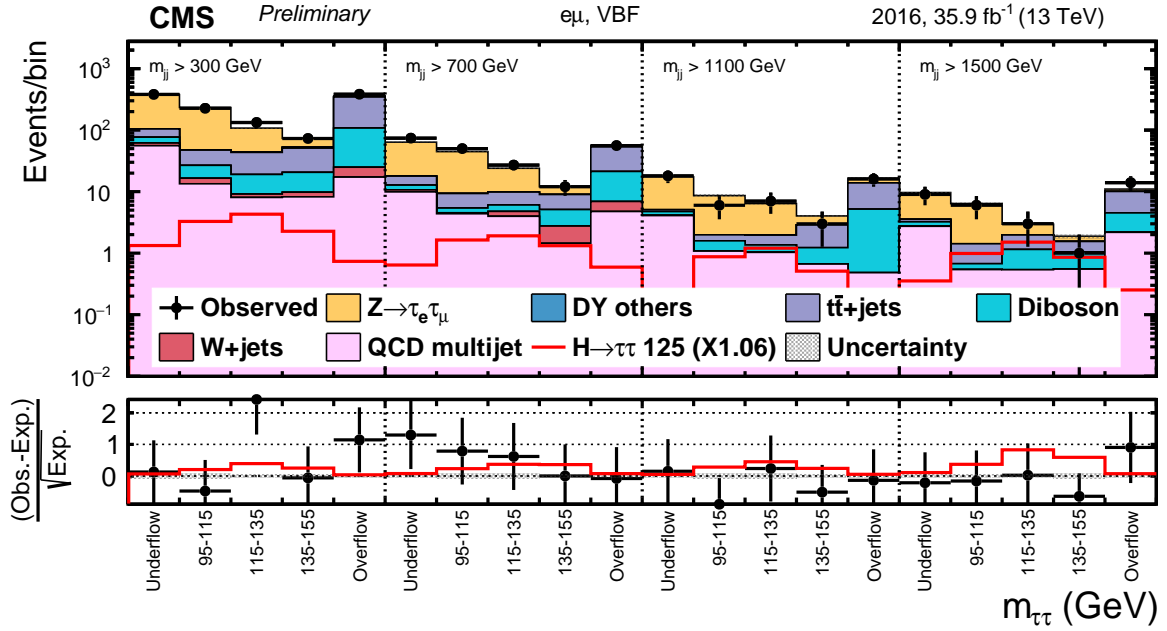


Figure 62: Pre-fit unrolled 2D distributions in the VBF category of the $e\mu$ channel.

1089 Second, control regions for the $W + \text{jets}$ background in the $e\tau_h$ and $\mu\tau_h$ final states, are also added
 1090 to the fit model. One control region per category and per final state is included. The control
 1091 regions are defined in the same way as the signal regions, except that b-tagged jets are vetoed
 1092 to reduce $t\bar{t}$ in $W + \text{jets}$ control region and the m_T cut is modified: $m_T > 80 \text{ GeV}$. Again, only one
 1093 bin per distribution is considered. The control distributions for the three categories can be seen
 1094 in Fig. 65 and 66, in the $\mu\tau_h$ and $e\tau_h$ final states respectively. $W + \text{jets}$ has already been scaled so
 1095 that background predictions match data, but it is free to float in the fit.

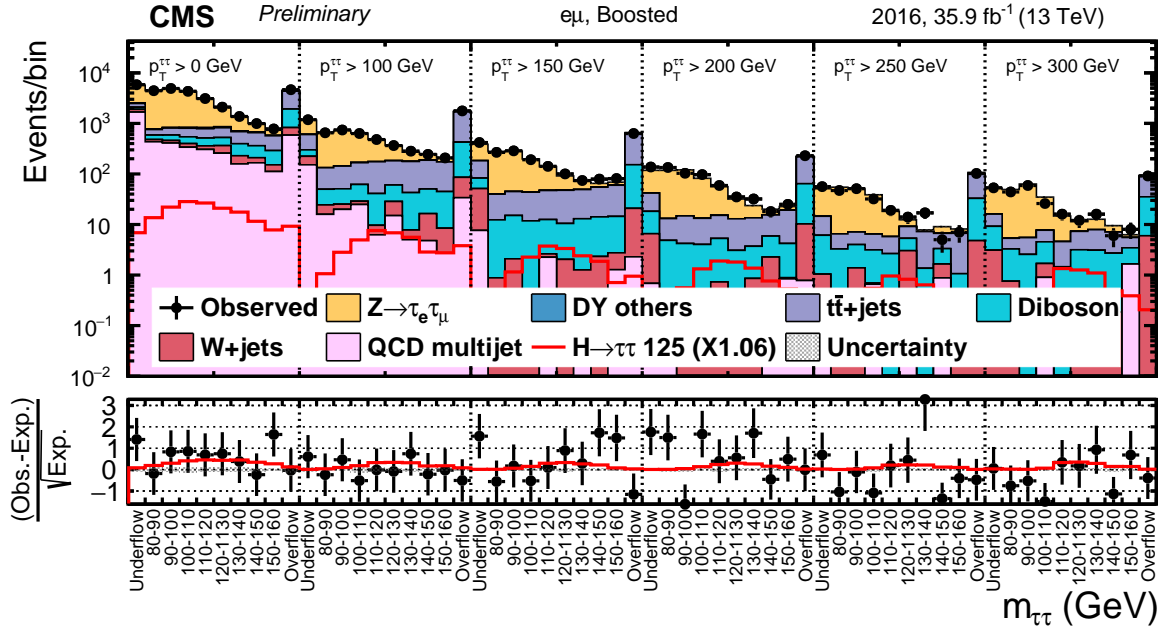


Figure 63: Pre-fit unrolled 2D distribution in the boosted category of the $e\mu$ channel.

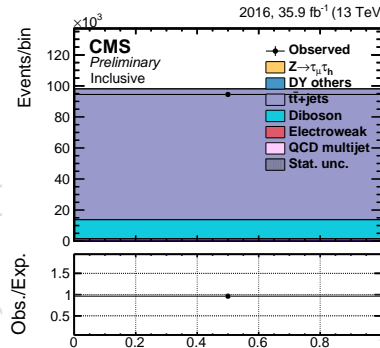
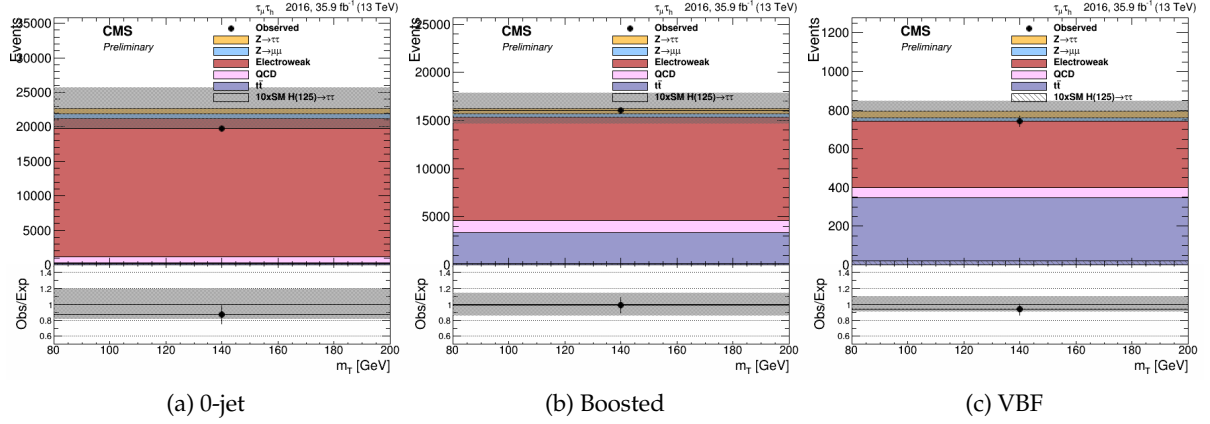
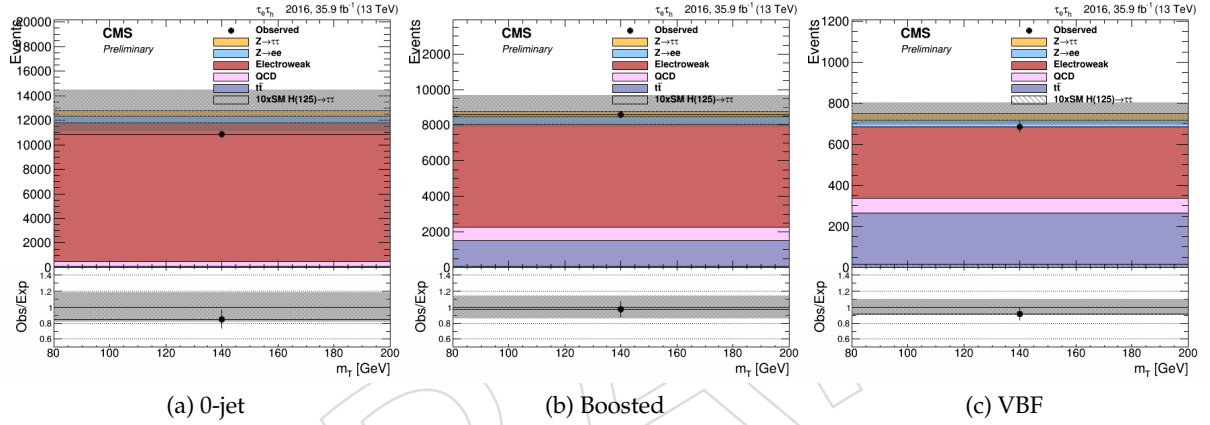
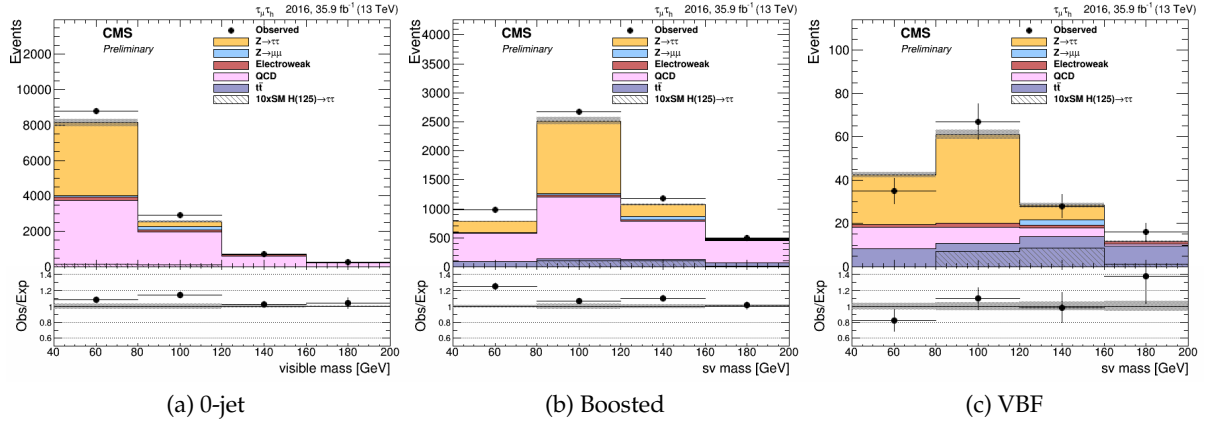


Figure 64: $t\bar{t}$ control region.

- 1096 Third, control regions for the QCD background in the $e\tau_h$ and $\mu\tau_h$ final states are also added
 1097 to the fit model. One control region per category and per final state is included. The control
 1098 regions are defined in the same way as the signal regions, except that the muon/electron and τ_h
 1099 isolations are relaxed. In particular, the relative isolation of the muon (electron) is required to
 1100 be between 0.15 and 0.30 (0.10 and 0.30). Four bins per distribution are included to take benefit
 1101 from the different mass distributions of the QCD, W+jets, and Drell-Yan processes. The QCD
 1102 control regions are shown in Fig. 67 and 68, in the $\mu\tau_h$ and $e\tau_h$ final states respectively.
 1103 It can be noted that no control region for the Drell-Yan background is included, but scale fac-
 1104 tors and uncertainties from the $Z \rightarrow \mu\mu$ region have been taken into account to create the
 1105 background shapes in the signal regions, as described previously in the text.

Figure 65: W+jets control regions in the $\mu\tau_h$ final state.Figure 66: W+jets control regions in the $e\tau_h$ final state.Figure 67: QCD control regions in the $\mu\tau_h$ final state.

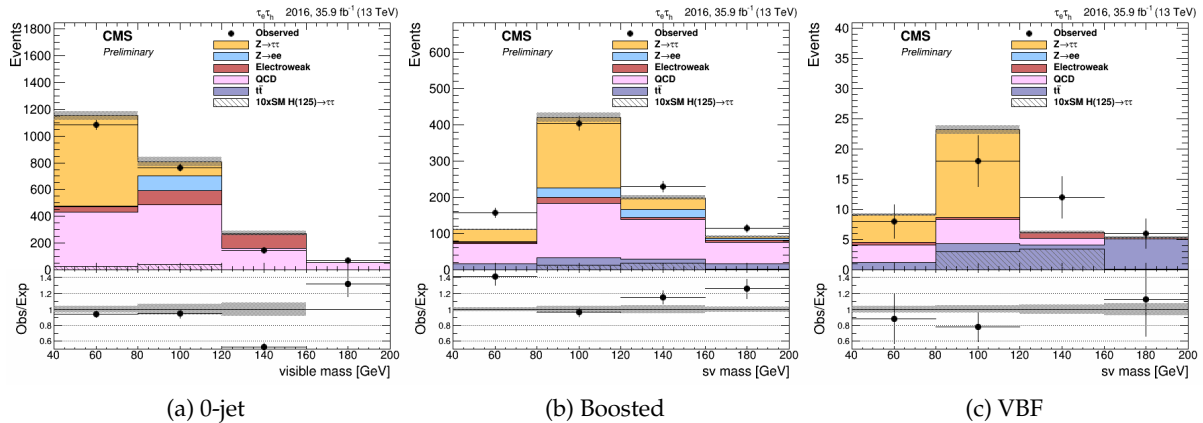


Figure 68: QCD control regions in the $e\tau_h$ final state.

11 Systematic uncertainties

Systematic uncertainties considered in this analysis affect the distribution and/or the normalization of background and signal processes.

11.1 Lepton isolation and identification

The uncertainty related to the identification of muons amounts to 2%. It is applied to all processes fully estimated from MC samples. In the $\mu\tau_h$ final state, this uncertainty does not affect the normalization of the W+jets background because it is estimated from data in a high- m_T control region.

Similarly, 2% uncertainty is assigned to the yield of MC processes with real electrons in the $e\mu$ and $e\tau_h$ final states, to account for the uncertainty in the electron isolation and identification efficiency.

The uncertainty in the data/MC scale factor related to the identification of hadronically decaying taus is 5%, as recommended by Tau POG. This uncertainty is applied to events with real hadronic taus, determined from generator-level matching. In particular the $t\bar{t}$ process is split into a component with real hadronic taus, and a component with other generated objects, so that the uncertainty is applied only to the first component (other uncertainties, described later in the text, are assigned to the other component). A fraction of this uncertainty, 4%, is fully correlated between final states, whereas the remaining component is uncorrelated between final states to account for differences in the anti-lepton discriminators applied. In the $\tau_h\tau_h$ final state, the fully correlated part of the uncertainty amounts to 8%, whereas the uncorrelated part also accounts for an uncertainty in the double tau trigger efficiency, which amounts to 7% in total for both tau legs.

In the 0 jet category of the $e\tau_h$ and $\mu\tau_h$ channels, events are separated based on the reconstructed tau decay mode. An uncertainty related to possible differences between the reconstruction/identification of hadronic taus in the various decays modes is considered. Each decay mode is allowed to fluctuate by 3%, while adjusting the other decay modes to keep the overall normalization constant.

1133 **11.2 Luminosity**

1134 The uncertainty in the collected integrated luminosity in 2016 amounts to 2.6%. It is applied
 1135 to all processes whose normalization is taken from MC simulations, and it is fully correlated
 1136 between categories and final states.

1137 **11.3 W+jets estimation**

1138 In the $e\mu$ and $\tau_h\tau_h$ final states, the W+jets background is small relative to other processes, and it
 1139 is estimated purely from MC simulations. In this case, an uncertainty of 4% is assigned to the
 1140 cross section of the process. It should be noted that additional uncertainties, described later in
 1141 the text, account for the $j \rightarrow \tau_h/e/\mu$ fake rates.

1142 In the $e\tau_h$ and $\mu\tau_h$ final states, the W+jets background is normalized in a high m_T sideband.
 1143 Several uncertainties have to be taken into account in the signal region: the extrapolation from
 1144 high- m_T to low- m_T , the statistical uncertainty of data and subtracted MC processes in the side-
 1145 band, and the systematic uncertainties in the subtracted MC simulations in the sideband. The
 1146 W+jets background is estimated separately for each category and each final state, and the cor-
 1147 responding uncertainties are fully uncorrelated.

1148 The combination of the statistical uncertainty of data, the statistical uncertainty of W+jets, and
 1149 20% uncertainty on the QCD background and 6% on the $t\bar{t}$ background, in the high- m_T region
 1150 result in, respectively, 5%, 5% and 25%, in the 0-jet, boosted, and VBF categories. The larger
 1151 uncertainty in the case of the VBF category is related to the larger statistical uncertainty, and
 1152 to a lower W+jets purity than the other categories because of the contribution of $t\bar{t}$ events. The
 1153 magnitude of these uncertainties is not used as an input to the combination tool, but control
 1154 regions for the W+jets background are added in the fit, and the corresponding uncertainties are
 1155 taken into account by the fit.

1156 An additional uncertainty in the high- m_T to low- m_T extrapolation scale factor is considered
 1157 in addition to the previously mentioned sources of uncertainty. This uncertainty accounts for
 1158 potential mismodeling of the transverse mass variable in MC simulations, leading to a biased
 1159 extrapolation of the normalization from the high- to low- m_T sidebands. The method to deter-
 1160 mine the magnitude of this uncertainty was called the "Ersatz method" in Run-1. It consists
 1161 in selecting very pure $Z \rightarrow \mu\mu$ events in data, and replacing one of the muons by transverse
 1162 missing energy to mimic $W \rightarrow \mu\nu$ events in data. This ersatz W+jets data sample can then be
 1163 compared to a $Z \rightarrow \mu\mu$ MC sample where one of the muons has also been replaced by MET.
 1164 The high to low m_T ratios are compared in both cases, and an uncertainty is determined based
 1165 on the statistical uncertainty of the samples (the Z +jets cross section is about one order of mag-
 1166 nitude lower than the W+jets cross section) and on the potential non closure between ersatz
 1167 data and MC samples. In practice $Z \rightarrow \mu\mu$ events are selected in data by requiring the events
 1168 to pass a combination of single muon triggers (IsoMu22 OR IsoTkMu22), to contain two oppo-
 1169 site sign muons with $p_T > 25$ GeV, passing the medium 2016 ID, and with a relative isolation
 1170 less than 0.15, and to contain a loose τ_h candidate passing the very loose tau MVA isolation, the
 1171 tight discriminator against muons and the very loose discriminator against electrons. Events
 1172 with additional electrons or muons are discarded, and the invariant mass of the two muons is
 1173 required to lie between 80 and 100 GeV to obtain a high purity sample. One of the muons is
 1174 selected randomly (if the event number is odd the leading muon is selected) to be replaced by
 1175 MET, and the tau is required to have an opposite sign as the remaining muon, to mimic the
 1176 selection in the signal region of the analysis for W+jets events. The steps to produce the ersatz
 1177 W+jets sample are:

- 1178 (i) Boost the two muons to the Z boson rest frame. The boost corresponds to the vector (-
 1179 $p_X^{\mu_1+\mu_2}, -p_Y^{\mu_1+\mu_2}, -p_Z^{\mu_1+\mu_2})/E^{\mu_1+\mu_2}$), where $E^{\mu_1+\mu_2} = \sqrt{(p_X^{\mu_1+\mu_2})^2 + (p_Y^{\mu_1+\mu_2})^2 + (p_Z^{\mu_1+\mu_2})^2 + (M^{\mu_1+\mu_2})^2}$.
 1180 (ii) Scale the muon four-vectors by the ratio of the W boson and Z boson masses, m_W/m_Z .
 1181 (iii) Boost back the two muons to keep the same total p_T as before, but with the W boson
 1182 mass. The boost corresponds to the vector $(p_X^{\mu_1+\mu_2}, p_Y^{\mu_1+\mu_2}, p_Z^{\mu_1+\mu_2})/E_2^{\mu_1+\mu_2}$, where $E_2^{\mu_1+\mu_2}$
 1183 is the same as in point (i) except that the mass in the last term has been replaced by the
 1184 new mass after scaling the muons by the ratio of the W and Z bosons mass.
 1185 (iv) The muon chosen previously is removed from the event and its transverse momentum is
 1186 added vectorially to the transverse missing energy.

1187 The exact same procedure is followed to produce an ersatz MC sample from a DY+jets MC
 1188 simulation. The distributions of the transverse mass between the remaining muon and the MET
 1189 in ersatz data and MC simulation are shown in Fig. 69 for the different categories of the analysis
 1190 and for an inclusive selection without any condition on the number of jets. Good data/MC
 1191 agreement is seen, and the high to low m_T ratios are comparable in both cases. A small non
 1192 closure is seen in the 0 jet category; it can likely be solved by applying recoil corrections to
 1193 the MET obtained in MC simulation. Based on these results, 10%, 5%, and 10% uncertainty
 1194 are considered in the 0 jet, boosted, and VBF categories, respectively. The uncertainty in the
 1195 0 jet category is driven by the non closure, whereas for the other categories it is driven by the
 1196 statistical uncertainty.

1197 The uncertainties are applied as normalization uncertainties to the W+jets background. They
 1198 are also propagated as a shape uncertainty in the QCD background. Indeed the W+jets back-
 1199 ground is subtracted from data in the SS isolated region to estimate the QCD contribution in the
 1200 signal region. Therefore, in the $e\tau_h$ and $\mu\tau_h$ final states, the uncertainty in the W+jets data/MC
 1201 scale factor has an impact both on the W+jets (normalization only), and on the QCD (shape and
 1202 normalization effect).

1203 There is no evidence for a dependence of the W+jets scale factor on the fitting variables, namely
 1204 the di-tau mass, the invariant mass of the jets, the Higgs boson p_T , or the tau decay mode. The
 1205 uncertainties are thus applied as flat over an entire category. Figure 70 illustrates the measured
 1206 data/MC scale factors for the individual categories, as well as for some particular slices of the
 1207 fitting parameters. No trend can be seen as a function of these parameters, and the scale factors
 1208 are compatible with the scale factors per category within the uncertainties. The slices of the
 1209 fitting parameters are close but not exactly the same as those used in the analysis because some
 1210 slices are too poorly populated to measure the scale factor in the high- m_T region. The scale
 1211 factors in slices have also been computed with a relaxed τ_h isolation and a looser m_T cut to
 1212 reduce the statistical uncertainties: the conclusion remains the same, and the scale factors in
 1213 the last Higgs p_T and m_{jj} slices get closer to the central values of the scale factors.

1214 11.4 QCD estimation

- 1215 In the $e\tau_h$ and $\mu\tau_h$ channels, the QCD multijet background is estimated from a SS region. An OS
 1216 to SS scale factor is measured in anti-isolated control regions. The uncertainty on the OS/SS
 1217 scale factor is taken into account by the fit of the anti-isolated control regions. Additionally
 1218 20% uncertainty, separated by channels, is considered to account for the extrapolation between
 1219 anti-isolated (control region) to isolated (signal region) taus; this uncertainty amounts to 20%.
 1220 In the $\tau_h\tau_h$ final state, the method to estimate the QCD background is different, and is described
 1221 in details in the corresponding section. The associated uncertainty ranges between 3% and 15%.

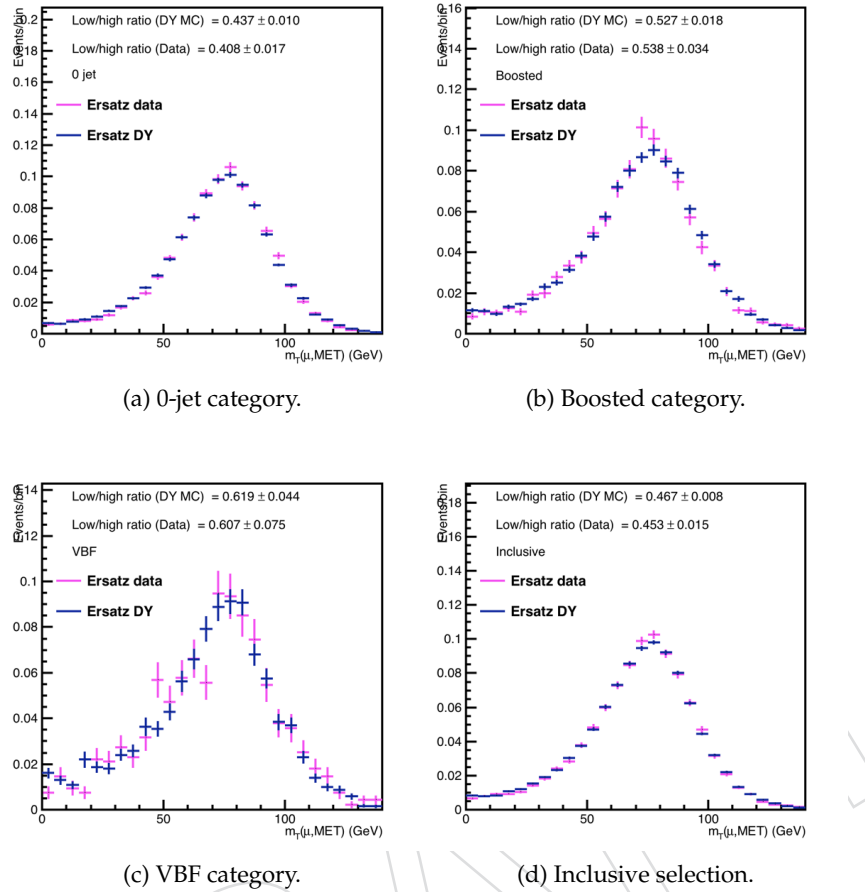


Figure 69: Comparison of the transverse mass distributions between ersatz $W \rightarrow \mu\nu$ events in data and in MC.

In the $e\mu$ final state, the uncertainty in the OS to SS scale factor is between 10 and 20% depending on the category.

11.5 $t\bar{t}$ estimation

The $t\bar{t}$ background is estimated from MC samples. The data/MC agreement can be checked in a signal-free region enriched in $t\bar{t}$ events, defined by the basic selection in the $e\mu$ final state, except that the P_ζ cut is inverted ($P_\zeta < -35$ GeV). In addition, the invariant mass of the muon and the electron is required to be greater than 90 GeV to reject Drell-Yan events. The data/MC agreement is checked in each category, and in each slice of the second fitting variable (not the mass). As shown in Fig 71, there is no evidence of different trends depending on the slice of the 2D distributions.

A control region for the $t\bar{t}$ background is created in a single-bin distribution with all $e\mu$ events with $P_\zeta < -35$ GeV and at least one jet with $p_T > 30$ GeV. The purity reaches about 85%. The control region is added to the final fit in order to constrain the $t\bar{t}$ background, as described in Section 10.

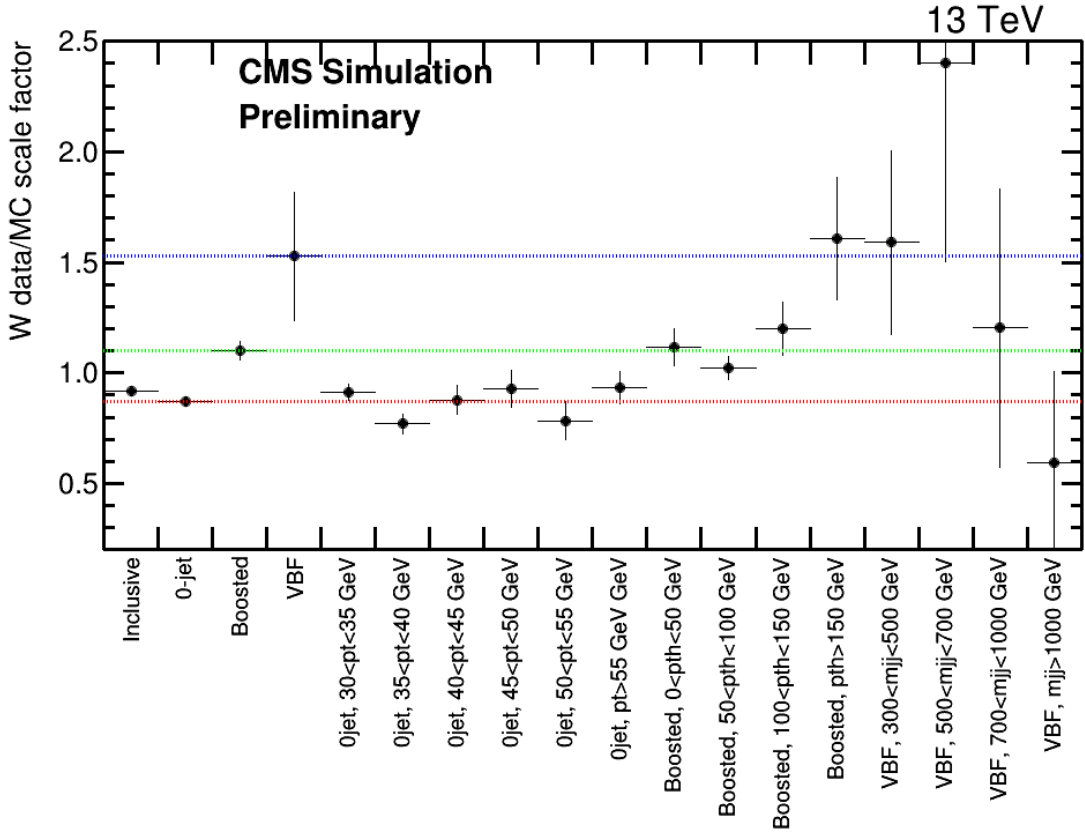


Figure 70: $W+jets$ data/MC scale factor measured in the $\mu\tau_h$ final state, for all events, for the individual categories, and for particular slices of the fitting parameters. The colored lines correspond to the scale factors measured in individual categories.

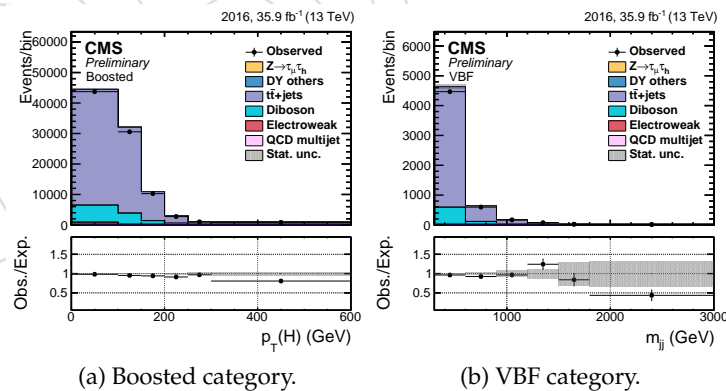


Figure 71: Control regions for the $t\bar{t}$ background obtained by inverting the P_ζ cut in the $e\mu$ final state. Plots are prefit, and only the statistical uncertainty is shown. There is no evidence for a different behavior with the Higgs p_T or m_{jj} in the boosted or VBF categories respectively.

1236 **11.6 Other MC normalization**

1237 The uncertainty on the single top background, estimated purely from MC samples, amounts to
 1238 5%. 5% uncertainty is also considered for the various diboson processes.

1239 **11.7 Fake rates**

1240 **11.7.1 $\mu \rightarrow \tau_h$ fake rate**

1241 Also described in section 4.3. The probability of a μ to fake a τ_h is measured in a dedicated
 1242 tag and probe study using $Z \rightarrow \mu\mu$ events which are reconstructed as $Z \rightarrow \mu\tau_h$. For different
 1243 working points of the anti-muon discriminator (Loose, Medium, Tight), events are split into
 1244 pass and fail categories and fit simultaneously between the pass and fail regions to extract a
 1245 data to mc scale factor and uncertainty for events with a generator matched μ which fakes a τ_h
 1246 in bins of η . In practice the scale factors are applied as a function of the pseudorapidity of the
 1247 muon that fakes the hadronic tau. A flat 25% uncertainty is considered on processes where a
 1248 muon fakes a hadronic tau (mostly $Z \rightarrow \mu\mu$ in the $\mu\tau_h$ final state). It is uncorrelated between
 1249 tau decay modes.

1250 **11.7.2 $e \rightarrow \tau_h$ fake rate**

1251 The probability of an electron to fake a τ_h is measured in a dedicated tag and probe study
 1252 using $Z \rightarrow ee$ events which are reconstructed as $Z \rightarrow e\tau_h$. For different working points of
 1253 the anti-electron discriminator (Very Loose, Loose, Medium, Tight, Very Tight), events are split
 1254 into pass and fail categories and fit simultaneously between the pass and fail regions to extract
 1255 a data to mc scale factor and uncertainty for events with a generator matched electron which
 1256 fakes a τ_h in bins of η . A flat 12% uncertainty is considered on processes where an electron
 1257 fakes a hadronic tau,(mostly $Z \rightarrow ee$ in the $e\tau_h$ final state). It is fully uncorrelated between tau
 1258 decay modes.

1259 **11.7.3 $j \rightarrow \tau_h$ fake rate**

1260 The uncertainty in data/MC scale factor for the probability for a jet to fake a hadronic tau
 1261 depends on the p_T of the jet associated to the fake τ_h . The uncertainty amounts to $20\% \times$ jet
 1262 $p_T/100$ GeV. Because of a lack of statistics, the correction for all events with $p_T > 200$ GeV is
 1263 taken as 40%. It is applied as a shape uncertainty to processes with a jet faking a hadronic tau,
 1264 for example to W+jets in the $\tau_h\tau_h$ final state, or $t\bar{t}$ with hadronic decays in the $e\tau_h$, $\mu\tau_h$ and $\tau_h\tau_h$
 1265 final states. This also brings a shape uncertainty to the W+jets background in the $e\tau_h$, $\mu\tau_h$ final
 1266 states. The normalization of the alternative shapes for the W+jets backgrounds is fixed to the
 1267 one of the nominal sample because the MC sample is used only to describe the shape of the
 1268 background whereas the nornalization is data-driven, based on the high- m_T control regions.

1269 **11.8 Energy scales**

1270 **11.8.1 τ_h energy scale**

1271 As described previously, the nominal τ_h energy scale is corrected based on the decay mode:
 1272 -1.8% for 1 prong taus, +1.0% for 1 prong + 1 π^0 , and +0.4% for 3 prong taus. These corrections
 1273 come from a measurement within the TAU POG, made in $Z \rightarrow \mu\tau_h$ events and based on a
 1274 fit to the visible mass distributions. The uncertainty on the correction ranges from 0.4 to 0.6%,
 1275 depending on the decay mode. For simplicity, a general 0.6% uncertainty is considered for each
 1276 decay mode, fully uncorrelated from the other decay modes. The τ_h energy scale uncertainty
 1277 is expected to be constrained by this analysis because we combine different final states (only

1278 $\mu\tau_h$ considered in the TAU POG measurement), take a slightly conservative number (0.6% for
1279 all decay modes), and have categories sensitive to event migrations caused by tau energy scale
1280 variations.

1281 The τ_h energy scale uncertainty is applied by shifting the τ_h four-vectors up and down 0.6%,
1282 recomputing composite variables in the analysis. The change in shape of final fitted variables
1283 is then included as a shape systematic uncertainty. For one prong taus the mass is set constant
1284 to the pion mass for all shifts.

1285 11.8.2 Fake τ_h energy scale

1286 A shape uncertainty is considered on the energy scale of electrons and muons misidentified as
1287 hadronic taus in the $e\tau_h$ and $\mu\tau_h$ final states. The uncertainty amount to 3%, is uncorrelated
1288 between muons and electrons, and is propagated to the SV mass calculation.

1289 As described previously the position of the $Z \rightarrow ee$ and $Z \rightarrow \mu\mu$ peaks in the $e\tau_h$ and $\mu\tau_h$
1290 channels respectively, is shifted to match the data. The uncertainty on the correction is between
1291 0.3 and 0.5%, and is uncorrelated between various reconstructed tau decay modes.

1292 11.8.3 Electron energy scale

1293 This should be applied for the $e\mu$ channel, where it is propagated through the SVmass calcula-
1294 tion. 1% in the barrel and 2.5% in the endcaps are considered for the energy scale shifts. This
1295 uncertainty is negligible compared to the τ_h energy scale in the $e\tau_h$ channel.

1296 11.8.4 Jet energy scale

1297 The recommended JetMEt POG corrections are used to shift the jets four-momenta within their
1298 uncertainties. The shape is computed by shifting the P_T of every jet in the event and then
1299 recomputing m_{jj} . The jet energy scale shape uncertainty is essential in the VBF category, where
1300 the $M_{\tau\tau}$ is unrolled in m_{jj} , a jet dependent variable. Events may shift between categories when
1301 a jet p_T is shifted up or down near 30 GeV.

1302 There exist 27 independent sources of jet energy scale uncertainty [?]:

- 1303 • Absolute[Stat][MPFBias][FlavMap][Scale] : flat absolute scale uncertainties. Mainly
1304 uncertainty in combined photon (EM) and $Z \rightarrow \mu\mu$ (tracking) reference scale and
1305 correction for FSR+ISR.
- 1306 • Fragmentation : high p_T extrapolation. Based on Pythia6 Z2/Herwig++2.3 differ-
1307 ences in fragmentation and underlying event (FullSim).
- 1308 • SinglePionHCAL : high p_T extrapolation. Based on propagation of +/-7% variation
1309 in single particle response in HCAL to PF Jets (FastSim).
- 1310 • SinglePionECAL : high p_T extrapolation. Based on propagation of +/-4% variation
1311 in single particle response (in ECAL/HCAL) to PF Jets (FastSim).
- 1312 • Flavor[QCD] : jet flavor. Based on Pythia6 Z2/Herwig++2.3 differences in uds/c/b-
1313 quark and gluon responses.
- 1314 • Time[Pt][Eta] : JEC time dependence. Observed instability in the endcap (barrel)
1315 region, presumed to be due to the HE/HF radiation damage, and possibly also due
1316 to ECAL transparency loss.
- 1317 • RelativeJER[EC1][EC2][HF] : eta-dependence uncertainty from jet p_T resolution (JER).
1318 The JER uncertainties are assumed fully correlated for endcap within tracking (EC1),
1319 endcap outside tracking (EC2) and hadronic forward (HF).

- RelativeFSR : η -dependence uncertainty due to correction for final state radiation. Uncertainty increases toward HF, but is correlated from one region to the other.
- RelativePt[BB][EC1][EC2][HF]: residual log-linear p_T dependence relative to the central fit (constant in BB, HF, log-linear in EC1, EC2 possibly due to radiation damage).
- RelativeStat[EC2][HF] : statistical uncertainty in determination of eta-dependence. Fixed uncertainty over wider detector regions. Only important in endcap outside tracking (EC2) and in HF.
- PileUpDataMC: taking 20% of data/MC difference observed in the data-based Random Cone method in Zero Bias data (RCZB) as uncertainty.
- PileUpPt[Ref][BB][EC][HF]: pile-up offset dependence on jet p_T is estimated from matched MC with and without PU overlay. The uncertainty is taken as difference to Random Cone method (i.e. essentially difference of PU inside and outside of jets), propagated through L2 and L3 data-driven methods.
- RelativeBal: to account for disagreement between central MPF and p_T balance methods. It is sizeable at high η .

Some of these uncertainties are specific to some particular regions of the detector only. To avoid that jets in a given region constrain other independent jets, we consider the 27 sources of JES uncertainty as fully uncorrelated in the analysis. Alternative distributions obtained by varying the individual sources are added for each process to the final fit.

The sensitivity of the analysis slightly decreases by uncorrelating the 27 sources of uncertainty because jets are less constrained than when there is only one jet energy scale uncertainty. Some of the individual sources of jet energy scale uncertainty still get constrained by the fit to the three analysis categories in the four final states, but the constraints are less important. In particular the "RelativeBal" uncertainty is constrained, with a relatively large impact on the analysis; this is expected because the uncertainty mostly affects high- η jets in the VBF category, and is overestimated because it accounts for a non closure between two measurements.

The effect of the total jet energy scale shifts (combination of the 27 sources) on the $Z \rightarrow \tau\tau$ background and on the signal, in the $\tau_h\tau_h$ final state, is shown for the boosted and VBF categories in Fig. 72.

11.8.5 MET energy scale

In the $e\mu$ final state, the MET plays a role via the P_ζ cut, which is used to reduce the contribution of $t\bar{t}$ and diboson events. The effect of the MET unclustered energy uncertainty on the yields of the different processes is evaluated by shifting the MET within its uncertainties and recomputing the acceptance. The total effect is of the order of 1% for all processes and categories. There is no trend with any of the fitting variables, and the uncertainty is considered as flat.

In the $\mu\tau_h$ and $e\tau_h$ final states, the MET is used to compute the transverse mass, which is required to be less than 50 GeV in all categories. The effect of the MET systematics is propagated to the yields: the uncertainty in the yield can go up to 2.5% in the 0-jet category. The changes in acceptance are given in Tab 26. Again no trend is seen as a function of the fitting variables.

In the $\tau_h\tau_h$ final state, the MET is not used directly in any of the selection criteria. However, as in the case of the other final states, it is one of the ingredients needed to compute the Higgs p_T . In the analysis, the Higgs p_T is computed with the SVfit algorithm, which computes the most likely full four-vectors of the taus. In the process, the MET is adjusted as far as the covariance matrix allows, so that it is likely that slightly different MET values would be adjusted towards

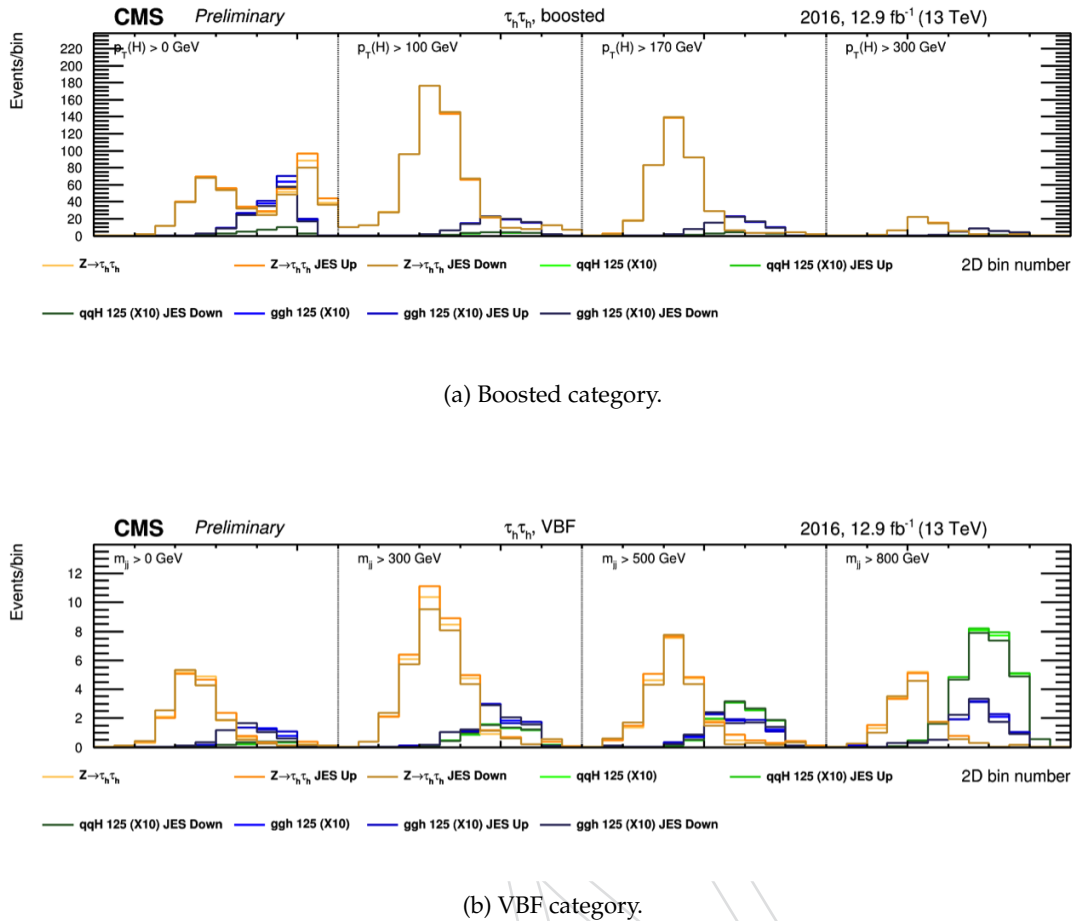


Figure 72: Effect of jet energy scale shifts on background and signal templates in the $\tau_h \tau_h$ final state.

	0-jet	VBF	Boosted
$\mu \tau_h$	-2.2 / +1.2%	-1.5 / +0.6%	-2.4 / +0.7%
$e \tau_h$	-2.6 / +1.8%	-1.1 / +0.5%	-0.1 / +0.2%

Table 26: Variation of the total background acceptance by varying the MET within its uncertainties and propagating it to the transverse mass, in the $\mu \tau_h$ and $e \tau_h$ final states.

the same most probable value. We have checked the effect that the MET uncertainties would have if the Higgs p_T was computed by vectorially summing the visible four-vectors of the taus and the MET vector, which is a very conservative situation. As expected the variation of the templates over the Higgs p_T spectrum is not flat (migration between bins), but the total variation does not exceed a few percents (of the order of 1% for most processes), which is negligible compared to other shape and normalization uncertainties already considered in the analysis.

11.9 Z+jets reweighting

The shape uncertainty of the Drell-Yan background is computed by applying 0.9 or 1.1 times the correction. It is fully correlated between channels and categories.

1374 **11.10 Btagging uncertainty**

1375 A btag veto is applied in the $e\mu$ channel. The btagging uncertainty for $t\bar{t}$ events in the 0 jet,
 1376 boosted, and VBF categories, is respectively 3.5, 5, and 5%. This is computed by propagating
 1377 the uncertainty on the scale factors for heavy flavor jets through all steps of the analysis. The
 1378 mistagging uncertainty for the diboson background is 1.5% in the boosted and VBF categories.
 1379 The uncertainty for other processes, including signal, is negligible.

1380 **11.11 Z+jets estimation uncertainty**

1381 Data/MC scale factors are derived for the Z+jets background based on a $Z \rightarrow \mu\mu$ enriched
 1382 region. Uncertainties to account for the extrapolation to the $Z \rightarrow \tau\tau$ kinematics are taken into
 1383 account. In the 0-jet category, 8% difference is seen between the data/MC scale factor measured
 1384 when selecting muons with p_T greater than 25 or 50 GeV. This is included as a yield systematic
 1385 in this category. It is split into a correlated uncertainty between final states, and an uncorrelated
 1386 uncertainty. In the boosted category the scale factors remain close when changing the muon p_T
 1387 thresholds, and a flat 3% uncertainty, split into a correlated and an uncorrelated component,
 1388 is considered. In the VBF category the data/MC disagreement seen with 25 GeV as threshold
 1389 disappears with higher p_T thresholds. Half of the weights with 25 GeV threshold are applied as
 1390 scale factors, whereas a shape uncertainty, for which the alternative 1σ distribution correspond
 1391 to no correction and the full 25 GeV scale factors, is added to the uncertainty model.

1392 **11.12 $t\bar{t}$ reweighting according to generated top/antitop p_T**

1393 The $t\bar{t}$ background is reweighted according to the generated transverse momentum of the top
 1394 quarks, as explained earlier. A shape uncertainty, corresponding to the size of the correction, is
 1395 applied to the background, and considered as fully correlated between the different final states.

1396 **11.13 Theoretical uncertainties for signal**

1397 A dedicated AN (AN-16-387) details theoretical uncertainties for the gluon-gluon fusion and
 1398 vector boson fusion processes. In this analysis the renormalization scale uncertainty is consid-
 1399 ered as a shape uncertainty, as the uncertainty can be parameterized linearly as a function of
 1400 the Higgs p_T and m_{jj} in the boosted and VBF categories respectively. This is illustrated in Fig 73,
 1401 for the $\mu\tau_h$ final state.

1402 Various sources of theoretical uncertainties are included in this analysis:

- 1403 • Uncertainty on $H \rightarrow \tau\tau$ branching fraction, composed of three independent sources
 1404 of uncertainties.
- 1405 • Uncertainty on cross section based on YR4, composed of three independent sources
 1406 of uncertainties.
- 1407 • Uncertainty on acceptance due to renormalization and factorization scales: consid-
 1408 ered as a shape uncertainty as explained in the previous paragraph.
- 1409 • Uncertainty on acceptance due to the parton shower tune.
- 1410 • Uncertainty on acceptance by comparing Powheg (default) and aMC@NLO signal
 1411 samples. Up to 20% for the ggH process, and up to 10% for the qqH process.
- 1412 • Uncertainty on acceptance due to α_S : less than 1%.

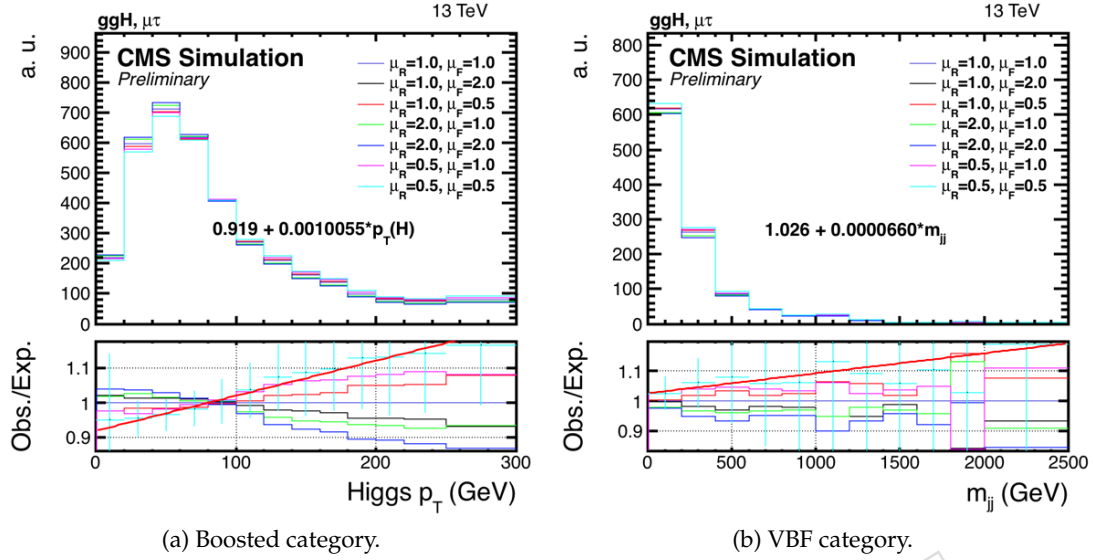


Figure 73: Parameterization of the renormalization/factorization scale uncertainties for the gluon-gluon fusion signal in the $\mu\tau_h$ final state.

11.14 Systematic uncertainties summary

The uncertainties considered in the analysis are the following. The names in parenthesis are those used in Combine, and also present in the impact plots in the next section.

- Electron ID and isolation efficiency (CMS_eff_e):** Applied to simulated processes with electrons, 2% on the yield.
- Muon ID and isolation efficiency (CMS_eff_m):** Applied to simulated processes with muons, 2% on the yield.
- Trigger efficiency (CMS_eff_trigger_*):** 2% uncorrelated between $e\mu$, $e\tau_h$, $\mu\tau_h$. For $\tau_h\tau_h$ it is counted together with the tau ID efficiency uncertainty.
- Tau ID efficiency (CMS_eff_t_*):** Applied to simulated events with reconstructed taus matched to hadronic taus at generated level. 5% per tau, composed from 4% correlated between final states, and 3% uncorrelated between final state. The uncorrelated part in the $\tau_h\tau_h$ final state also includes the trigger efficiency (3.5% per tau).
- Tau decay mode distribution (CMS_tauDMReco_*):** Applied to simulated events with reconstructed taus matched to hadronic taus at generated level, in the 0 jet category of $e\tau_h$ and $\mu\tau_h$. It allows for variations by 3% of the reconstruction/ID efficiency per decay mode, while preserving the overall normalization.
- $e \rightarrow \tau_h$ fake rate (CMS_eFakeTau_*):** uncertainty in the $e \rightarrow \tau_h$ scale factors. 12% for $Z \rightarrow ee$ in the $e\tau_h$ final state, fully uncorrelated between tau decay mode.
- $\mu \rightarrow \tau_h$ fake rate (CMS_mFakeTau_*):** uncertainty in the $\mu \rightarrow \tau_h$ scale factors. 25% for $Z \rightarrow \mu\mu$ in the $\mu\tau_h$ final state, fully uncorrelated between tau decay mode.
- jet $\rightarrow \tau_h$ fake rate (CMS_htt_jetToTauFake):** Shape uncertainty for backgrounds with a hadronic tau matched to a jet at reconstructed level. 20% uncertainty per slice

of 100 GeV in τ_h p_T . This uncertainty also affects the yield, except for the W+jets background where the shapes are normalized to the nominal distribution because the normalization is extracted from data.

- **τ_h energy scale (CMS_scale_t_*)**: 0.6% for taus matched to hadronic taus at generated level. Fully uncorrelated per decay mode, and fully correlated between channels and categories.
- **Electron energy scale (CMS_scale_e_em)**: 1% in the barrel and 2.5% in the endcaps, for simulated processes in the $e\mu$ channel. Neglected in the $e\tau_h$ final state.
- **Jet energy scale (CMS_scale_j_*)**: 27 sources of JES propagated independently to the number of jets and m_{jj} for all simulated processes .
- **MET energy scale (CMS_htt_scale_met)**: Unclustered MET uncertainty propagated as a yield uncertainty in all final states.
- **$Z \rightarrow ee/\mu\mu$ peak position (CMS_ZLShape_*)**: Uncertainty on the correction applied to the visible mass peak of the ZL background in the 0 jet category of the $e\tau_h$ and $\mu\tau_h$ channels. It is uncorrelated between decay modes. The uncertainty is between 0.3 and 0.5%.
- **Luminosity (lumi_13TeV)**: 2.6%.
- **Btagging and mistagging efficiencies (CMS_htt_eff_b, CMS_htt_mistag_b)**: related to the bjet veto, up to 5% for $t\bar{t}$ in the $e\mu$ channel and in the $t\bar{t}$ control region.
- **Top p_T reweighting (CMS_htt_ttbarShape)**: Uncertainty between no and twice the correction on the reweighting, applied to $t\bar{t}$ events in all channels.
- **Drell-Yan MC reweighting (CMS_htt_dyShape)**: Uncertainty between 0.9 and 1.1 times the correction of the DY MC sample that depends on the generated Z boson p_T and mass. Applied as a shape uncertainty, with a yield effect too.
- **Drell-Yan estimation (CMS_htt_zmm_norm_extrap_*)**: Yield uncertainties for the Drell-Yan MC sample, uncorrelated between final states and categories, based on the data/MC agreement observed in $Z \rightarrow \mu\mu$ events, and on the variations of the data/MC ratio by varying the muon p_T threshold used to select events in the $\mu\mu$ region. It ranges between 7 and 20%, depending on the category and final state.
- **Drell-Yan description in VBF (CMS_htt_zmumuShape_*)**: Shape only uncertainty on the Drell-Yan template in the VBF category, extracted from the $Z \rightarrow \mu\mu$ region. Uncorrelated between channels. It does not change the overall normalization, but the contribution to individual m_{jj} slices.
- **QCD estimation in the $\tau_h\tau_h$ final state (CMS_htt_QCD_*.tt)**: Yield uncertainty between 3 and 15%, uncorrelated between categories.
- **QCD estimation in the $e\mu$ final state (CMS_htt_QCD_*.em)**: Yield uncertainty between 10 and 20%, uncorrelated between categories.
- **QCD extrapolation between anti-isolated and isolated regions (QCD_Extrap_Iso_nonIso_*)**: in the $e\tau_h$ and $\mu\tau_h$ channels, extrapolation uncertainty from the anti-isolated control region to the signal region, 20% on the yield.
- **Effect of W estimation on QCD shape (WSFUncert_*)**: Propagation of the W+jets uncertainty on the W subtracted from data in the SS region to estimate the QCD. Considered as a shape uncertainty only.
- **W+jets high to low m_T extrapolation (WHighMTToLowMT_*)**: Up to 10%, uncorrelated between channels and categories.

- **W+jets cross section (CMS_htt_wjXsec):** 4% in $e\mu$ and $\tau_h\tau_h$.
- **Diboson and single top cross sections (CMS_htt_vvXsec):** 6%.
- **Signal cross section from PDF and α_S uncertainties (pdf_Higgs_*):** PDF and α_S uncertainties on signal cross section, from YR4. 3.2% for ggH, 2.1% for qqH, 1.9% for WH, 1.6% for ZH.
- **Signal acceptance from α_S uncertainties (CMS_*.PDF):** α_S uncertainties on signal acceptance. Up to 0.9%.
- **Signal acceptance from PDF uncertainty (CMS_scale_gg):** renormalization and factorization scale uncertainties on signal acceptance. Considered as a shape uncertainty, with a dependence on the lepton p_T , Higgs p_T , and m_{jj} . **Parton shower scale variation on signal cross acceptance (CMS_*.UEPS):** Uncertainty on the signal acceptance relates to different parton shower scales. Up to 5%, in the boosted category.
- **MC comparison for signal (CMS_*.mcComp):** Theoretical uncertainty for the signal, based on different acceptances observed with Powheg and aMC@NLO MC samples.
- **Renormalization and factorization scales (QCDscale_*):** Theoretical uncertainty on the signal acceptance due to variations of the renormalization and factorization scales.
- **$H \rightarrow \tau\tau$ branching fraction (BR_htt_THU, BR_htt_PU_mq, BR_htt_PU_alphas):** Theoretical uncertainty in $H \rightarrow \tau\tau$ branching fraction. 1.7, 0.99, 0.62% respectively.
- **$H \rightarrow WW$ branching fraction (BR_hww_THU, BR_hww_PU_mq, BR_hww_PU_alphas):** Theoretical uncertainty in $H \rightarrow WW$ branching fraction.

12 Results

1504 The search for an excess of SM Higgs boson events over the expected background involves a
 1505 global maximum likelihood fit based on two-dimensional distribution in all channels.

1507 The distributions of the final discriminating variable obtained for each category and each channel
 1508 as two-dimensional distributions ($p_T, mass$) are combined in a binned likelihood, involving
 1509 the expected and observed numbers of events in each bin. The expected number of signal
 1510 events is the one predicted by the SM for the production of a Higgs boson of mass H decaying
 1511 into a pair of τ leptons, multiplied by a signal strength modifier μ treated as free parameter in
 1512 the fit.

1513 The mass distributions per category and channel have been shown in the previous sections
 1514 of this note. From these distributions, we fill a histogram based on the ratio of the signal to
 1515 signal-plus-background in each bin of the distributions. The most sensitive bins of the analysis
 1516 have $-0.4 < \log(S/S + B) < 0.2$, and belong mostly to the $\tau_h\tau_h$ distributions. This is shown in
 1517 Fig. 74.

1518 The systematic uncertainties are represented by nuisance parameters that are varied in the
 1519 fit according to their probability density function. A log-normal probability density function
 1520 is assumed for the nuisance parameters affecting the event yields of the various background
 1521 contributions, whereas systematic uncertainties that affect the distributions are represented by
 1522 nuisance parameters whose variation results in a continuous perturbation of the spectrum [?]
 1523 and which are assumed to have a Gaussian probability density function. Overall, the statistical
 1524 uncertainty in the observed event yields is the dominant source of uncertainty for all combined

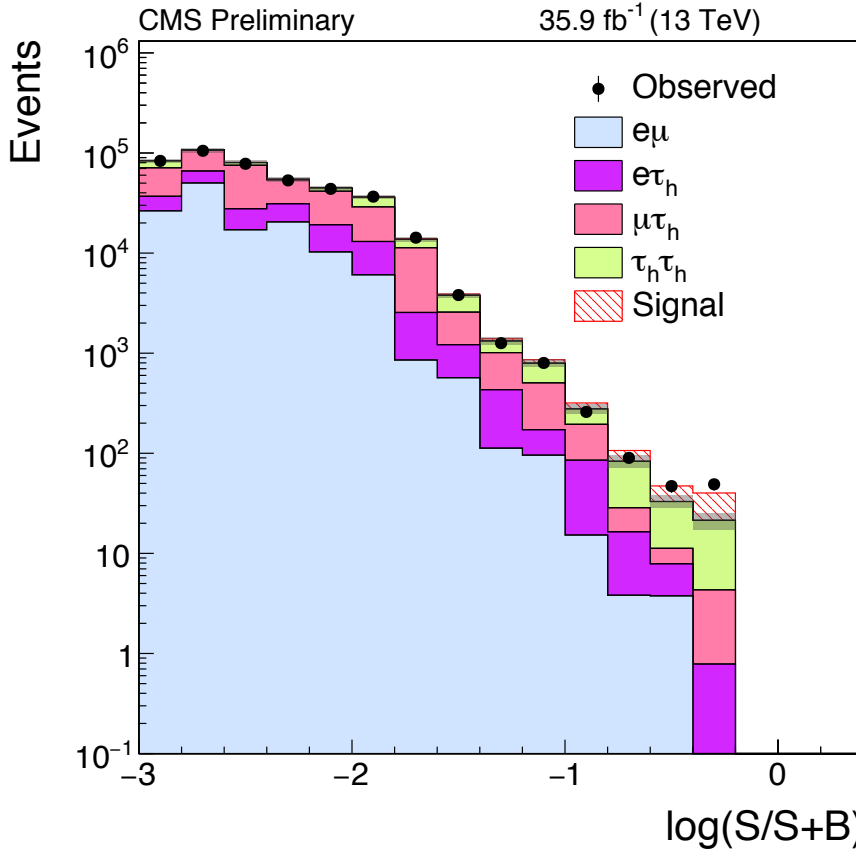


Figure 74: Distribution of the ratio between the expected signal and the sum of expected signal and expected background in each bin of the mass distributions used to extract the results, in all channels.

1525 results.

1526 The systematic model is tested by computing the impacts of the nuisance parameters, as well as
 1527 the constraints on the nuisance parameters, based on an Asimov dataset. The results are given,
 1528 for non bin-by-bin uncertainties, in Figs. 75-78. Theoretical uncertainties on the signal yield
 1529 have major impacts on the signal strength. Uncertainties in the tau ID efficiency, tau energy
 1530 scale, and jet $\rightarrow e/\mu$ energy scales, are expected to be constrained with respect to recommenda-
 1531 tions by TAU POG (which cover also non closures of measurements with different methods).
 1532 The jet energy scale gets constrained by the fit on m_{jj} in the VBF category, and by the migration
 1533 of events between categories.

1534 An excess in data is quantified by calculating the corresponding local p -values using a profile-
 1535 likelihood ratio test statistics [37, 38]. The expected significance for a Higgs boson with a mass
 1536 of 125 GeV is equal to 4.9 standard deviations. The corresponding observed significance is 4.9
 1537 standard deviations.

1538 Upper limits at 95% CL are set on the signal strength using the modified frequentist construc-
 1539 tion CL_s [39, 40]. The observed limit for $H = 125$ GeV is equal to 1.5, for an expected limit of
 1540 0.4. The background-only hypothesis includes the expected contribution from ww decays for
 1541 $H = 125$ GeV. The decomposition of the expected upper limits in the different final states, as
 1542 well as the combined upper limit on the signal strength together with its one- and two-standard
 1543 deviations uncertainty bands, are shown in Fig. 79. The most sensitive final state is $\tau_h\tau_h$, which

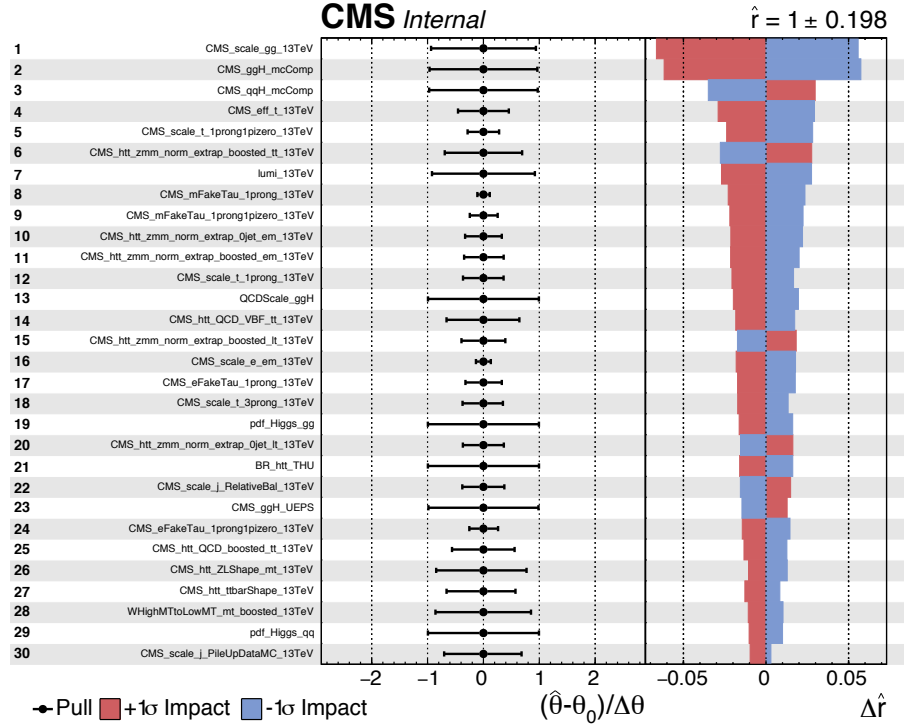


Figure 75: Impact of nuisance parameters on the signal strength, based on an Asimov dataset (part 1).

1544 has the largest branching fraction of all di-tau final states. It is closely followed by $\mu\tau_h$, which,
 1545 despite a branching fraction about twice as low, benefits from lower trigger threshold and from
 1546 a cleaner environment. The $e\tau_h$ final state is slightly less sensitive than $\mu\tau_h$ because of higher
 1547 trigger thresholds, and less efficient electron identification for a similar fake rate. The least sen-
 1548 sitive final state is $e\mu$, which suffers from a low branching fraction, as well as from a large $t\bar{t}$
 1549 background.

1550 The best-fit signal strength is 1.06 ± 0.25 . The combined and per channel μ -values are shown
 1551 in Fig. 80.

1552 13 Summary

1553 A search for the SM scalar boson based on data collected in pp collisions by the CMS detector
 1554 in 2016 at a center-of-mass energy of 13 TeV with a total integrated luminosity of 35.9 fb^{-1} ,
 1555 has been presented. The four di- τ final states, $e\tau_h$, $\mu\tau_h$, $\tau_h\tau_h$, $e\mu$, have been studied, in event
 1556 categories targeting Higgs boson signal events produced via gluon-gluon fusion and vector
 1557 boson fusion. The results are extracted via two-dimensional maximum likelihood fits in the
 1558 plans defined by the full or visible di- τ mass, and the lepton transverse momentum in the 0-
 1559 jet category, the invariant mass of the leading jets in the VBF category, and the Higgs boson
 1560 candidate transverse momentum in the boosted category. This leads to an evidence for the
 1561 decay of the SM Higgs boson to pairs of taus, with an observed significance of XXX standard
 1562 deviations for a mass of 125 GeV.

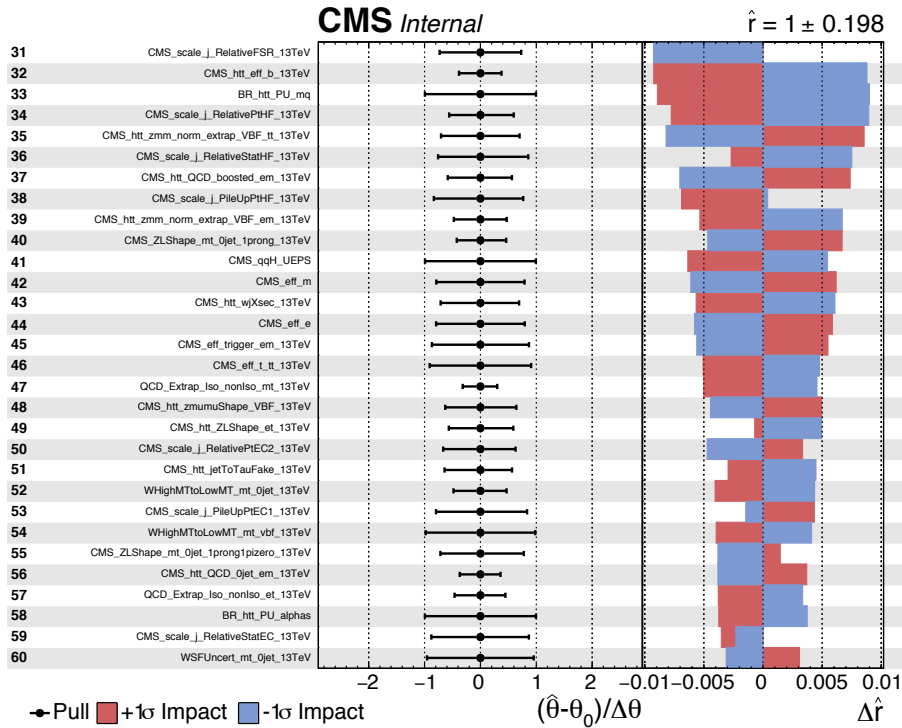


Figure 76: Impact of nuisance parameters on the signal strength, based on an Asimov dataset (part 2).

References

- [1] S. Weinberg, "A Model of Leptons", *Phys. Rev. Lett.* **19** (1967) 1264, doi:10.1103/PhysRevLett.19.1264.
- [2] A. Salam, "Weak and electromagnetic interactions", in *Elementary particle physics: relativistic groups and analyticity*, N. Svartholm, ed., p. 367. Almqvist & Wiksell, Stockholm, 1968. Proceedings of the eighth Nobel symposium.
- [3] F. Englert and R. Brout, "Broken Symmetry and the Mass of Gauge Vector Mesons", *Phys. Rev. Lett.* **13** (1964) 321, doi:10.1103/PhysRevLett.13.321.
- [4] P. W. Higgs, "Broken symmetries, massless particles and gauge fields", *Phys. Lett.* **12** (1964) 132, doi:10.1016/0031-9163(64)91136-9.
- [5] P. W. Higgs, "Broken Symmetries and the Masses of Gauge Bosons", *Phys. Rev. Lett.* **13** (1964) 508, doi:10.1103/PhysRevLett.13.508.
- [6] G. S. Guralnik, C. R. Hagen, and T. W. B. Kibble, "Global Conservation Laws and Massless Particles", *Phys. Rev. Lett.* **13** (1964) 585, doi:10.1103/PhysRevLett.13.585.
- [7] P. W. Higgs, "Spontaneous Symmetry Breakdown without Massless Bosons", *Phys. Rev.* **145** (1966) 1156, doi:10.1103/PhysRev.145.1156.
- [8] T. W. B. Kibble, "Symmetry Breaking in Non-Abelian Gauge Theories", *Phys. Rev.* **155** (1967) 1554, doi:10.1103/PhysRev.155.1554.

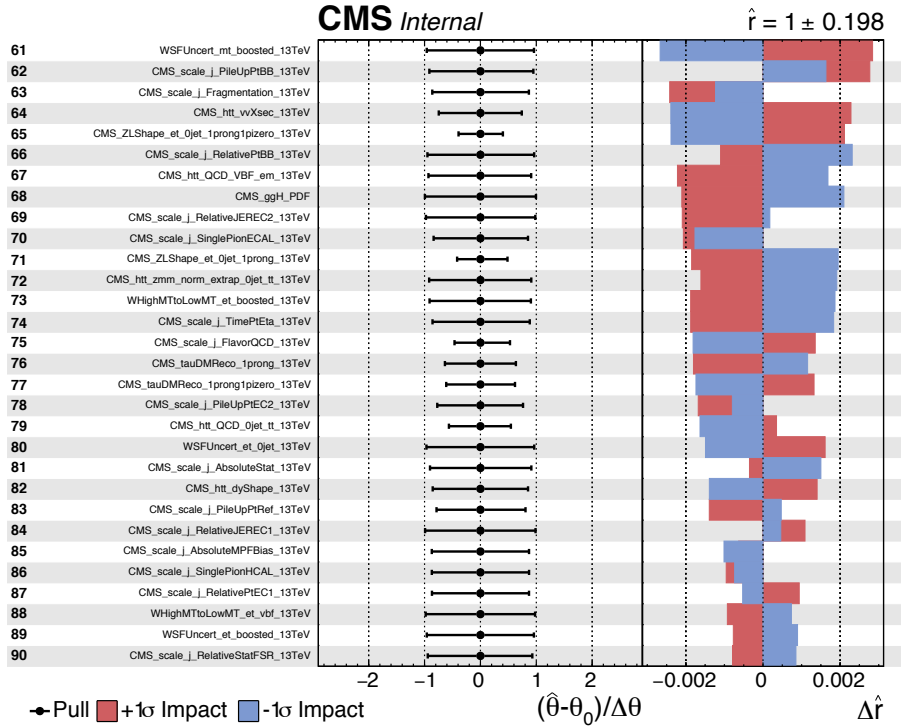


Figure 77: Impact of nuisance parameters on the signal strength, based on an Asimov dataset (part 3).

- [9] ATLAS Collaboration, “Observation of a new particle in the search for the Standard Model Higgs boson with the ATLAS detector at the LHC”, *Phys. Lett. B* **716** (2012) doi:10.1016/j.physletb.2012.08.020, arXiv:1207.7214.
- [10] CMS Collaboration, “Observation of a new boson at a mass of 125 GeV with the CMS experiment at the LHC”, *Phys. Lett. B* **716** (2012) doi:10.1016/j.physletb.2012.08.021, arXiv:1207.7235.
- [11] CMS Collaboration, “Observation of a new boson with mass near 125 GeV in pp collisions at $\sqrt{s} = 7$ and 8 TeV”, *JHEP* **06** (2013) 081, doi:10.1007/JHEP06(2013)081.
- [12] ALEPH Collaboration, “Observation of an excess in the search for the Standard Model Higgs boson at ALEPH”, *Phys. Lett. B* **495** (2000) 1, doi:10.1016/S0370-2693(00)01269-7, arXiv:hep-ex/0011045.
- [13] DELPHI Collaboration, “Final results from DELPHI on the searches for SM and MSSM neutral Higgs bosons”, *Eur. Phys. J. C* **32** (2004) 145, doi:10.1140/epjc/s2003-01394-x, arXiv:hep-ex/0303013.
- [14] L3 Collaboration, “Standard model Higgs boson with the L3 experiment at LEP”, *Phys. Lett. B* **517** (2001) 319, doi:10.1016/S0370-2693(01)01010-3, arXiv:hep-ex/0107054.
- [15] OPAL Collaboration, “Search for the Standard Model Higgs boson in e^+e^- collisions at $\sqrt{s} = 192\text{--}209$ GeV”, *Phys. Lett. B* **499** (2001) 38, doi:10.1016/S0370-2693(01)00070-3, arXiv:hep-ex/0101014.

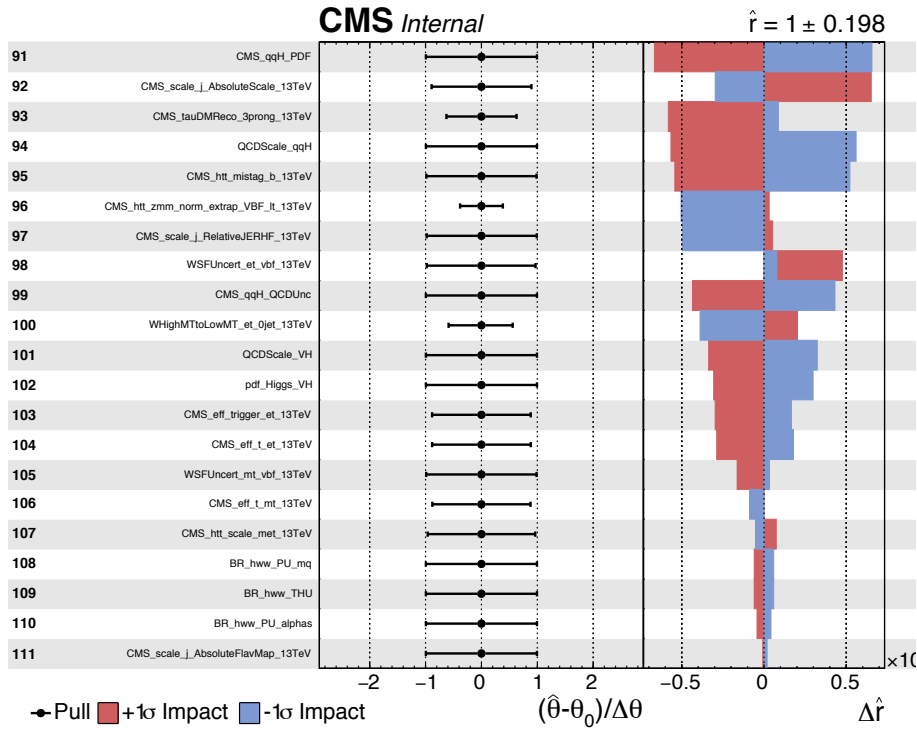


Figure 78: Impact of nuisance parameters on the signal strength, based on an Asimov dataset (part 4).....

- [16] ATLAS Collaboration, "Evidence for the Higgs-boson Yukawa coupling to tau leptons with the ATLAS detector", *JHEP* **04** (2015) 117, doi:10.1007/JHEP04(2015)117, arXiv:1501.04943.
- [17] CMS Collaboration, "Evidence for the 125 GeV Higgs boson decaying to a pair of τ leptons", *JHEP* **05** (2014) 104, doi:10.1007/JHEP05(2014)104, arXiv:1401.5041.
- [18] F. Maltoni and T. Stelzer, "MadEvent: Automatic event generation with MadGraph", *JHEP* **0302** (2003) 027, arXiv:0208.0156.
- [19] S. Frixione, P. Nason, and C. Oleari, "Matching NLO QCD computations with Parton Shower simulations: the POWHEG method", *JHEP* **0711** (2007) 070, arXiv:0709.2092.
- [20] T. Sjöstrand, S. Mrenna, and P. Z. Skands, "A Brief Introduction to PYTHIA 8.1", *Comput. Phys. Commun.* **178** (2008) 852, doi:10.1016/j.cpc.2008.01.036, arXiv:0710.3820.
- [21] CMS Collaboration, "Underlying Event Tunes and Double Parton Scattering", CMS Physics Analysis Summary CMS-PAS-GEN-14-001, 2014.
- [22] J. M. Campbell, R. K. Ellis, and C. Williams, "Vector boson pair production at the LHC", *JHEP* **1107** (2011) 018, doi:10.1007/JHEP07(2011)018, arXiv:1105.0020.
- [23] NNPDF Collaboration, "Parton distributions for the LHC Run II", *JHEP* **04** (2015) 040, doi:10.1007/JHEP04(2015)040, arXiv:1410.8849.

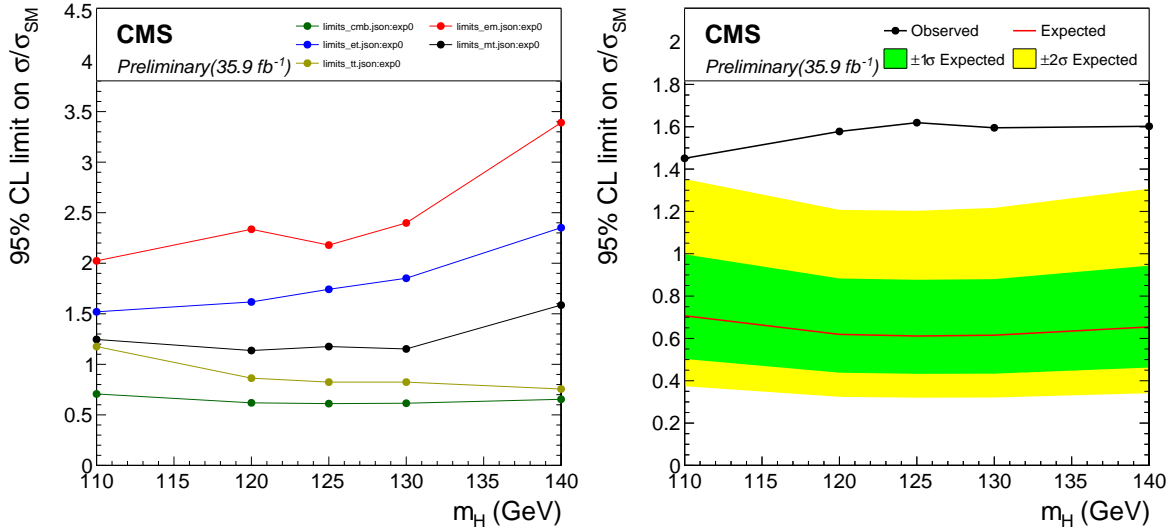


Figure 79: Left: Expected 95% CL upper limit on the signal strength parameter μ , for each final state, and for the combination of final states. Right: Combined expected 95% CL upper limit on the signal strength parameter μ , together with the expected limit obtained in the background-only hypothesis with its one- and two-standard deviation uncertainty bands.

- [24] CMS Collaboration, "Particle-Flow Event Reconstruction in CMS and Performance for Jets, Taus, and E_T^{miss} ", CMS Physics Analysis Summary CMS-PAS-PFT-09-001, 2009.
- [25] CMS Collaboration, "Commissioning of the Particle-flow Event Reconstruction with the first LHC collisions recorded in the CMS detector", CMS Physics Analysis Summary CMS-PAS-PFT-10-001, 2010.
- [26] CMS Collaboration, "Commissioning of the Particle-Flow reconstruction in Minimum-Bias and Jet Events from pp Collisions at 7 TeV", CMS Physics Analysis Summary CMS-PAS-PFT-10-002, 2010.
- [27] CMS Collaboration, "Particle-flow commissioning with muons and electrons from J/Psi and W events at 7 TeV", CMS Physics Analysis Summary CMS-PAS-PFT-10-003, 2010.
- [28] CMS Collaboration, "Reconstruction and identification of lepton decays to hadrons and at CMS", *JINST* **11** (2016), no. 01, P01019, doi:10.1088/1748-0221/11/01/P01019, arXiv:1510.07488.
- [29] CMS Collaboration, "Performance of reconstruction and identification of tau leptons in their decays to hadrons and tau neutrino in LHC Run-2",
- [30] CMS Collaboration, "Performance of CMS muon reconstruction in pp collision events at $\sqrt{s} = 7$ TeV", *JINST* **7** (2012) P10002, doi:10.1088/1748-0221/7/10/P10002, arXiv:1206.4071.
- [31] CMS Collaboration, "Performance of electron reconstruction and selection with the CMS detector in proton-proton collisions at $\sqrt{s} = 8$ TeV", *JINST* **10** (2015), no. 06, P06005, doi:10.1088/1748-0221/10/06/P06005, arXiv:1502.02701.
- [32] M. Cacciari and G. P. Salam, "Pileup subtraction using jet areas", *Phys. Lett. B* **659** (2008) 119, doi:10.1016/j.physletb.2007.09.077, arXiv:0707.1378.

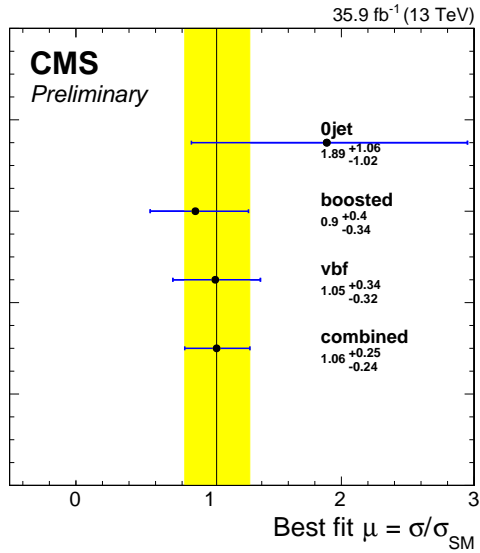


Figure 80: Observed μ -values, per channel and combined.

- [33] M. Cacciari, G. P. Salam, and G. Soyez, "The anti- k_t jet clustering algorithm", *JHEP* **04** (2008) 063, doi:10.1088/1126-6708/2008/04/063, arXiv:0802.1189.
- [34] CMS Collaboration. https://twiki.cern.ch/twiki/bin/view/CMS/JetID#Recommendations_for_13_TeV_data.
- [35] CMS Collaboration, "MSSM Higgs to tau tau search at 13 TeV using the 2015 data sample".
- [36] D. Jang, "Search for MSSM Higgs decaying to tau pairs in $p\bar{p}$ collision at $\sqrt{s} = 1.96$ TeV at CDF". PhD thesis, Rutgers University, 2006. FERMILAB-THESIS-2006-11.
- [37] ATLAS and CMS Collaborations, LHC Higgs Combination Group, "Procedure for the LHC Higgs boson search combination in Summer 2011", Technical Report ATL-PHYS-PUB 2011-11, CMS NOTE 2011/005, CERN, 2011.
- [38] CMS Collaboration, "Combined results of searches for the standard model Higgs boson in pp collisions at $\sqrt{s} = 7$ TeV", *Phys. Lett. B* **710** (2012) 26, doi:10.1016/j.physletb.2012.02.064, arXiv:1202.1488.
- [39] T. Junk, "Confidence level computation for combining searches with small statistics", *Nucl. Instrum. Meth. A* **434** (1999) 435, doi:10.1016/S0168-9002(99)00498-2, arXiv:hep-ex/9902006.
- [40] A. L. Read, "Presentation of search results: the CL_s technique", *J. Phys. G* **28** (2002) 2693, doi:10.1088/0954-3899/28/10/313.